

Development and Applications
of Synchrotron Radiation
Microtomography

Dissertation

der Fakultät für Physik der
Ludwigs-Maximilians-Universität München

vorgelegt von

WOLFGANG LUDWIG

Januar 2001

DEVELOPMENT AND APPLICATIONS
OF SYNCHROTRON RADIATION
MICROTOMOGRAPHY

DISSERTATION

der Fakultät für Physik der
Ludwigs-Maximilians-Universität München

vorgelegt von Wolfgang Ludwig
aus Ingolstadt

München, den 23.01.2001

1. Gutachter: Prof. Dr. J. Peisl
2. Gutachter: Prof. Dr. K. Karrai
Tag der mündlichen Prüfung: 16. Mai 2001

*"The problems worthy of attack
Prove their worth by hitting back"
Piet Hein*

Meinem kleinen Ferdinand und seiner Mutter

Zusammenfassung

Mit der Entwicklung von Synchrotron-Strahlungsquellen der dritten Generation wurde der zerstörungsfreien Röntgendiagnostik eine Reihe von neuen Anwendungsgebieten in der Materialforschung erschlossen. Die räumliche Kohärenz der Synchrotron-Strahlung ermöglicht eine einfache Variante der Phasenkontrast-Bildgebung (*in-line* oder *Gabor-Holographie*), mit deren Hilfe Variationen im Brechungsindex der durchstrahlten Proben nachgewiesen werden können. Mit Hilfe numerischer Algorithmen kann man aus einer Serie solcher Hologramme, die in verschiedenen Entfernungen von der Probe aufgenommen werden, den Phasenschub der transmittierten Strahlung bestimmen. Die tomographische Rekonstruktion einer Vielzahl solcher Phasenbilder liefert die dreidimensionale Verteilung des Brechungsindex in der Probe und erlaubt den Nachweis von geringen Dichteunterschieden, welche im konventionellen Absorptionsbild verborgen bleiben.

Unter bestimmten Bedingungen läßt sich das tomographische Prinzip auch auf die Analyse von Defektstrukturen in nahezu perfekten Einkristallen anwenden. In diesem Fall nutzt man eine spezielle Art von Beugungskontrast (Röntgen-Topographie, 'direktes Bild'), welcher Gitterverzerrungen in der Nähe von Kristallbaufehlern sichtbar macht. Mit dieser Kombination aus Topographie und Tomographie gelang es, die Anordnung von Versetzungen in einem synthetischen Diamantkristall dreidimensional darzustellen.

Fortschritte in der Instrumentierung (Detektorsystem, Monochromator, mechanischer Aufbau, ...) erlauben darüber hinaus die Anwendung der Mikroradiographie auf materialwissenschaftliche Fragestellungen, welche bisher aufgrund mangelnden räumlichen oder zeitlichen Auflösungsvermögens nicht oder nur schlecht untersucht werden konnten.

So liefern *in-situ* Beobachtungen der Korngrenzenbenetzung im System Aluminium / Gallium den direkten Nachweis, daß - entgegen gängigen Modellen - das Eindringen des flüssigen Metallfilms mit einer Bewegung der angrenzenden Aluminium Körner verbunden ist. Auch die Beobachtung einer diskontinuierlichen Ausbreitung des flüssigen Films entlang der Korngrenze ist nicht im Einklang mit existierenden Modellen der Korngrenzenbenetzung, welche einen diffusiven Materialtransport (Abtransport von Aluminium entlang der Korngrenze) als prinzipiellen Mechanismus vorsehen. Die Diskontinuitäten lassen sich im Rahmen eines Modelles erklären, welches das schnelle Eindringen von Gallium auf die Fortpflanzung eines Sprödbruchs entlang der Korngrenze zurückführt.

Aufgrund der nahezu vollständigen Benetzung von Aluminium Korngrenzen kann Gallium dazu verwendet werden, die Korngrenzenstruktur in Aluminium Vielkristallen dreidimensional darzustellen. Flüssiges Gallium dient in diesem Fall als Kontrastmittel. Mit Hilfe dieser Technik ist es möglich die Ausbreitung von Ermüdungsrissen und ihre Wechselwirkung mit der Kornstruktur detailliert zu analysieren.

Abstract

The advent of third generation synchrotron sources has entailed considerable progress in the field of X-ray imaging. The coherence properties of modern synchrotron beams opened the way for an experimentally simple variant of hard X-ray phase contrast imaging, based on Fresnel diffraction. Combining the information contained in a series of such diffraction patterns recorded at different distances from the object, it is possible to determine the phase shift of the X-ray wavefield. Together with tomographic image acquisition this gives rise to a new quantitative imaging technique (holotomography) which allows to determine the three-dimensional distribution of the refractive index decrement within the object. Moreover, the optimization of critical components of the imaging set-up like the monochromator and the high resolution detector system have considerably enhanced the temporal and spatial resolution of X-ray micro-imaging. High bandwidth, synthetical multilayer monochromators deliver two orders of magnitude higher photon flux compared to conventional Si monochromators and optimized X-ray to visible light converter screens based on transparent LAG crystals provide one micrometer spatial resolution.

In addition to absorption and phase contrast, which are used to characterize sample inhomogeneities at the micrometer level one may also use diffraction contrast (X-ray topography) in order to reveal atomic scale deviations from the lattice periodicity in crystalline materials. Provided the 'direct image' is the prevalent contrast mechanism, one may combine X-ray topography and tomography to a three-dimensional imaging technique (topo-tomography). Using this technique it is possible to analyze the three-dimensional arrangement of crystalline defects like individual dislocations in rather perfect single crystals.

The combination of high temporal and spatial resolution makes X-ray imaging the ideal tool for the study of dynamic processes in the bulk of opaque materials. Our observations of grain boundary wetting in the room temperature system Al/Ga take advantage of these *in-situ* imaging capabilities of X-ray micro-radiography and give strong evidence that the rapid penetration of microscopic liquid Ga films along the grain boundaries of Al differs principally from the wetting behaviour in high temperature systems. The systematic observation of grain displacement during the wetting process and the discontinuous character of the thickening and propagation process give strong evidence for a mechanism which involves the propagation of a brittle crack along the grain boundary. The absence of microscopic wetting layers in small grained polycrystals reveals further the importance of geometrical and mechanical constraints for the wetting process.

Liquid Ga can be used as a contrast agent to reveal the three-dimensional grain boundary structure in Al polycrystals by tomographic imaging in absorption mode (grain boundary imaging). The interest of this technique is demonstrated for the post-mortem characterization of fatigue cracks in cast Al alloy. The three-dimensional analysis reveals clear evidence for the interaction of short fatigue cracks with the grain structure in the bulk of the polycrystalline material.

Acknowledgements

This thesis has been prepared in the Topography group at the European Synchrotron Radiation Facility. I am much indebted to Dr. José Baruchel, director of the Topography group, who accepted me in his group and who supported me and my work in his effective and uncomplicated way.

Meinem Doktorvater Prof. Johann Peisl danke ich für sein Vertrauen und seine Bereitschaft, mir diese Arbeit fernab vom heimatlichen Institut zu ermöglichen.

Je remercie tout particulièrement Peter Cloetens, qui m'a accompagné comme ami et mentor pendant ce travail. Inutile de mentionner ses capacités nombreuses et toutes azimuts (à part peut-être, une légère faiblesse quant à la pratique du ski dans la neige de printemps...).

Un très grand merci également à Daniel Bellet et Yves Bréchet, jeunes professeurs à l'INPG de Grenoble, qui ont attiré mon attention au problème du mouillage de joints de grains. Grâce à leur soutien et intérêt pour le sujet nous avons pu, à la fin, décélérer certains secrets de ce phénomène bien miraculeux.

I would like to thank Profs. E. Glickman, E. Rabkin, M. Biscondi, K. Wolski, D. Chatain, W. Gust, C. Herzig, F. Barbier and N. Eustathopoulos for helpful discussions concerning the problem of grain boundary wetting.

Ce fut un grand plaisir de collaborer avec l'équipe 'destructive' de Lyon: P.H. Jouneau, N. Godin, E. Maire, S. Savelli, G. Peix et tout particulièrement Jean-Yves Buffière. Bien que leur intérêt principal était de maltraiter leurs pauvres éprouvettes d'aluminium, ils ont toujours su réjouir leurs 'local contacts' avec un tas de friandises et leur humour. Merci aussi à M. Veron et P. Prosenko, LTPCM Grenoble, pour leur aide à la préparation des échantillons et à Jérémie Teyssier pour le dépouillement d'une partie des données sur le mouillage.

It was a great pleasure to work with S.F. Nielsen and H.F. Poulsen from the Risø National Laboratory, Denmark. Their competence and their willingness to explore new fields of applications for the 3D X-ray microscope at ID11 gave rise to a fruitful and ongoing collaboration.

C'est grâce à Sébastien Bouchet, que la segmentation tri-dimensionnelle des données tomographiques a vu le jour à l'ESRF. Son travail d'implémentation d'algorithmes morphologiques nous a permis de procéder à l'autopsie virtuelle des polycristaux.

This work could not have been accomplished without the help of numerous colleagues from the ESRF and its support groups: I. Snigireva (micro-manipulation), J.C. Labiche and co-workers (Frelon camera), H. Müller (chemistry), D. Fernandez (SPEC), P. Bernard (design) and A. Hammersley (computing). It is mainly the merit of A. Koch (detectors) and his work on transparent scintillators crystals, that imaging with micrometer and sub-micrometer spatial resolution became possible. We could not have benefitted of this resolution without the use of multilayer monochromators, which have been prepared by C. Morawe (optics group).

Thanks also to G. Förstner, D. Use and R. Dimper who managed to rescue part of our data from transience in the clusters of NICE and who did not go mad about the fact, that we permanently filled their disks and produced more than 1 Terabyte of tomographic data during this work.

Incontournable également la mention des membres actuelles et anciens du groupe *Topographie*, au sein duquel ce travail a été effectué. Commençons par Elodie, jeune ingénieur, qui s'est mise à ramasser de l'argent industriel pour financer la recherche de ses pauvres collègues: merci pour ton aide pendant de nombreuses manips ! Merci également aux membres de l'entité 'osseuse': Stefania, Estella, Abdelmajid et Françoise. C'est Jürgen Härtwig, maître de la théorie dynamique, qui m'a appris les bases de la topographie au départ de mon séjour à l'ESRF (vive le mono courbable!). Je remercie Jean-Pierre Guigay et Michel Schlenker, pour leur disponibilité concernant toutes questions sur l'imagerie. Un grand merci également à Dominique Rohlion, François Thurel et René Chagnon pour leur aide concernant tous aspects techniques et mécaniques de mon travail. On n'a jamais pu conclure, pourquoi les nuages ne tombent pas du ciel, mais ce fut plaisir d'en discuter avec Holger Klein. Finalement, il y avait aussi une vie en dehors de l'ESRF (bien qu'à la fin un certain déséquilibre était à constater): les sorties en montagne avec Frank Heyroth, Stefan Köhler, Michael Ohler, Silvano Agliozzo, Olivier Mathon (vive l'escalade) et Lukas Helfen (VTT...), ainsi que les barbecues chez Etienne et Petra Pernot ont beaucoup aidé pour remonter le moral après des semaines dures au synchrotron.

Meinen Eltern, die mir diese Arbeit ermöglicht haben, sowie meinen Geschwistern und allen Freunden sei Dank für Ihre Unterstützung in den letzten Jahren.

Contents

Introduction	1
I Methods and Instrumentation	5
1 Imaging with hard X-rays	7
1.1 Introduction	7
1.2 The transmission function	8
1.3 Absorption imaging	9
1.4 Phase contrast	10
1.4.1 Partial Coherence	11
1.4.2 Edge enhancement	13
1.4.3 Quantitative phase reconstruction	14
1.5 Tomography	15
1.5.1 Determination of projections	17
1.5.2 Tomographic reconstruction	17
2 Instrumentation	21
2.1 Source characteristics	22
2.1.1 The source size	23
2.2 Choice of the monochromator	24
2.2.1 Silicon monochromators	24
2.2.2 Multilayer monochromators	25
2.2.3 Preservation of coherence	27
2.3 The high-resolution detector system	30
2.3.1 X-ray imaging with thin film scintillators	30
2.3.2 Optimization of the converter screens	33
2.3.3 Fast-readout, low-noise CCD camera (FRELON camera)	35
2.3.4 Detective Quantum Efficiency	37
2.3.5 Determination of the transfer function	38
2.4 The mechanical setup	40

3	Methods	43
3.1	Holotomography	43
3.1.1	Case of 'weak' phase objects	43
3.1.2	Approximate solution for the case of an absorbing object	45
3.1.3	Experimental results	47
3.1.4	Conclusion	52
3.2	Topo-Tomography	53
3.2.1	Motivation	53
3.2.2	The principle	53
3.2.3	The experimental set-up	55
3.2.4	Results	56
3.2.5	Discussion	58
3.2.6	A possible variant for polycrystalline material	60
3.2.7	Conclusion	60
II	Applications	63
4	Grain boundary wetting	65
4.1	Introduction	65
4.2	General background about GBW	66
4.3	Peculiarities of GBW in the Al/Ga system	69
4.3.1	Material properties	69
4.3.2	GBW and LME in the Al/Ga system	69
4.4	Sample preparation	71
4.4.1	Initial wetting contact	72
4.5	2D characterization of GBW	73
4.5.1	In-situ radiography	73
4.5.2	Observations with Al bicrystals	78
4.6	3D characterization of GBW in polycrystals	81
4.6.1	Microtomographic characterization of Al polycrystals	82
4.6.2	Characterization by X-ray tracking	84
4.6.3	Tomographic observations with industrial Al alloy	87
4.7	Discussion	92
4.7.1	Possibilities and limitations of X-ray micro-imaging	92
4.7.2	Interpretation of the experimental results	94
4.7.3	A possible mechanism	96
4.8	Conclusions	98

5 Grain boundary imaging	101
5.1 Motivation	101
5.2 Fatigue properties of Al/Si cast alloy	103
5.3 Experimental Results	104
5.3.1 Observations on the sample surface	104
5.3.2 3D analysis of the crack morphology	105
5.3.3 Determination of the 3D grain structure	106
5.4 Discussion	108
5.5 Conclusion	113
Conclusion	115
Bibliography	i
A The new tomograph	ix
B Approximation for an absorbing object	xiii
C Basic concepts of GBW models	xv
C.1 The role of coherency strain	xv
C.2 The dissolution models	xvi
C.2.1 The model of Fradkov	xvi
C.2.2 The model of Bokstein	xvii
C.3 A thermodynamic approach	xvii
C.4 The SIIS model	xvii
Curriculum Vitae	xxi

Introduction

Among the variety of characterization methods used in materials science, imaging plays undoubtedly a predominant role. This is well reflected in the wide spectrum of established imaging techniques which employ such different probes like ultrasound, electro-magnetic radiation, electrons and neutrons. One uses the interaction of these probes with matter in order to reveal local variations of material properties like the attenuation, electron density, polarization,

The interest of hard X-ray imaging (>10 keV), compared to electron microscopy (EM), which may be considered as the standard imaging tool in materials science, arises from the fact that X-rays have a higher penetration depth and do usually not require special sample preparation. Moreover, the high penetration and depth of field allow the introduction of special sample environments such as cryostats, furnaces or tension rigs. Finally, X-ray radiography can be easily extended to computed tomography (CT), its three-dimensional counterpart, which has revolutionized medical imaging [Hou72] in the last thirty years.

Despite its great success in medical imaging and in non-destructive testing, X-ray CT has still found only few applications in materials science, mainly due to the fact that the spatial resolution achievable with conventional X-ray scanners ($\cong 10 \mu\text{m}$ [SD98]) is too restrictive.

Due to ongoing progress in hard X-ray Synchrotron Radiation (SR) micro-imaging, this situation is about to change. The optimization and development of new X-ray optical elements (e.g. multilayers, compound refractive lenses [LSR⁺99], Fresnel zone plates [DiF99]) together with the optimization of high-resolution X-ray imaging detectors have extended the spatial resolution of SR X-ray imaging to the micrometer and submicrometer range [KPH⁺99, LST⁺99].

In addition to the enhanced resolution, a simple variant of phase-contrast imaging has become available. The coherence properties of third generation synchrotron beams give rise to interference effects which build up after free-space propagation of the diffracted wavefields behind the sample (Fresnel diffraction). To a first approximation the contrast in such diffraction patterns (in-line holograms, [SSK⁺95, CBB⁺96]) is proportional to the Laplacian of the refractive index, projected along the beam direction. It depends therefore in a highly nonlinear way on the object properties and is best described as *edge enhancement*.

A more sophisticated approach to X-ray phase imaging consists in the quantitative reconstruction of the phase shift, the X-ray beam experienced by traversing the sample. The implementation of such a phase retrieval algorithm, based on the numerical processing of a series of images, taken at different sample to detector distances (similar to the defocussing technique in high-resolution electron microscopy, [CJBD92, BDC96]) has been recently carried out by P. Cloetens [Clo99]. The extension of the two-dimensional phase retrieval method to a three-dimensional imaging technique is straightforward: the determination of the phase shift (2D) for a large number of orientations allows to reconstruct the spatial (3D) distribution of the refractive index decrement by use of standard tomographic reconstruction algorithms. This technique, 'holotomography' [CLB⁺99], was demonstrated recently for the case of a pure phase object. We will

discuss the extension of holotomography to the case of absorbing objects and present a practical application in metallurgy.

In absorption and phase-contrast imaging one usually neglects small deviations from the transmission behaviour due to Bragg diffraction in crystalline parts of the sample, which consists usually of polycrystalline or amorphous materials. Is it possible to use X-ray diffraction as contrast mechanism for tomographic imaging and to extend tomography to the case of single-crystalline materials? We will show that the combination of X-ray diffraction imaging (topography) and tomography is indeed possible for rather perfect single crystals, giving rise to a new 3D imaging technique ('topo-tomography').

In the view of the mentioned progress and enhancement of X-ray imaging, we are now in the position to address new, challenging problems in various fields of life and materials science. With a spatial resolution of $1\ \mu\text{m}$ we dispose of a resolution comparable to light microscopy and we can consequently contribute to a whole class of problems, where this lengthscale is of particular interest.

X-ray micro-imaging is further of invaluable interest for problems, where high spatial *and* temporal resolution are required for the study of *dynamic* processes in the bulk of opaque samples. An ideal example of this type is the wetting of metal grain boundaries by a liquid metal. In a large number of systems (e.g. Cu/In, Al/Ga, Fe/Zn, Cu/Bi, ...) one observes the rapid penetration of microscopic ($0.1 - 10\ \mu\text{m}$) liquid films along the grain boundaries of the host metal. This process may give rise to catastrophic failure, if the solid metal is subject to external or internal stresses. This failure mechanism, known as liquid metal embrittlement (LME) [NO79, FJ97] is of relevance when structural metals are exposed to liquid metal environments. The subject has gained renewed interest in recent years due to the active international efforts to develop 'safe' (undercritical), accelerator driven nuclear reactors where liquid metals serve as targets and cooling fluids. Among the different systems displaying such wetting transitions, the room temperature system Al/Ga ($T_{m,\text{Ga}} = 29^\circ\text{C}$) shows a quite peculiar behaviour: the spreading of the liquid gallium occurs at rates which are two or three orders of magnitude higher compared to other 'classical' couples. Despite numerous efforts, no generally accepted model has emerged so far, which could account for this rapid penetration. Our attempts, to characterise this process by applying state-of-the-art X-ray imaging techniques revealed interesting new aspects of this intriguing phenomenon.

The current work has been divided into two parts: *I. Methods and Instrumentation* and *II. Applications*.

The first part includes an introduction to the basic concepts of two-dimensional and three-dimensional X-ray imaging under coherent illumination (chapter 1). In chapter 2 we discuss relevant characteristics of the X-ray source and present our contribution to the development and optimization of the different components of the experimental set-up. The demonstration of new variants of X-ray imaging (holotomography and topo-tomography) will be the subject of chapter 3.

In the second part we applied X-ray micro-imaging to the study of two particular problems in materials science: (i) the wetting of aluminium grain boundaries by liquid gallium (chapter 4) and (ii) the propagation and interaction of short fatigue cracks with respect to the microstructure in polycrystalline materials (chapter 5).

In chapter 4 we will give an introduction to the current understanding and to the open questions in the field of grain boundary wetting. We will then demonstrate in how far different X-ray micro-imaging techniques may help to elucidate different aspects of this bulk phenomenon.

The *in-situ* observation of grain boundary wetting in the Al/Ga system pushes X-ray imaging to its limits: ultimate sensitivity and the combination of high spatial *and* temporal resolution are required to characterize the penetration of sub-micrometric liquid Ga films along the grain boundaries.

The characterization of fatigue cracks (chapter 5) benefited a lot from an interesting finding, realized during our studies of the wetting process in Al alloys: liquid Ga can be used as a *contrast agent* to visualize the three-dimensional grain structure in Al polycrystals by absorption tomography. Collaborating with a materials science laboratory, specialized on damage mechanisms in compound materials (GEMPPM, INSA Lyon) we applied this new technique ('grain boundary imaging') to the case of a (fatigued) Al alloy, containing short cracks. The three-dimensional analysis of the crack structure in the bulk of the sample provides interesting aspects about the propagation mechanism of such short cracks.

Part I

Methods and Instrumentation

Chapter 1

Imaging with hard X-rays

1.1 Introduction

The interaction of X-rays with matter can be used in quite different ways to obtain images revealing qualitative or quantitative information about the internal structure of the specimen. X-ray absorption radiography, pioneered by Röntgen as early as 1896, is due to its simplicity and versatility still by far the most employed X-ray imaging technique with countless applications in medical and industrial imaging. The attenuation of X-rays in matter is based on different interaction processes of the photons with the electrons in the material. In the energy range between 1 and 100 keV the main contributions to the total interaction cross-section are

Photoabsorption σ_{pe} : The energy of the incoming photon is transferred to a bound electron which is expelled from the atom. The photo-electric cross-section depends strongly on photon energy and atomic number ($\sigma_{pe} \sim Z^4 E^{-3}$) and displays strong discontinuities at energies close to bound electron energy levels.

Coherent (Rayleigh) scattering σ_r : The incoming photon is scattered *elastically*, i.e. it changes only direction, but not its energy. The scattering cross-section σ_r is proportional to Z and closely related to the macroscopic refractive index of the material.

Incoherent (Compton) scattering σ_c : In this case the photon is scattered *inelastically*, i.e. part of its energy is transferred to the electron.

In the considered energy range the total cross-section $\sigma_{tot} = \sigma_{pe} + \sigma_r + \sigma_c$ is governed by photoelectric absorption. However, particularly for light elements and high energies, the scattering gives rise to a background signal and contrast deterioration when the detector is positioned close to the sample. Figure 1.1a shows the variation of the individual cross-sections as a function of photon energy for the element Ga.

We will adopt the usual description of the interaction of X-rays with matter by writing the complex refractive index in the form

$$n = 1 - \delta + i\beta \quad (1.1)$$

The refractive index decrement δ for hard X-rays is a small, positive number in the order of $\delta \approx 10^{-5} \dots 10^{-6}$ and can be expressed as

$$\delta = \frac{r_c \lambda^2}{2\pi V} \sum_j N_j \text{Re}(f_j) \quad \text{with} \quad f = f^0 + f' + if'' \quad (1.2)$$

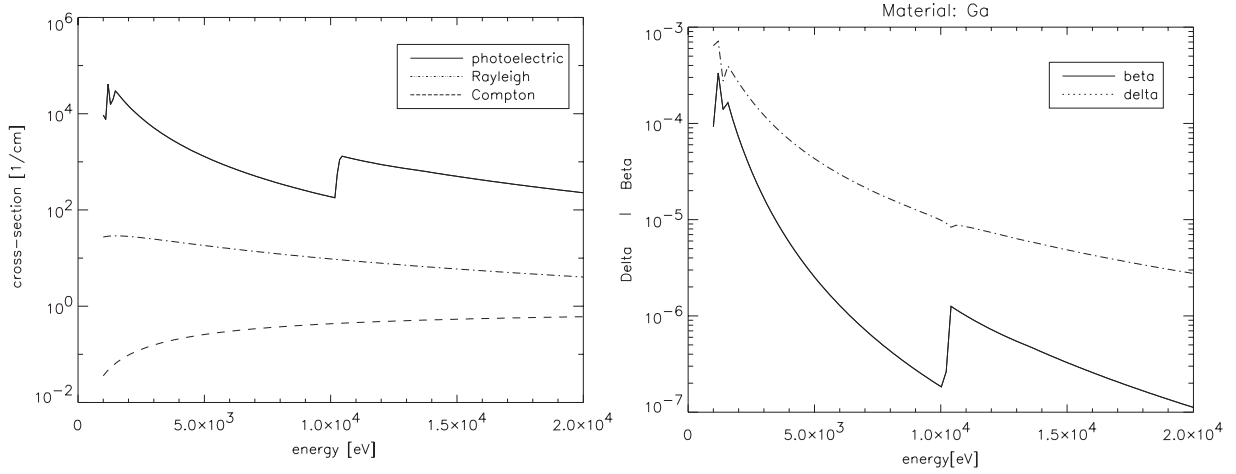


Figure 1.1: a) Photoelectric σ_{pe} (—), Rayleigh σ_{r} (- · - ·) and Compton σ_{c} (---) cross-section of Ga as a function of energy. Discontinuities in the photoelectric absorption cross-section like the one at the K-edge of Ga (10.4 keV) can be used to perform element sensitive K-edge subtraction imaging b) Relative magnitudes of the real (δ) and imaginary parts (β) of the refractive index of Ga.

where f is the atomic scattering factor for forward diffraction ($f^0 \equiv Z$), $r_c = e^2/mc^2 = 2.82$ fm is the Thomson scattering length (or classical electron radius) and N_j is the number of atoms of type j in the representative volume V . The wavelength dependent dispersion corrections f' and f'' show resonance effects in the vicinity of X-ray absorption edges where strong changes in the phase and the amplitude of the scattered wave occur. The imaginary part of the atomic scattering factor f'' is related to the photoelectric absorption coefficient σ_{pe} via

$$f''(\omega) = \frac{\omega}{4\pi r_e c} \sigma_{\text{pe}}(\omega) \quad (1.3)$$

and f' is connected to f'' by the Kramers-Kronig relation

$$f'(\omega) = \frac{2}{\pi} P \int_0^\infty \frac{\omega' f''(\omega', 0)}{\omega^2 - \omega'^2} d\omega' \quad (1.4)$$

where P denotes the Cauchy principle value of the integral.

1.2 The transmission function

Formally, the propagation of X-rays through an object may be described by means of the transmission function $T(x, y)$ which is determined by projections of the real and imaginary part of the refractive index distribution along the beam direction. The interaction of a plane, monochromatic wave u_0 with the sample may then be described by a simple multiplication in real space

$$u_{\text{obj}} = u_0 \cdot T(x, y) \quad \text{with} \quad T(x, y) = A(x, y) \exp \{i\varphi(x, y)\} \quad (1.5)$$

where

$$A(x, y) = e^{-B(x, y)} \quad (1.6)$$

$$B(x, y) = \frac{2\pi}{\lambda} \int \beta(x, y, z) dz \quad (1.7)$$

$$\varphi(x, y) = \frac{2\pi}{\lambda} \int 1 - \delta(x, y, z) dz = \varphi_0 - \frac{2\pi}{\lambda} \int \delta(x, y, z) dz. \quad (1.8)$$

In the following we will neglect the constant phase term φ_0 which has no influence on the recorded intensities and may be regarded as the phase of the reference wave in vacuum. The following inequalities hold for the case of hard X-rays

$$B(x, y) \geq 0 \quad (\text{no X-ray sources in the sample}) \quad (1.9)$$

$$\varphi(x, y) - \varphi_0 \leq 0 \quad (\text{Thomson scattering}) \quad (1.10)$$

The above approach is justified as long as the propagation inside the sample can be considered to occur along straight lines. Therefore, angular deviations due to refraction ($\alpha \sim \nabla\varphi$) and/or total reflection ($\alpha_c = \sqrt{2\delta}$) must be small compared to the spatial resolution $r_d \cong 1 \mu\text{m}$ of the detector. This yields a limit of 1 mm for the sample thickness, if the extreme case of total reflection at sample interfaces ($\alpha_c = \sqrt{2\delta} \sim 10^{-3}$) is considered. In the absence of strong refraction effects, Fresnel diffraction *inside* the sample (thickness t_s) will still be a limiting factor for the sample thickness: a point at the exit plane of the object mainly contains information from a region corresponding to the the first Fresnel zone ($\sqrt{\lambda t_s}$). The condition

$$r_d \geq \sqrt{\lambda t_s}$$

yields a maximum thickness t_{max} in the order of 10 mm for a wavelength of 1 Å and a spatial resolution r_d of 1 μm .

In the following sections we will describe the different variants of X-ray imaging with the help of the concept of the complex transmission function. We will only consider the case of projection imaging, i.e. X-ray imaging without the use of refractive (e.g. compound refractive lenses, [LSR⁺99]) or diffractive (e.g. Fresnel zone plates, [DiF99]) lenses.

1.3 Absorption imaging

Absorption imaging is still by far the most used X-ray imaging technique, mainly because of its experimental ease and versatility. It does not require coherent illumination and can be performed with conventional X-ray sources. The interest of synchrotron radiation for this technique is mainly due to the tremendous gain in flux and the possibility to select the energy according to the requirements imposed by the size and the composition of the sample.

For quantitative absorption measurements it is necessary to determine the intensity with and without the object. As, in a real experiment, the profile of the incoming beam is not perfectly uniform (neither in the direction perpendicular nor in the one parallel to the beam) and as it varies slowly with time, it is important to take both images within a few minutes and without moving the detector (i.e the incoming intensity is determined by moving the object out of the beam path)

$$I_{\text{obj}}(x, y) = A^2(x, y)I_{\text{inc}}(x, y) \quad \text{with} \quad (1.11)$$

$$A^2(x, y) = \exp \left\{ -\frac{4\pi}{\lambda} \int \beta(x, y, z) dz \right\} = \exp \left\{ -\int \mu(x, y, z) dz \right\} \quad (1.12)$$

Logarithmic subtraction yields finally two-dimensional projections of the absorption coefficient within the sample

$$-\ln \frac{I_{\text{obj}}}{I_{\text{inc}}} = \int \mu(x, y, z) dz \quad (1.13)$$

The outlined procedure neglects the effect of the finite spatial response of the two-dimensional detector: the recorded images are convolutions of the intensity distributions with the point spread function $R_p(\mathbf{r})$ of the detector system

$$I_{\text{rec}}(\mathbf{r}) = \int I(\mathbf{r} - \mathbf{r}')R_p(\mathbf{r}')d\mathbf{r}' = I(\mathbf{r}) \otimes R(\mathbf{r}) \quad (1.14)$$

or, alternatively in frequency space

$$\tilde{I}_{\text{rec}}(\mathbf{f}) = \tilde{I}(\mathbf{f})\tilde{R}_p(\mathbf{f}) \quad (1.15)$$

A more accurate approach would therefore include the deconvolution of the recorded images before logarithmic subtraction.

1.4 Phase contrast

We will now consider in more detail the case of coherent illumination with a plane monochromatic wave. Free space propagation of the wave after the sample will transform the phase modulation into intensity variations. The diffracted wavefield can be calculated using the Fresnel-Kirchhoff diffraction integral [BW99]

$$u_d(x, y) = \frac{1}{i\lambda} \iint u_{\text{obj}}(\xi, \eta) \frac{e^{ikr_{\text{od}}}}{r_{\text{od}}} \cos(\mathbf{n}, \mathbf{r}) d\xi d\eta \quad (1.16)$$

with

$$r_{\text{od}}^2 = z^2 + (x - \xi)^2 + (y - \eta)^2 \quad (1.17)$$

The Fresnel approximation to the diffraction integral corresponds to the approximation (see also Fig. 1.2

$$r_{\text{od}} = (d^2 + (x - \xi)^2 + (y - \eta)^2)^{-\frac{1}{2}} \approx d \left(1 + \frac{(x - \xi)^2}{2d^2} + \frac{(y - \eta)^2}{2d^2} \right) \quad (1.18)$$

and reads

$$u_d(x, y) = e^{ikd} \frac{1}{i\lambda} \iint u_{\text{obj}}(\xi, \eta) \exp\left(i\frac{\pi}{\lambda d}((x - \xi)^2 + (y - \eta)^2)\right) d\xi d\eta \quad (1.19)$$

In equation (1.19) the wavefields u_d and u_{obj} are related via a convolution integral in real space. For computational reasons the calculation is usually implemented in Fourier space where the convolution simplifies to a multiplication. The equivalent expression to (1.19) is obtained when the wavefield is decomposed into plane waves components $\tilde{u}(f, g)$

$$u(x, y) = \iint_{-\infty}^{\infty} \tilde{u}(f, g) e^{i2\pi(fx + gy)} df dg \quad (1.20)$$

with

$$\tilde{u}(f, g) = \iint_{-\infty}^{\infty} u(x, y) e^{-i2\pi(fx + gy)} dx dy \quad (1.21)$$

where f and g are related to the wavevector $k = \frac{2\pi}{\lambda}$ via

$$k_x = 2\pi f \quad k_y = 2\pi g \quad k_z = \sqrt{k^2 - k_x^2 - k_y^2} = \frac{2\pi}{\lambda} \sqrt{1 - (\lambda f)^2 - (\lambda g)^2} \quad (1.22)$$

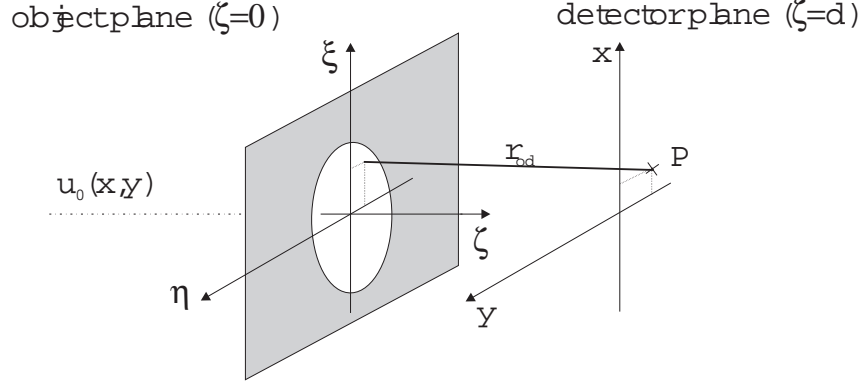


Figure 1.2: In the Fresnel approximation the object - detector distance r_{od} is approximated by $d(1 + \frac{(x-\xi)^2}{2d^2} + \frac{(y-\eta)^2}{2d^2})$.

Propagation of the wavefield to $z = d$ corresponds to a multiplication of the plane wave components with a phase term $\exp(ik_z d)$

$$\tilde{u}_d(f, g) = \tilde{u}_{obj}(f, g) \cdot \exp\left(i\frac{2\pi}{\lambda}\sqrt{1 - (\lambda f)^2 - (\lambda g)^2}d\right) \quad (1.23)$$

and a similar development of the square root like in (1.18) yields

$$\tilde{u}_d(f, g) = \tilde{u}_{obj}(f, g) \cdot \tilde{P}_d(f, g) \quad (1.24)$$

with

$$\tilde{P}_d(f, g) = \exp\left[-i\pi\lambda d(f^2 + g^2)\right] \quad (1.25)$$

where we neglected an overall phase term. The intensity spectrum $\tilde{I}_d(f, g)$ is obtained via autocorrelation of the wavefunction in reciprocal space $\tilde{u}_d(f, g)$

$$\tilde{I}_d(f, g) = \int \tilde{u}_d(p, q) \tilde{u}_d^*(p - f, q - g) dp dq \quad (1.26)$$

Alternatively it is possible to express the intensity spectrum by one of the following 2D integrals in real space [Gui77]

$$\tilde{I}_d(\mathbf{f}) = \int e^{-i2\pi\boldsymbol{\eta}\mathbf{f}} u_0\left(\boldsymbol{\eta} - \frac{\lambda d\mathbf{f}}{2}\right) u_0^*\left(\boldsymbol{\eta} + \frac{\lambda d\mathbf{f}}{2}\right) d\boldsymbol{\eta} \quad (1.27)$$

$$\tilde{I}_d(\mathbf{f}) = e^{-i2\pi\lambda d\mathbf{f}^2} \int e^{-i2\pi\boldsymbol{\eta}\mathbf{f}} u_0(\boldsymbol{\eta}) u_0^*(\boldsymbol{\eta} + \lambda d\mathbf{f}) d\boldsymbol{\eta} \quad (1.28)$$

So far we have restricted our discussion to the ideal case of a plane monochromatic incident wavefield $u_0(\mathbf{x})$. A simulation of the intensity distribution recorded at a given distance d has further to take into account effects like the limited spatial coherence of the incoming radiation as well as the finite response of the detector system.

1.4.1 Partial Coherence

The coherence properties of an arbitrary wavefield can be described by correlation functions depending on space and time [BW99]. In the case of quasi-monochromatic radiation a simplified

description leads to the concepts of temporal and spatial coherence. The temporal coherence $\Gamma(\tau)$ is described by the correlation of the amplitude $f(t)$ at a given point with the amplitude at the same point at time $t + \tau$

$$\Gamma(\tau) = \langle f^*(t)f(t + \tau) \rangle = \lim_{T \rightarrow \infty} \frac{1}{T} \int_{-T/2}^{T/2} f^*(t)f(t + \tau) dt \quad (1.29)$$

Its normalized version $\gamma(\tau) = \Gamma(\tau)/\Gamma(0) \leq 1$ is called the *complex degree of coherence* and it may be used to define the *longitudinal coherence length*

$$l_c = c\tau_c \quad (1.30)$$

where τ_c is the time where $|\gamma(\tau)|$ drops to $1/e$. In the case of monochromatized radiation (Si(111) double crystal monochromator, $\Delta\lambda/\lambda \approx 10^{-4}$ for $\lambda = 1\text{\AA}$) the longitudinal coherence length can be estimated to $l_c = c \cdot \tau_0 \approx c/\Delta\nu = \lambda\nu/\Delta\nu = \lambda^2/\Delta\lambda \approx 1 \mu m$. Note that the size of the sample is not limited to this length, as typical differences in the optical path length z will be in the order of $10^{-6}z$.

The correlation of the wavefield at different locations \mathbf{x}_1 and \mathbf{x}_2 and can be characterized by the mutual intensity (quasi-monochromatic case) [BW99]

$$J_z(\mathbf{x}_1, \mathbf{x}_2) = \sum u_z(\mathbf{x}_1) \cdot u_z^*(\mathbf{x}_2) \quad (1.31)$$

Again, a normalized version, called the *degree of coherence* exists, and is defined as

$$\gamma^c(\mathbf{x}_1, \mathbf{x}_2) = \frac{J(\mathbf{x}_1, \mathbf{x}_2)}{\sqrt{I(\mathbf{x}_1) \cdot I(\mathbf{x}_2)}} \quad (1.32)$$

If both points \mathbf{x}_1 and \mathbf{x}_2 coincide, the mutual intensity is equal to the usual intensity and $\gamma^c(\mathbf{x}_1, \mathbf{x}_2) = 1$. If the points are separated, $|\gamma^c|$ is a measure for the coherence of the wavefields. The *transverse coherence length* l_t may be defined as the distance $|\mathbf{x}_1 - \mathbf{x}_2| = l_t$ for which $|\gamma^c| = 1/2$.

The effect of the partial coherence is taken into account by the multiplication of the intensity spectrum (equ. 1.27) with the degree of coherence

$$\tilde{I}_d(\mathbf{f}) = |\gamma^c(\lambda d \mathbf{f})| I^{coh}(\mathbf{f}) \quad (1.33)$$

The computational ease of switching between real space and frequency space via Fast Fourier Transform (FFT) leads to the following scheme for the calculation of the intensity distribution at distance d from an object $T(\mathbf{x})$ [Clo99]

$$I_d(\mathbf{x}) = \mathcal{F}^{-1} \left\{ \tilde{R}(\mathbf{f}) |\gamma^c(\lambda d \mathbf{f})| \mathcal{F} \left\{ \left| \mathcal{F}^{-1} \left\{ \mathcal{F} \{ T(\mathbf{x}) u_{inc}(\mathbf{x}) \} \tilde{P}_d(\mathbf{f}) \right\} \right|^2 \right\} \right\} \quad (1.34)$$

This formulation accounts for non-uniform illumination (u_{inc}) of the object T . The wavefield is propagated to the distance d by multiplication with the propagator P_d in Fourier space. The intensity is calculated by multiplication with the complex conjugate in real space. Finally, the effects of partial coherence γ^c and the finite response of the detector system are taken into account by multiplication with γ^c and \tilde{R} in Fourier space.

1.4.2 Edge enhancement

We will next consider an approximation of the intensity spectrum \tilde{I}_d , valid for weak defocus conditions $\pi\lambda d\mathbf{f}^2 \ll 1$. In this case we can develop the exponential function of the propagator (equ. 1.25) and obtain

$$\tilde{u}_d(\mathbf{f}) \approx \tilde{u}_0 (1 - i\pi\lambda d\mathbf{f}^2) \quad (1.35)$$

Back-transformation into real space yields

$$u_d(\mathbf{x}) \approx u_0(\mathbf{x}) + i\frac{\lambda d}{4\pi}\nabla^2 u_0(\mathbf{x}) \quad (1.36)$$

After decomposition of u_0 into real and imaginary parts we obtain

$$I_d \approx |u_0|^2 - \frac{\lambda d}{2\pi}\text{Im}[u_0\nabla^2 u_0^*] + \text{O}(\nabla^2 u_0)^2 \quad (1.37)$$

Introducing the modulus and the phase of the object transmission function we can rewrite equ. 1.37 in the following form [CPSB⁺97] ($i_0 = |u_{\text{inc}}|^2$, intensity of the incident wavefield)

$$I_d \approx i_0 A^2 \left(1 - \frac{\lambda d}{2\pi}\nabla^2 \varphi\right) - i_0 \frac{\lambda d}{2\pi}(\nabla A^2 \nabla \varphi) \quad (1.38)$$

Under the condition, that the variations of the absorption term are small compared to the variations of the phase term we can neglect the last term in expression 1.38 and arrive at the following approximation

$$I_d(\mathbf{x}) \approx i_0 A^2(\mathbf{x}) \left(1 - \frac{\lambda d}{2\pi}\nabla^2 \varphi(\mathbf{x})\right) \quad (1.39)$$

The image at distance d is consequently the product of the absorption image $I_0 = i_0 A^2$ and a phase sensitive defocusing term.

If we dispose of two images at $d = 0$ (absorption) and $d > 0$ (phase sensitive), we can disentangle the absorption and phase contributions by rewriting equ.1.39 in the form

$$\frac{I_d(\mathbf{x})}{I_0(\mathbf{x})} - 1 \approx -\frac{\lambda d}{2\pi}\nabla^2 \varphi(\mathbf{x}) \approx -d\nabla^2 \int \delta(x, y, z) dz \quad (1.40)$$

The resulting image corresponds now to the 2D Laplacian of the projected refractive index distribution.

If we dispose only of a single image at $d > 0$ we may still transform equation 1.39 into the more convenient form [Clo99]

$$I_d \approx i_0 A^2 \exp \left\{ -\frac{\lambda d}{2\pi}\nabla^2 \varphi \right\} \quad (\text{valid for } \frac{\lambda d}{2\pi}\nabla^2 \varphi \ll 1) \quad (1.41)$$

Logarithmic subtraction of the incident and transmitted intensity yields finally

$$-\ln \frac{I_d}{i_0} \approx -\ln A^2 + \frac{\lambda d}{2\pi}\nabla^2 \varphi \approx \int \mu(x, y, z) dz - d\nabla^2 \int \delta(x, y, z) dz \quad (1.42)$$

We may interpret the resulting image as the superposition of an absorption and a phase sensitive term. The latter corresponds to the 2D Laplacian of the projection of $\delta(x, y, z)$.

Expressions 1.8 and 1.42 allow to interpret the contrast in phase sensitive images in a *qualitative* way: sample inhomogeneities like internal interfaces, pores, cracks represent singularities

in the refractive index distribution. The second derivative will generate pronounced black-white contrasts at each of these singularities.

The fact, that both expressions involve the second derivative of the projected phase shift complicates on the other hand the *quantitative* analysis of such phase sensitive images: the determination of the phase shift would require the double integration of these images and was not considered in this work.

1.4.3 Quantitative phase reconstruction

In contrast to the previous section, where we tried to calculate the intensity distribution in an arbitrary image plane from knowledge of the object transmission function we will now look for possibilities to perform the inverse task, i.e. to determine the phase modulation

$$\varphi = \frac{2\pi}{\lambda} \int \delta(x, y, z) dz$$

from knowledge of the intensity distribution behind the object. Whereas a variety of reconstruction methods are known in classical optics, so far basically only three quantitative methods have been reported in the hard X-ray regime. The basic concepts of these methods will be outlined in the next section.

Interferometric techniques determine the phase shift via analysis of the fringe patterns produced when the transmitted and the reference beam are recombined in a two-beam interferometer. Usually, a Bonse-Hart type X-ray interferometer [BH65] is used to split the incoming beam into two mutually coherent parts (see Fig. 1.3). By recording a series of interference patterns with and without sample and for different settings of the adjustable phase shifter (typically 8 images per projection), it is possible to determine the phase modulation up to an uncertainty of 2π [Mom95, BBBG97].

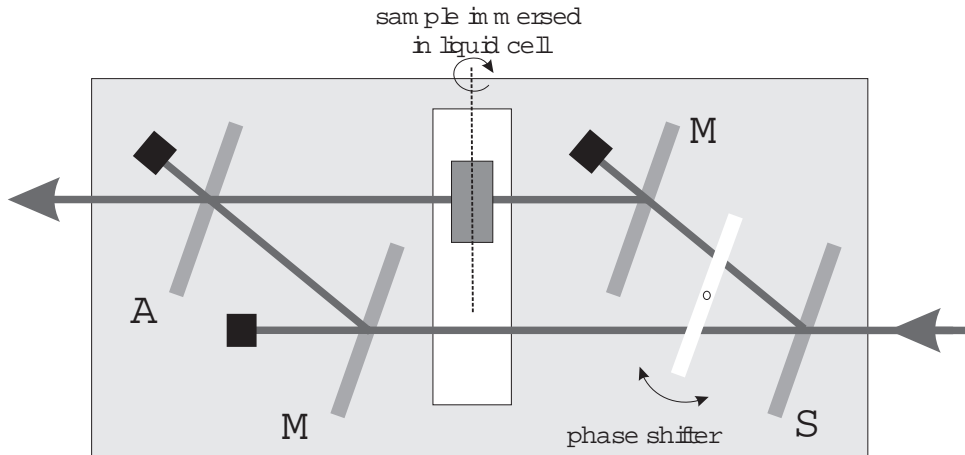


Figure 1.3: Typical design of an X-ray interferometer. The incoming beam is split by the first Laue crystal (S) and passes through the phase shifter and the liquid-filled sample cell before recombination in the analyser crystal (A). Two mirrors (M) are used in order to generate parallel trajectories in the sample cell. The phase shifter allows to vary the relative phase between object and reference beam.

The remaining 2π uncertainty in the reconstructed phase maps can be removed by numerical phase unwrapping techniques as far as the fringe spacing is large compared to the spatial resolution of the imaging detector. For this reason, the samples are usually immersed in a liquid of matched mass density in order to eliminate the phase discontinuities near the sample surface. Unlike differential phase contrast methods, the interferometric phase reconstruction is also sensitive to constant phase shifts or small gradients. The major drawback of the interferometric method is the rather poor spatial resolution in direction of the diffraction vector: due to dynamical diffraction in the analyser crystal, the resolution is limited by the width of the Borrmann fan to about $15\ \mu\text{m}$ [Bec98]. Moreover, the stringent requirements for stability (mechanical, thermal, acoustic) are experimentally demanding and impose the use of monolithic Si crystal interferometers (limited space for additional sample environment).

Schlieren imaging, known from classical optics [Hec98], is a method which is sensitive to phase gradients in the object. In the geometrical optics approximation, the local angular deviation of the beam α is proportional to the phase gradient in the object: $\alpha(x) = -2\pi/\lambda \nabla\varphi(x)$. Two different implementations are known in the X-ray regime: point by point scanning of the object by a microbeam (and analysis of the deviation of the image spot) [EMW00] and full-field analysis by means of an analyser crystal [FGZ80, BIB96]. In the latter case, quantitative image analysis has to take into account dynamical diffraction in the analyser crystal and requires *a priori* information about the object.

Propagation techniques determine the phase shift via adapted numerical processing of the intensities recorded in different image planes behind the object [Clo99, GRS⁺99]. Unlike in the previous case, these methods require spatially coherent radiation and the observed image contrast is due to interference of the locally deformed wavefronts with the unperturbed wavefield transmitted through the object (Fresnel diffraction, Gabor holography). Numerical processing of two or several such Fresnel diffraction patterns allows to determine the phase shift introduced by the object. However, due to the vanishing contrast for low spatial frequencies the determination of very weak phase gradients remains problematic with these techniques.

The approach adopted in this work is based on the latter method. Different numerical phase reconstruction algorithms, originally developed for electron microscopy [CJBD92, BDC96], were adapted to the case of X-ray imaging by P. Cloetens as part of his PhD thesis [Clo99]. Applied to the case of a pure phase object, we demonstrated recently the feasibility of quantitative X-ray phase tomography [CLB⁺99]. The extension of this method to absorbing objects will be discussed in section 3.1.

The contrast was shown to be proportional to *projections* of quantities like the linear attenuation coefficient μ (equ. 1.13) or the 2D Laplacian of projections of the refractive index decrement δ . As will be shown in the next section it is possible to extend these two-dimensional imaging techniques to three dimensions.

1.5 Tomography

So far we have limited our discussion to the case of two-dimensional X-ray imaging. In order to obtain quantitative information about the internal structure of three-dimensional objects we

have to combine X-ray imaging with computed tomography (CT), a numerical image reconstruction technique, capable to produce cross-sectional images of the object. Tomographic imaging is based on the finding, that the distribution of an unknown object function $f(\mathbf{r})$ might be calculated from the knowledge of its Radon transform (equ. 1.43), i.e. the ensemble of parallel *projections* for different orientations. In the case of X-ray imaging this unknown object function might e.g. be the spatial distribution of the attenuation coefficient $\mu(\mathbf{r})$ (absorption tomography) or the refractive index decrement $\delta(\mathbf{r})$ (quantitative phase-contrast tomography).

From a mathematical point of view, the problem of image reconstruction from projections was first addressed by Radon [Rad17] in 1917 when he studied the properties of the underlying integral transform. However, Radon's work was not known to the pioneers of computerised tomography who reported on first practical implementations in the seventies [Cor63]. The first medical scanner was build in 1972 [Hou72] and since then, computerised tomography revolutionised medical imaging. Nowadays the principle is applied to a variety of fields including electron microscopy, geophysics and materials science.

Quite generally, tomographic imaging involves two steps:

1. Determination of projections of the relevant physical object quantity (i.e. μ, δ, \dots) by adequate measurement and image processing techniques. In the case of synchrotron radiation X-ray microtomography a large number ($N \cong 1000$) of two-dimensional images are acquired while the sample is rotated stepwise [$0^\circ \dots 180^\circ$] around an axis perpendicular to the X-ray beam.
2. The 3D tomographic reconstruction of the object is performed offline in a slice by slice approach: each line in the two-dimensional projection images corresponds to the parallel projection of a given layer z of the object. The ensemble of parallel projections of a given layer for all different angular settings is called the *sinogram* or Radon transform of the layer and serves as input for the reconstruction (see Figure 1.4).

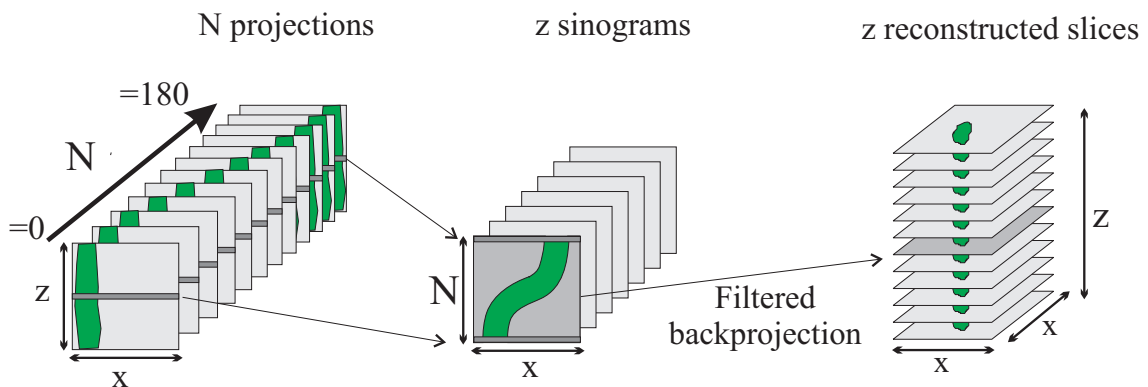


Figure 1.4: Reconstruction of a three-dimensional object in the parallel beam geometry: N two-dimensional projections are recorded while the sample is rotated stepwise over 180° . Each projection contains z lines and x columns. The projections are reorganised into z sinograms, containing N lines and x columns (Radon transform of one object layer) and the volume (z slices) is then reconstructed slice by slice.

1.5.1 Determination of projections

In our discussion of absorption contrast (§ 1.3) we already mentioned the possibility to determine projections of the attenuation coefficient μ (equ. 1.13) by two independent measurements of the incoming and the transmitted intensity: $\int \mu(x, y, z) dz = -\ln I_{\text{obj}}/I_{\text{inc}}$.

The determination of projections of the refractive index decrement $\varphi = 2\pi/\lambda \int \delta(x, y, z) dz$ turns out to be a more delicate problem which involves either the use of a Bonse-Hart type interferometer or the combination of the propagation technique with a numerical phase retrieval procedure. We will come back to the latter technique in chapter 3.1.

Moreover, in our discussion of phase sensitive imaging in the near field (weak defocus conditions) we have shown, that the Laplacian of the projection of the refractive index decrement (equ. 1.40) can be approximated by $-d\nabla^2 \int \delta(x, y, z) dz \approx I_d/I_0 - 1$. It can be shown, that tomographic reconstruction of this quantity yields the Laplacian of the refractive index decrement [Clo99, Her80].

1.5.2 Tomographic reconstruction

Tomographic reconstruction algorithms can be divided into algebraic and analytic methods. Starting from the Radon transform we will deduce the Fourier slice theorem and discuss the most popular analytic reconstruction algorithm, called *filtered backprojection*. We follow the description given in [BW99]. For a rigorous mathematical discussion the reader is referred to [Her80] or [Nat86].

Let us start by defining the two-dimensional Radon transform $F(\mathbf{n}, p)$ of an object function $f(\mathbf{x})$ which might for instance represent the spatial distribution of the absorption index within our object

$$F(\mathbf{n}, p) = \int f(\mathbf{x}) \delta(p - \mathbf{n} \cdot \mathbf{x}) d\mathbf{x} \quad (1.43)$$

The two-dimensional integral corresponds to integrations along straight lines, perpendicular to \mathbf{n} (see Fig. 1.5a). The parameter p denotes the distance from the origin.

By expressing the Dirac delta function as a Fourier integral

$$\delta(p - \mathbf{n} \cdot \mathbf{x}) = \frac{1}{2\pi} \int_{-\infty}^{\infty} e^{-iu(p - \mathbf{n} \cdot \mathbf{x})} du \quad (1.44)$$

and by inverting the order of integration in equation (1.43) we find that

$$F(\mathbf{n}, p) = \frac{1}{2\pi} \int_{-\infty}^{\infty} \tilde{f}(u\mathbf{n}) e^{-iup} du \quad (1.45)$$

where $\tilde{f}(\mathbf{k})$ is the two-dimensional Fourier transform of $f(\mathbf{x})$

$$\tilde{f}(\mathbf{k}) = \int f(\mathbf{x}) e^{i\mathbf{k} \cdot \mathbf{x}} d^2x. \quad (1.46)$$

On taking the one-dimensional Fourier transform of (1.45) we obtain

$$\tilde{f}(u\mathbf{n}) = \int_{-\infty}^{\infty} F(\mathbf{n}, p) e^{iup} dp. \quad (1.47)$$

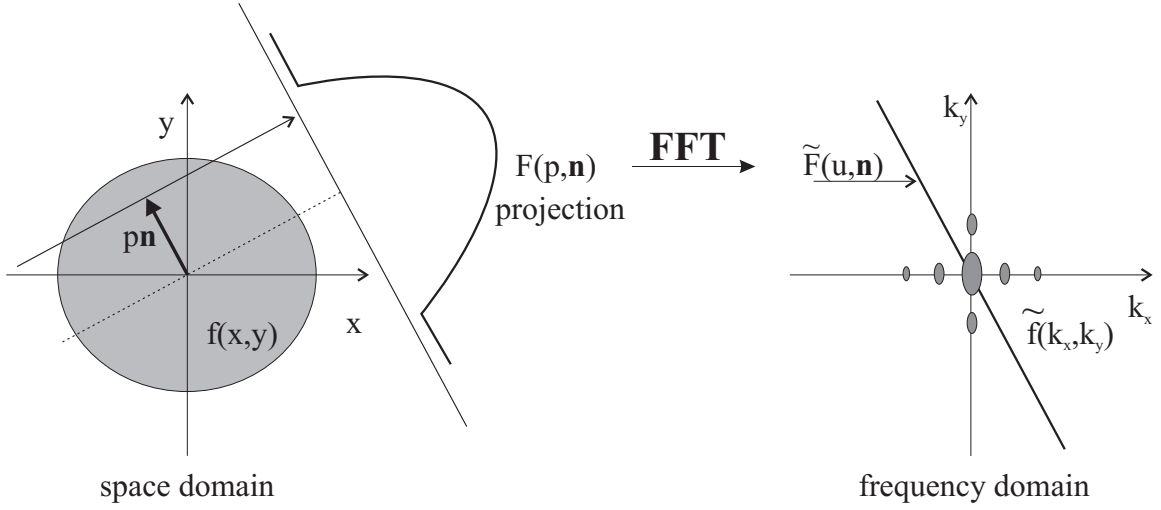


Figure 1.5: The Fourier slice theorem relates the projections $F(\mathbf{n}, p)$ with the Fourier transform $\tilde{f}(u\mathbf{n})$ of the object: a) the projections are characterized by the direction \mathbf{n} and distance p . b) the 1-dim Fourier transform of $F(\mathbf{n}, p)$ corresponds to the 2-dim Fourier transform of $f(x, y)$ along the direction \mathbf{n} : $\tilde{F}(\mathbf{n}, u) \equiv \tilde{f}(u\mathbf{n})$

Equation 1.47, rewritten in the more compact form

$$\tilde{f}(u\mathbf{n}) = \tilde{F}(\mathbf{n}, u) \quad (1.48)$$

is usually referred to as the *projection slice theorem*. Formula 1.48 might be interpreted in the following way (see also Fig. 1.5):

The one-dimensional Fourier transform $\tilde{F}(\mathbf{n}, u)$ of the projection $F(\mathbf{n}, p)$ on \mathbf{n} of the object function $f(\mathbf{x})$ is equal to the slice in the two-dimensional Fourier transform $\tilde{f}(\mathbf{k})$ of the object, taken along the line $\mathbf{k} = u\mathbf{n}$ through the origin in the Fourier domain.

From knowledge of the Radon transform $F(\mathbf{n}, p)$ for all possible values of \mathbf{n} and p one can calculate the Fourier components $\tilde{f}(u\mathbf{n})$ by the use of equation 1.48.

In principle, the object function could now be calculated by two-dimensional inverse Fourier transform of $\tilde{f}(u\mathbf{n})$. The inevitable discretization of the problem in practical implementations (limited spatial and angular sampling rate) would require an interpolation of the complex function $\tilde{f}(u\mathbf{n})$ onto a cartesian grid in order to calculate the inverse Fourier transform. In practice, this interpolation turns out problematic and a different approach, called *filtered backprojection* is adopted. The basis formula of the filtered backprojection algorithm is easily derived by expressing the Fourier representation of $f(\mathbf{x})$ in cylindrical coordinates (u, Φ)

$$f(\mathbf{x}) = \frac{1}{(2\pi)^2} \int_0^{2\pi} d\Phi \int_0^\infty \tilde{f}(u \cos \Phi, u \sin \Phi) e^{-iu\mathbf{n} \cdot \mathbf{x}} u du. \quad (1.49)$$

Using the relation 1.48 we can rewrite 1.49 in the form

$$f(\mathbf{x}) = \frac{1}{(2\pi)^2} \int_0^\pi d\Phi \int_{-\infty}^\infty \tilde{F}(\mathbf{n}, u) e^{-iu\mathbf{n} \cdot \mathbf{x}} |u| du \quad (1.50)$$

or

$$f(\mathbf{x}) = \frac{1}{(2\pi)^2} \int_0^\pi Q(\mathbf{n} \cdot \mathbf{x}) d\Phi \quad (1.51)$$

where

$$Q(\mathbf{n} \cdot \mathbf{x}) = \int_{-\infty}^{\infty} \tilde{F}(\mathbf{n}, u) e^{-i u \mathbf{n} \cdot \mathbf{x}} |u| du \quad \text{and} \quad \mathbf{n} \cdot \mathbf{x} = x \cos \Phi + y \sin \Phi . \quad (1.52)$$

Equation 1.51 can be interpreted in the following way: the object function $f(x, y)$ is synthesised from the sum of filtered projections $Q(\mathbf{n} \cdot \mathbf{x})$. The values of $Q(\mathbf{n} \cdot \mathbf{x})$ are *backprojected* into the image plane: each point (x, y) satisfying $\mathbf{n} \cdot \mathbf{x} = \text{const}$ receives the same contribution $Q(\mathbf{n} \cdot \mathbf{x})$. This approach allows interpolation to be performed in the spacial domain during the backprojection step rather than in the frequency domain.

Chapter 2

Instrumentation

Quantitative X-ray imaging experiments require a homogeneous, monochromatic X-ray beam. As will be shown in § 2.2.1, perfect single crystal Si monochromators are still unchallenged in terms of beam quality. However, the spectral bandwidth as delivered by conventional Si (111) double crystal monochromators ($\Delta\lambda/\lambda \cong 10^{-4}$) is at least one order of magnitude narrower than the one actually required¹ for the type of imaging experiments described in this work. This, together with the fact, that the number of photons necessary to image with a constant signal to noise ratio scales with the surface of the picture elements (pixels) results in unpractically long exposure times (up to minutes for a single projection) and rules out routine tomographic imaging with pixel sizes below one micrometer.

This situation (limited applicability of high-resolution tomographic imaging due to impractically long scan times) was the starting point for our efforts, to optimize and improve the experimental set-up.

The following possibilities were considered and realized in collaboration with different ESRF support groups:

- Increase of the detective quantum efficiency of the high resolution detector system (see § 2.3.2). Undoubtedly the best approach, as it helps at the same time to increase the signal and to reduce the dose on the sample. The latter point is of crucial importance in life sciences.
- Increase of the incoming photon flux (upstream of the monochromator) by switching to an undulator source. This possibility became available quite recently - the new devices are currently under commissioning.
- Increase of the energy bandwidth. Large bandwidth synthetical multilayers (§ 2.2.2), prepared in the ESRF optics group, allowed us to increase the photon flux by two orders of magnitude, compared to the conventional Si(111) double monochromator set-up.

Without the use of the multilayer monochromator, our in-situ observations of grain boundary wetting (see. § 4.5.1) and more generally, most of our high resolution tomographic imaging experiments would not have been possible.

Before we discuss the characteristics and the optimization of the monochromator and the detector system, we will give a short introduction to synchrotron radiation: hard X-ray phase contrast imaging became only of easy and practical due to the coherence properties of third generation synchrotron beams.

¹high energy resolution is e.g. required for spectroscopic imaging (XANES) or K-edge subtraction imaging.

2.1 Source characteristics

Synchrotron radiation is the electromagnetic radiation emitted by relativistic, charged particles (usually electrons or positrons) forced on curved trajectories. The outstanding characteristics of modern third generation synchrotron sources result mainly from improvements in the control of the electron trajectory and the development of multipole insertion devices which act as sources of intense electromagnetic radiation.

The characteristic parameters of a storage ring are usually expressed in terms of [Rao93]

- the **critical wavelength** λ_c . The spectrum emitted by a charged particle which is deviated by a static magnetic field B depends on its energy $E = \gamma m_e c^2$, on the radius of curvature $\rho = \gamma m_e c / qB$ and on the vertical angle θ_v with respect to the plane of the orbit. The critical wavelength is defined such, that half of the energy is radiated at wavelength higher than λ_c (case of a bending magnet):

$$\lambda_c = \frac{4\rho}{3c\gamma^3}. \quad (2.1)$$

- the vertical (z) and horizontal (x) **emittance** of the electron beam $\epsilon_i = \sigma_i \sigma'_i$, ($i = x, z$). ϵ is a constant of motion (phase space density) which relates the width σ and angular divergence σ' of the electron beam at each point of the trajectory.
- the **brightness** is a measure for photon flux impinging on the sample. It is defined as the number of photons emitted per second in a spectral bandwidth $\Delta\lambda/\lambda = 10^{-3}$ and per solid angle 1 mrad^2 .
- the **brilliance** is defined as

$$\text{Brilliance} = \frac{\text{Brightness}}{\sigma_x \sigma_z}$$

and is a measure for the achievable photon density in a focal spot if the source is imaged with focusing optics.

The vertical emittance of the electron beam, $\epsilon_z = \sigma_z \sigma'_z$, is in the order of $10 \text{ pm}\cdot\text{rad}$ at the ESRF, and brilliances higher than $4 \cdot 10^{20}$ (photons/s/mm²/0.1%BW/mrad²) have been measured for a 5 m long undulator (U34) [Hig99]. For comparison: the brilliance of rotating anode X-ray sources is in the order of 10^9 .

The high brilliance of synchrotron radiation can be understood as a result of the Lorentz transformation which yields an apparent opening angle $\Psi = 1/\gamma$ of the radiation emitted by a single particle. In the case of the ESRF, which operates an electron storage ring at an energy of 6 GeV we obtain

$$\gamma = \frac{E}{E_0} = \frac{1}{\sqrt{1 - v^2/c^2}} = 11740 \quad (2.2)$$

hence a natural collimation of the radiation (in the vertical direction) in the order of $83 \mu\text{rad}$. In the case of a bending magnet, the radiation is linearly polarized in the plane of the electron orbit ($\theta = 0$). Additional perpendicular polarization states appear for $\theta \neq 0$ and result in an elliptical polarization above and below the plane of the orbit.

The characteristics of the radiation emitted by an insertion device, i.e. a periodic array of alternating magnetic fields depend further on the K value, which is a measure for the amplitude

of the angular deviation α of the electron trajectory with respect to the natural opening $1/\gamma$ of the radiation:

$$\alpha(s) \simeq \frac{K}{\gamma} \cos\left(\frac{2\pi s}{\lambda_u}\right) \quad \text{with} \quad K = \frac{e}{2\pi m_e c} \lambda_u B_0 \quad (2.3)$$

where λ_u is the period of the insertion device and s denotes the position along the electron trajectory. In the so-called wiggler regime ($K \gg 1$), the angular deviation of the electron trajectory α is larger than the natural opening $1/\gamma$ of the cone within the particle radiates. In this case the intensities emitted by the individual (half-) wiggles sum up incoherently and the total intensity in the direction of the axis of the device is therefore approximately $2N$ times the intensity of a bending magnet (N = number of periods of the device).

In the undulator regime ($K \leq 1$, $\alpha < 1/\gamma$) the radiation emitted by an electron is able to interfere and this results in a discrete energy spectrum and a highly collimated emission along the axis of the device.

For our work on coherent imaging, we were particularly interested in the transverse source size. This parameter defines the coherence properties of the radiation and will be discussed in more detail in the next section.

2.1.1 The source size

The transverse source size depends on the type and length of the insertion device, the distribution of the electron position within the device (i.e. the emittance) and on the angle of observation with respect to the device axis.

Distribution of the electron position

The stochastic nature of the radiation process, combined with the dispersion of the electron optics lead to an oscillation of the electron trajectories around the ideal orbit in the storage ring (betatron oscillations). The width σ of this distribution is given by the position dependent beta-function and an additional dispersion correction in the horizontal plane:

$$\sigma_i(s) = \sqrt{\epsilon_i \beta_i(s) + (\sigma_E D_i(s))^2} \approx \sqrt{\epsilon_i \beta_i(s)} \quad (2.4)$$

$$\sigma'_i(s) = \sqrt{\epsilon_i \gamma_i(s) + (\dot{D}_i(s) \sigma_E)^2} \approx \sqrt{\frac{\epsilon_i}{\beta_i(s)}} \quad (2.5)$$

$$\gamma_i(s) = \frac{4 + \dot{\beta}_i(s)}{4\beta_i(s)} \quad (2.6)$$

i	x or z
ϵ_i	emittance of storage ring
$\beta_i(s)$	beta function of storage ring
$D_i(s)$	dispersion function of storage ring
σ_E	relative energy spread

So far we considered only the effect of the electron beam. There are other contributions resulting from the finite length L and the lateral extent and divergence of the electron trajectory

	horizontal	vertical	
ϵ_i	3.9	0.01	[nm rad]
$\beta_i(s)$	0.5	2.7	[m/rad]
$\dot{\beta}_i(s)$	0	0	[1/rad]
$D(s)$	0.04	0	[m]
σ_i	57	10	[μm]
σ'_i	88	4	[μrad]

Table 2.1: Typical values for the electron beam in a low beta section of the ESRF. The vertical beam position is not affected by dispersion effects, however coupling with the horizontal magnetic lattice and the radiation loss result in a small vertical emittance.

within the device [Rao93]

$$\Sigma_z = (\sigma_z^2 + L^2\theta_z^2)^{\frac{1}{2}} \quad (2.7)$$

$$\Sigma_x = (\sigma_x^2 + (\frac{K\lambda_u}{\gamma\pi})^2 + L^2\theta_x^2)^{\frac{1}{2}} \quad (2.8)$$

L length of the insertion device

λ_u length of one period of the device

θ_i angle with respect to the device axis

We will now consider the specific case of the wiggler of ID19 which is installed in a low beta straight section of the storage ring. The characteristic parameters of this device are $\lambda_u = 0.15$ m, $N=5.5$ and $L=0.825$ m. The alternating magnetic field is produced by permanent magnets and its strength can be varied between 0 and 1.4 T by changing the gap between the jaws housing the magnets. The maximum critical energy is 33.5 keV and corresponds to a K value of 20 [BDZ93]. An large source to sample distance of 145 m has been chosen in order to produce an extended (40 mm x 14 mm), homogeneous beam for imaging of large objects. When working close to the axis of the device ($\theta \cong 0$), the last term in equations 2.7 and 2.8 can usually be neglected and the remaining contributions yield the following source sizes (fwhm, $K=14$) and lateral coherence length $l_c = \lambda l/2s$ for a typical wavelength of $\lambda = 1$ Å:

$$\Sigma_z \approx 24 \mu\text{m} \quad l_c = 270 \mu\text{m} \quad (2.9)$$

$$\Sigma_x \approx 190 \mu\text{m} \quad l_c = 34 \mu\text{m} \quad (2.10)$$

The initial design of ID19 was optimized for diffraction topography, a technique which requires a large homogeneous beam. In the mean time, about 50% of the beamtime is dedicated to high resolution micro-tomography, where the typically required beam size is only in the order of 1 mm^2 and the divergent wiggler source is not well adapted. The recent installation of two undulators in the same straight section where the ID19 multipole wiggler is located, will allow a more efficient use of the available photon flux. Future users will have the choice to switch between one of the three devices, which fits best to the experimental needs in terms of the required energy and beam size.

2.2 Choice of the monochromator

2.2.1 Silicon monochromators

The availability of large, dislocation free Silicon single crystals and well developed mechano-chemical polishing methods make Silicon the first choice for X-ray optical elements like monochro-

mators, mirrors and focussing elements. Monochromatization is achieved by setting two perfectly flat Si (111) crystals to Bragg diffraction. The dispersion free, symmetrical ($n, -n$) Bragg arrangement is chosen because it does not introduce additional divergence on the beam [ECB⁺98]. In practice, the double crystal arrangement is slightly detuned from the exact Bragg condition in order to suppress the higher harmonic content² of the radiation exiting the second crystal.

Extreme care was taken to ensure the optimum surface finish of the perfectly flat crystal surfaces. Any kind of surface irregularities (slope errors, scratches, contamination, dust) lead to detrimental degradation of the field uniformity. The current state of the art is demonstrated in Fig. 2.1 a, which shows the image of the monochromatic beam (20 keV) as delivered by the Si double crystal monochromator. Most of the remaining, spurious contrast is caused by surface irregularities and dust contamination of the beam windows upstream the monochromator. The typical modulation of the normalized beam profile is below 5 %, and may reach up to 10 % in the case of dust contaminations (see profile Fig. 2.1 b). From a practical point of view, the fixed exit, double crystal monochromator allows to select and optimize the energy with great ease: automated translations of the crystals ensure, that the beam is delivered with a constant vertical offset and parallel to the incoming white beam. Moreover, the length of the crystals is sufficient to provide the maximum available vertical beamsizes up to energies of 40 keV, thus allowing for convenient imaging of large objects (up to 15×40 mm²).

2.2.2 Multilayer monochromators

The applicability of synthetically manufactured multilayer devices as beam deflecting and focusing systems as well as their possible use as high throughput monochromators is currently intensively investigated at the ESRF [ZMH⁺99]. Concerning imaging applications their interest arises clearly from the possible gain of two orders of magnitude in flux compared to the conventional double crystal set-up. The gain results from the increase of the relative energy bandwidth, which depends on the order of diffraction m and on the number of periods NJ of the device (kinematic approximation) [Mic86]

$$\frac{dE}{E} = 2\sqrt{\frac{\ln 2}{\pi}} \frac{1}{mN} \quad (2.11)$$

The characterization of these devices in terms of homogeneity, higher order harmonics suppression, their resistance against irradiation, as well as their effect on the coherence properties of the radiation was therefore of primary interest.

First imaging experiments with a Ru/B_4C multilayer (100×25 mm Si substrate, 65 periods ($\Lambda = 41.9 \text{ \AA}$, $\Delta\lambda/\lambda = 3\%$, peak reflectivity $R \cong 0.8$ at 10 keV) were encouraging. Despite the strong degradation of the beam homogeneity due to long-range surface height errors (see Fig. 2.1 c,d), these devices are now routinely used for high-resolution tomographic and real-time imaging experiments in absorption mode. It turned out a workable solution, to take regular updates of the incoming beam (flatfield images) in order to correct for the slowly changing beam profile (decrease of electron current, thermal and mechanical instabilities,ldots).

The extreme sensitivity against long-range surface slope errors arises from the fact that the deposited diffraction coating follows the slope of the substrate and will lead to variations in beam direction and energy. The height variations Δz lead to phase shifts $\Delta\phi = \frac{4\pi}{\lambda}\Delta z \sin\theta_B$

²at a given angular setting θ_B all wavelength corresponding to allowed reflections are passed through the set-up leading to considerable (few percent) high energy contamination of the radiation.

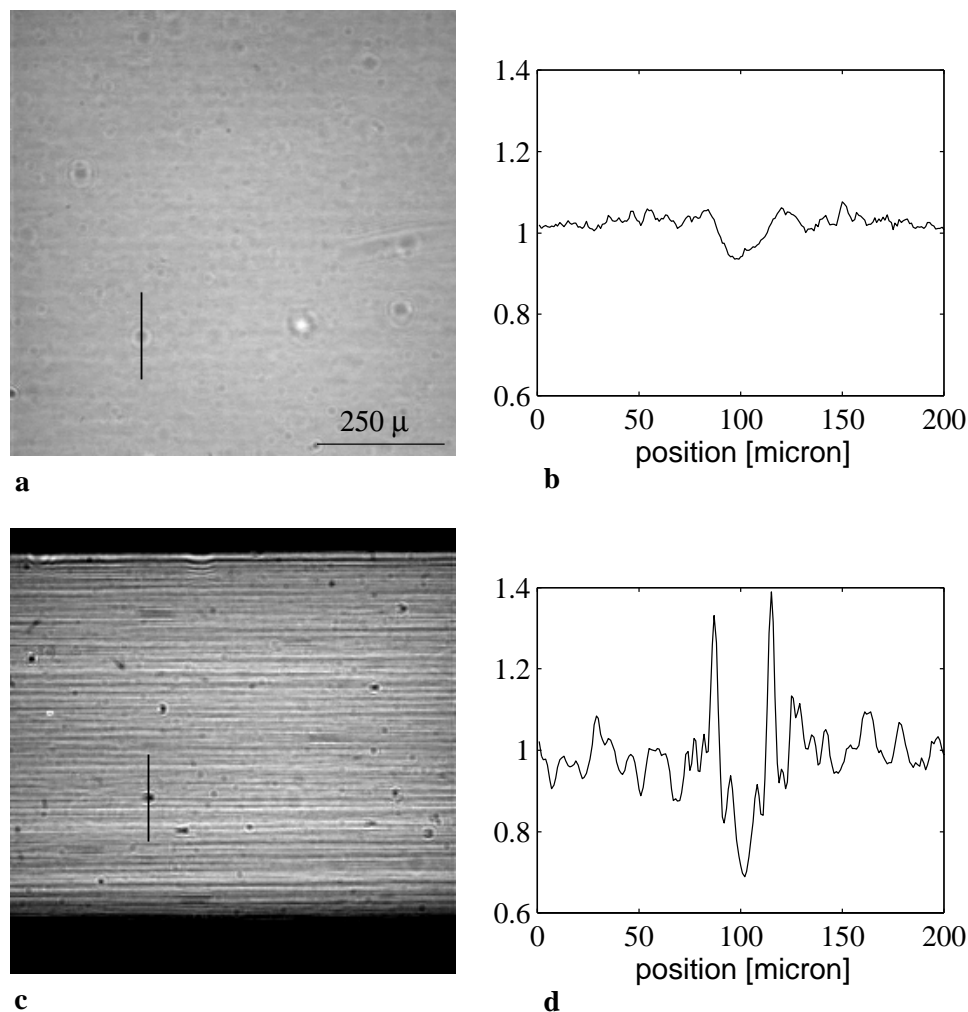


Figure 2.1: a) Image of the monochromatic beam (18 keV) as delivered by the Si(111) double crystal monochromator situated 5 m upstream of the camera. Most of the observed contrast is due to inhomogeneities and defects (pores, dust) on the polished beamline windows. b) plot of the normalized intensity through one of the defects. c) Monochromatic beam (18 keV) as delivered by a 100 mm Ru/B₄C multilayer (diffracting in the vertical direction), situated 2.5 m upstream of the camera. The beam profile shows 10-20% modulations in the vertical direction and even stronger contrast at isolated surface defects of the multilayer

and result in the pronounced intensity modulations after propagation to the detector, which is positioned typically 2-3 m downstream of the device. Extreme care has to be taken to prevent dust contamination of the device surface.

The small Bragg angle ($\theta_B = 0.43$ deg at 20 keV) results in strong compression of the image in direction of the diffraction vector. This effect is more pronounced at higher energies and limits the field of view to $l = L \sin \theta_B$ (with $L =$ length of the crystal). For the case of a 100 mm long substrate and an energy of 20 keV this results in a maximal beam size of 0.7 mm in the vertical direction.

Due to the small incident angles, a refraction correction has to be taken into account for

Bragg's law:

$$m\lambda = 2d\sqrt{n^2 - \cos^2(\theta_B)} \quad (2.12)$$

where n is the refractive index of the multilayer.

Precautions have to be taken in order to prevent low energy contamination of the diffracted beam, especially when working at higher energies i.e. small grazing angles. As can be seen from Fig. 2.2, the tail of the specular reflection may lead to a significant contribution in the order of several percents. Putting additional aluminium filters in the beampath allows to suppress the low energy content and has proven a workable solution.

Compared to the fixed exit double crystal set-up, the use of a multilayer monochromator is currently less convenient from a practical point of view: a change of energy results in a change of beam direction, position and size, hence implying realignment of the tomographic set-up. In order to take images at different defocus distances, an additional vertical movement of the detector is required. The redesign of the tomographic instrument (§ A) and the foreseen permanent installation of the multilayer account for these special requirements and will ease the routinely use of this device in the future.

2.2.3 Preservation of coherence

In order to assess the deterioration of the spatial coherence by optical elements in a quantitative way, we applied a method based on the optical Talbot effect [Tal36, CGM⁺97, Clo99]. The Talbot effect describes the peculiar property of a coherently illuminated, periodic object, to reproduce identical images at distances corresponding to integral multiples of a characteristic distance $D_T = 2a^2/\lambda$ where a is the period of the object.

The origin of the periodicity in the propagation direction is easily understood when reasoning in frequency space. The periodic object can be described as a Fourier series with frequencies

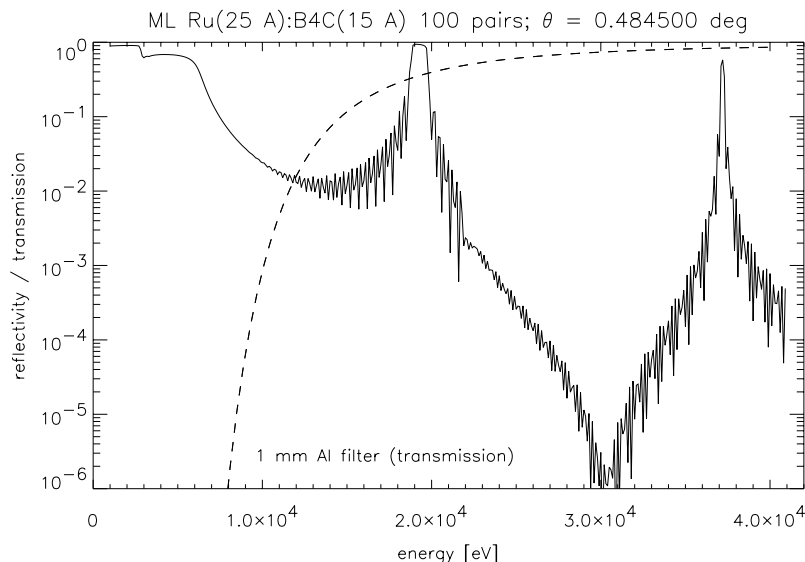


Figure 2.2: Reflectivity of a Ru/B₄C multilayer at a typical setting of $\theta_B = 0.48^\circ \approx 19.2$ keV. Polished Al filters are used to suppress low energy contamination due to the wing of the specular reflection. The dashed line shows the transmission as a function of energy by a 1 mm thick Al filter.

$f = m/a$. The propagator (equ. 1.25) $\exp i\pi\lambda D f^2 = \exp i\pi\lambda D \frac{m^2}{a^2}$ will be unaltered if the distance D changes by a multiple of $D_T = 2\frac{a^2}{\lambda}$. Particular contrast behaviour is expected also at other distances, noteworthy at $D_T/2$, where the periodic structure is imaged with a shift of half a period. In the case of a pure phase grating, no contrast is observed at zero distance (and multiples of $D_T/2$) and maxima of contrast are expected at distances $D = D_T/4 + pD_T/2$, where p is an integer number [Gui71].

Illumination by a partially coherent beam leads to a decrease of image contrast in the self-images with increasing distance from the periodic object. This decrease is readily observed in Fig. 2.3 where images of a phase grating of $6.35\mu\text{m}$ period are shown for reduced Talbot distances $D/D_T = 0, 1/4, 1/2$ and $3/4$. Quantitative assessment of this decrease by Fourier analysis allows

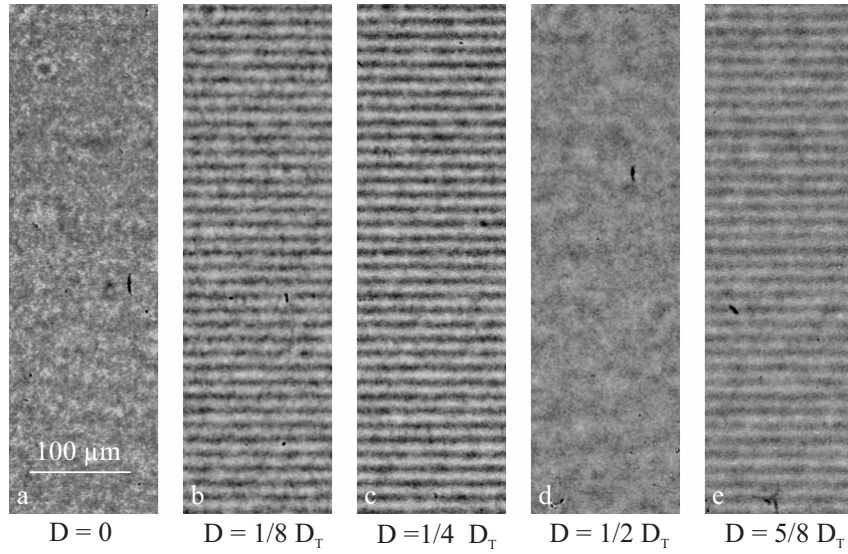


Figure 2.3: Fractional talbot images obtained from a periodical phase grating with $12.7\mu\text{m}$ period at an X-ray energy of 18 keV. The quantitative assessment of the drop of contrast at multiples of $D_T/2$ (e.g. from the images (b) and (e)) can be used to determine the degree of coherence (from [Clo99]).

to measure directly the degree of coherence $\gamma_{\text{inc}}(\mathbf{r}_2 - \mathbf{r}_1)$ (see § 1.4.1). A detailed description of this method is found in [Clo99]. Compared to other techniques which deduce the degree of coherence from the visibility of interference fringes from a known object, this method has the advantage to be independent of the object and the detector response: the decrease of contrast is analysed for the same spatial frequency as a function of the propagation distance. From equations 1.33 and 1.15 we obtain the following expression for the m -th harmonic component of the intensity spectrum:

$$I^m = \tilde{R}\left(\frac{m}{a}\right)\gamma_{\text{inc}}^c\left(\lambda D \frac{m}{a}\right)I_{\text{coh}}^m \quad (2.13)$$

Building the ratio of the m -th harmonic at distances D_0 and $D_0 + D_T$ yields:

$$\left| \frac{I^m(D_0 + pD_T/2)}{I^m(D_0)} \right| = \left| \frac{\gamma_{\text{inc}}\left((D_0 + pD_T/2)\frac{m}{a}\right)}{\gamma_{\text{inc}}\left(\lambda D_0 \frac{m}{a}\right)} \right| \quad (2.14)$$

Instead of a successive evaluation of equation 2.14 at distances corresponding to multiples of $D_T/2$ we adopted a model, describing the beam as an incoherent superposition of plane waves

with a gaussian angular distribution

$$S_\alpha(\theta) = \frac{1}{\sqrt{2\pi}\sigma_\alpha} \exp -\frac{\theta^2}{2\sigma_\alpha^2}. \quad (2.15)$$

Such a description is equivalent to the model of a Gaussian source of size $\sigma_s = l \cdot \sigma_\alpha$ where l denotes the source to sample distance. The van Cittert Zernike theorem yields in this case:

$$\gamma_{\text{inc}}(\lambda D \frac{m}{a}) = \tilde{S}_\alpha(D \frac{m}{a}) = \exp -2(\pi\sigma_\alpha D \frac{m}{a})^2 \quad (2.16)$$

The parameter σ_α describes the partial coherence in terms of the angular divergence of the radiation. It can be obtained from two measurements at distances D_0 and $D_p = D_0 + pD_T/2$ by combining equations 2.14 and 2.16:

$$\sigma_\alpha = \frac{a}{\sqrt{2\pi}\sqrt{D_p^2 - D_0^2}} \left(\ln \left| \frac{I^{(1)}(D_p)}{I^{(1)}(D_0)} \right| \right)^{\frac{1}{2}} \quad (2.17)$$

Table 2.2.3 summarizes the values of σ_α we obtained for the angular source size (vertical direction) for different monochromator set-ups. Surprisingly, the values obtained for the double crystal monochromator and the 100 mm RuB₄C multilayer are quite similar, indicating that neither of both devices would be preferable in terms of coherence preservation. This discrepancy from the expected behaviour could be experimentally attributed to vibrations induced by the water cooling system of the double crystal monochromator. Using an uncooled, horizontally diffracting Si(111) monochromator, a value close to the theoretically expected value of 0.1 μrad (fwhm) was obtained.

set-up	Si(111) double crystal	Si(111) single crystal	multilayer
σ_α	1.2 μrad	0.2 μrad	1.5 μrad

The large value of $\sigma_\alpha = 1.5 \mu\text{rad}$ for the multilayer reveals the stringent requirements concerning surface quality for the substrates. Further improvement of multilayer monochromators for imaging applications is therefore strongly connected to progress in substrate characterisation and preparation techniques. Two different methods for precise X-ray surface metrology were recently proposed and implemented by Cloetens. These techniques provide Ångstrom height resolution combined with high lateral resolution ($\cong 0.1 \text{ mm}$) over the entire length of the substrate (100-300 mm) and close the lack of adequate characterisation techniques at this particularly important lengthscale. Combined with precise ion beam etching techniques this might pave the way for further improvement of these devices.

Different requirements for absorption and phase imaging

Apart bandwidth considerations, the choice of the monochromator is also determined by the extent the different imaging methods are affected by imperfections in the beam profile. A nonuniform intensity distribution makes the set-up extremely sensitive to submicrometer displacements of the different components with respect to each other: moderate temperature drifts of only half a degree (current level of stabilization in the experimental hutch) might already lead to displacements in the order of 1 μm due to differences in the thermal expansion of the mechanical components. Regular update of the incident beam profile (so called *flat-field* images),

and interpolation between successive images helps to reduce artifacts resulting from this type of misalignment.

Working at a single distance (i.e. in absorption or edge detection mode) the non uniformity of the flat-field is less problematic. The use of multilayers open the way for time resolved, and high resolution tomographic imaging in this case.

On the other hand, multilayers are still of limited applicability for quantitative phase imaging methods: in addition to the increase of the apparent angular source size, the surface slope errors result in noticeable image deformation at larger distances from the sample. Accurate alignment of the images, a prerequisite for stable operation of numerical phase retrieval algorithms, gets increasingly difficult, especially when aiming for highest spatial resolution, where the large bandwidth of multilayers would be most beneficial.

2.3 The high-resolution detector system

Photographic film is, despite some known disadvantages like the low dynamic range ($\cong 300$), the non-linear response and the complicated off-line processing and handling, still widely used in medical and industrial X-ray imaging. This is mainly due to the fact, that it combines excellent spatial resolution (down to $1 \mu\text{m}$ in the case of special holographic film) with a nearly unlimited field of view.

X-ray micro-imaging at synchrotron sources on the other hand is mainly concerned with high-resolution imaging of small, typically millimeter sized objects. Among different concepts for X-ray imaging detectors like image intensifiers, image plates and active diode arrays, systems based on scintillators and charge coupled device (CCD) cameras have proven the best solution for the majority of imaging applications. They have replaced film and provide images with comparable resolution directly in digitized format. The high dynamic range, linearity and real-time imaging capabilities of state of the art detector systems make them the ideal tool for quantitative, real-time and three-dimensional imaging techniques.

After a description of the imaging process in these detector systems we will give a short description of their different components (i.e the scintillator screen, the optics and the CCD camera). The imaging performance of the entire system will be characterized in terms of the line spread function (LSF), modulation transfer function (MTF) and the detective quantum efficiency (DQE).

2.3.1 X-ray imaging with thin film scintillators

For the conversion of X-rays into visible light two alternatives are currently available at ID19: powder phosphor screens $\text{Gd}_2\text{O}_2\text{S:Tb}$ and transparent scintillator crystals $\text{Y}_3\text{Al}_5\text{O}_{12}:\text{Ce}$ (YAG) and $\text{Lu}_3\text{Al}_5\text{O}_{12}:\text{Eu}$ (LAG). We will concentrate on the discussion of the imaging process with transparent screens as this variant provides the best spatial resolutions measured so far ($< 1 \mu\text{m}$). The typical set-up of the detector system including converter screen, optics and camera is shown in Fig. 2.4.

The imaging process can be described in the following way: a parallel X-ray beam is partially absorbed in the active region of the scintillator and generates identical ³ visible light images across arbitrary planes (z) of the active layer. The numerical aperture (NA) of the objective

³apart from intensity changes due to absorption

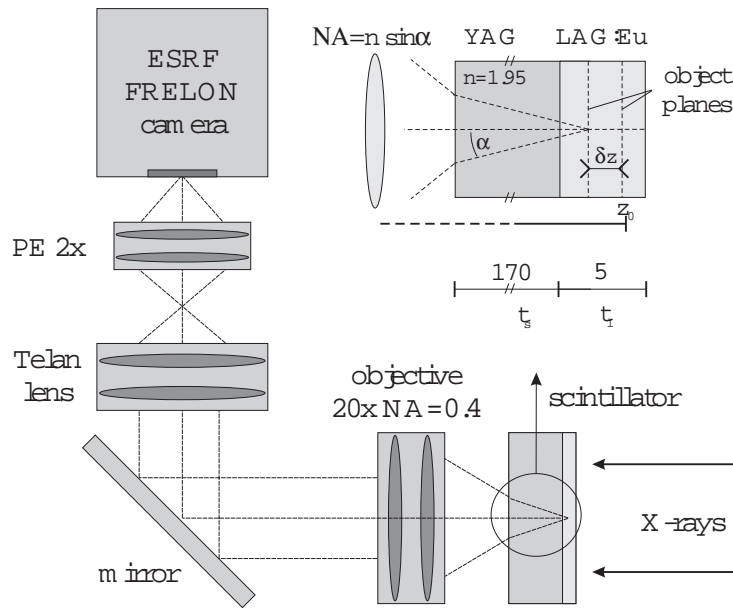


Figure 2.4: Components of the high resolution detector system. Images produced at different defocus δz are projected on the CCD camera. The mirror is included in order to prevent direct irradiation of the CCD. (PE designs a photo eyepiece.)

lens is adapted to the thickness of the active region of the converter screen. Because of the infinite working distance of the objective lens, a second lens (Telan lens) is required to create an image at finite distance. Depending on the set-up, this image is further magnified by a photo eyepiece (PE) before it reaches the CCD.

Clearly, the design has to compromise between good efficiency and high-resolution. Good efficiency helps to limit the radiation dose received by the sample and suggests the use of thick converter screens. High resolution on the other hand requires thin layers and the optimum configuration has to trade off between both requirements.

The ultimate spatial resolution of the set-up may be limited by one of the following factors:

Spatial distribution of the deposited X-ray energy

The output of visible light is proportional to the X-ray energy deposited in the active region of the converter screen. However, even in the case of a point like excitation of the screen (pencil beam of X-rays), energy transport of the secondary radiation (photo-electrons, Auger electrons, secondary X-rays, Compton scattering) will result in a radial distribution function of the deposited energy in an extended region around the primary interaction site. This radial distribution function depends on the composition and thickness of the layer and substrate as well as on the energy of the incoming X-rays. Monte-Carlo simulations have been performed for the case of a 100 μm thick YAG crystal and for different X-ray energies [KRSS98]. Radial distribution functions for the energy deposited in the 5 μm thick surface layer of the crystal were calculated for different X-ray energies (Fig. 2.5). These simulations indicate a rapid initial decay over the first few hundred nanometers. The initial decay is similar for all energies and was attributed to short range Auger electrons. Pronounced tails, attributed to long range photoelectrons and characteristic X-rays, start to limit the resolution at energies above $\cong 10$ keV.

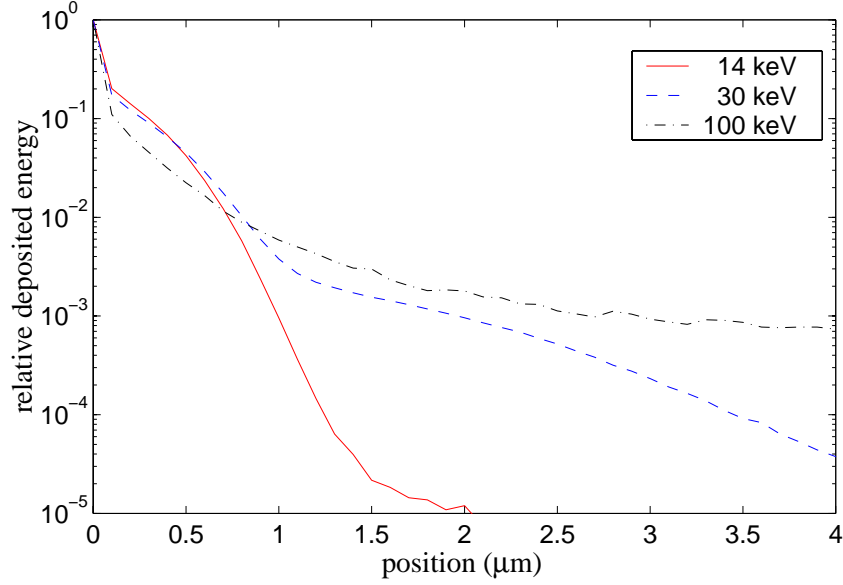


Figure 2.5: Monte-Carlo simulation of the radial distribution function of energy deposition in a 5 μm surface layer of a 100 μm thick YAG substrate (from [KRSS98]).

Depth of focus

As mentioned earlier, we are summing up the intensity distributions across different object planes in the scintillator. This will lead to a deterioration of the frequency response of our system due to defect of focus. Hopkins derived the following approximation for the transfer function of a defocussed optical system [Hop55]

$$\tilde{R}(f) \approx 1 - \frac{2\lambda_v f}{\pi NA} - \frac{1}{2}\pi^2 (NA)^2 f^2 \left(\frac{z}{n_v}\right)^2 \quad (2.18)$$

and averaging over the thickness t_l of the scintillator yields

$$\tilde{R}(f) \approx 1 - \frac{2\lambda_v f}{\pi NA} - \frac{\pi^2}{24} (NA)^2 \left(\frac{t_l}{n_v}\right)^2 f^2. \quad (2.19)$$

The last term in this expression corresponds to the defect of focus.

If we impose a certain design goal for the frequency response [Clo99], e.g.

$$R(f) > \epsilon_m \quad \forall f < f_m \quad (2.20)$$

we can solve equation 2.19 at $f = f_m$ for the layer thickness. Derivation with respect to NA yields finally the value of the numerical aperture which will yield the maximum layer thickness and consequently also maximum X-ray absorption under the constraint 2.20:

$$NA_{\text{opt}} = \frac{3}{\pi(1 - \epsilon_m)} \lambda_v f_m \quad (2.21)$$

and

$$t_{l,\text{opt}} = \frac{\sqrt{8}(1 - \epsilon_m)^{3/2}}{3} \frac{n_v}{\lambda_v f_m^2} \quad (2.22)$$

If we want to preserve a transfer function bigger than 0.5 for frequencies up to 500 line pairs per millimeter, we obtain an optimum layer thickness of 4.7 μm for a numerical aperture of NA = 0.5.

Spherical aberration

So far we neglected the spherical aberrations introduced by the substrate of the scintillator. The presence of the substrate with refractive index n_v leads to a shift of the apparent origin of the rays in the substrate. This focus shift depends on the thickness of the substrate t_b as well as on the angles θ_s (substrate) and θ_a (air) and equals

$$\Delta z = t_b \left(1 - \frac{\tan \theta_s}{\tan \theta_a} \right) \quad (2.23)$$

High numerical aperture microscope objectives are usually corrected for a fixed cover glass thickness of $t_{\text{cover}} = 170 \mu\text{m}$ and a refractive index of $n_{\text{cover}} = 1.5$. The YAG substrates used in the high-resolution set-up have a refractive index of $n_{\text{yag}} = 1.95$ and a thickness $t_{\text{yag}} = 180 \mu\text{m}$. The spherical aberration introduced by the discrepancy of the refractive index should be small compared to the thickness of the active layer t_l . For this we consider the following approximation of equation 2.23

$$\Delta z \approx t_b \frac{n_v - 1}{n_v} + t_b \frac{n_v^2 - 1}{2n_v^3} \sin^2 \theta_a \quad (2.24)$$

The difference of the angle dependent part, using ($\sin \theta_a \leq NA$) should be smaller than t_l . This yields the following condition for the acceptable thickness of the YAG substrate t_b :

$$\left| t_{\text{cover}} \frac{n_{\text{cover}}^2 - 1}{2n_{\text{cover}}^2} NA^2 - t_{\text{yag}} \frac{n_{\text{yag}}^2 - 1}{2n_{\text{yag}}^2} NA^2 \right| \leq t_l \quad (2.25)$$

In the case of the high-resolution set-up ($t_l = 5 \mu\text{m}$, $NA = 0.4$) we obtain $t_{\text{yag}} = [43-213] \mu\text{m}$, i.e. our substrate (t_{yag}) alone would not suffer from aberration. In practice we are obliged to add 1 mm of lead glass after the converter screen, in order to avoid degradation of the optics due to X-ray irradiation. It is this additional lead glass which introduces spherical aberration into our system.

Diffraction

The ultimate resolution will be limited due to visible light diffraction in the optical system. The theoretical limit (depends on definition) is [BW99] $r \approx \frac{\lambda_v}{NA}$ (corresponds to the second term in equation 2.19) and yields a value in the order of $1.3 \mu\text{m}$ if we consider the above example with $NA = 0.4$ and $\lambda_v = 550 \text{ nm}$.

2.3.2 Optimization of the converter screens

Each improvement of the absorption efficiency of the converter screen translates directly into a gain of the DQE (see section 2.3.4), hence reduced radiation dose for the sample and enhanced real-time imaging capabilities. One of the primary goals consisted therefore in the replacement of the commercial YAG:Ce scintillators (Crismatec, France) by layers with higher effective atomic number. The substitution of Yttrium ($Z=39$) by Lutetium ($Z=71$) yields $\text{Lu}_3\text{Al}_5\text{O}_{12}$ (LAG), a material of nearly identical crystalline structure⁴ but with considerably increased absorption. Figure 2.6 shows the absorption of different scintillator materials as function of energy. The

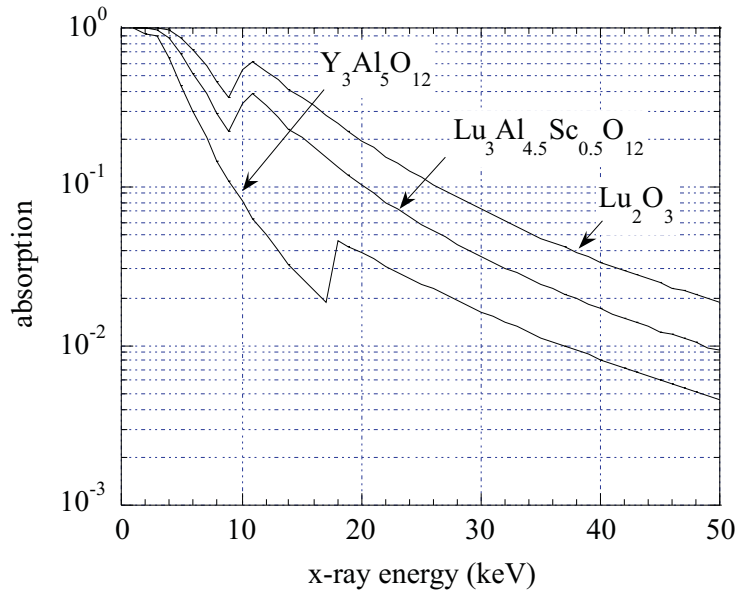


Figure 2.6: Absorption energy fraction for different, 5 μm thick converter layers. YAG, and recently also LAG layers are used in our optical set-up.

replacement of YAG by LAG is most beneficial in the energy range between the L edge of Lu (11 keV) and the K-edge of Yttrium (17 KeV).⁵

A two year research project between the ESRF and LETI⁶ was established in order to elaborate and optimize the process of liquid phase epitaxy of thin LAG layers on YAG substrates. Layers with different activators (Eu and Tb) and different activator concentrations were produced and analysed by A. Koch (ESRF detector group) in terms of homogeneity, time response and luminescence efficiency. The latter is defined as number of visible photons produced per absorbed X-ray energy.

The relative luminescence efficiencies of LAG:Eu and LAG:Tb compared to YAG:Ce (≈ 21000 ph/MeV) are 0.4 and 0.6, respectively.⁷ This reduces the gain in signal to 3.3 below the Y-edge, and 1.2 above. However, as will be shown in § 2.3.4, the relevant parameter is not the gain in signal, but rather the gain in absorption, as it has the strongest influence on the detective quantum efficiency.

LAG:Eu was finally chosen as scintillator material, mainly for two reasons:

1. The luminescence of LAG:Eu decays slightly faster than the one of LAG:Tb. A level of 10^{-3} is reached within 100 ms. This has to be compared to YAG:Ce, which shows pronounced afterglow and memory effects over several minutes at the level of 10^{-3} relative intensity [KPH⁺99]. The time decays are depicted in Fig. 2.7
2. The spectral emission of Eu (line emitter, principal wavelength: 580 nm and 700 nm) is better matched to the sensitivity of frontside illuminated CCD's and allows to filter part of the unwanted luminescence of the YAG substrate.

⁴the resulting lattice parameter mismatch compared to YAG is compensated by doping with Sc

⁵Even higher absorption could be expected from Lu_2O_3 powder phosphors. The fabrication of such layers requires special preparation methods and is currently investigated at INSA, Lyon.

⁶Laboratoire d'Electronique, de Technologie et d'Instrumentation, Grenoble

⁷measured with frontside illuminated CCD

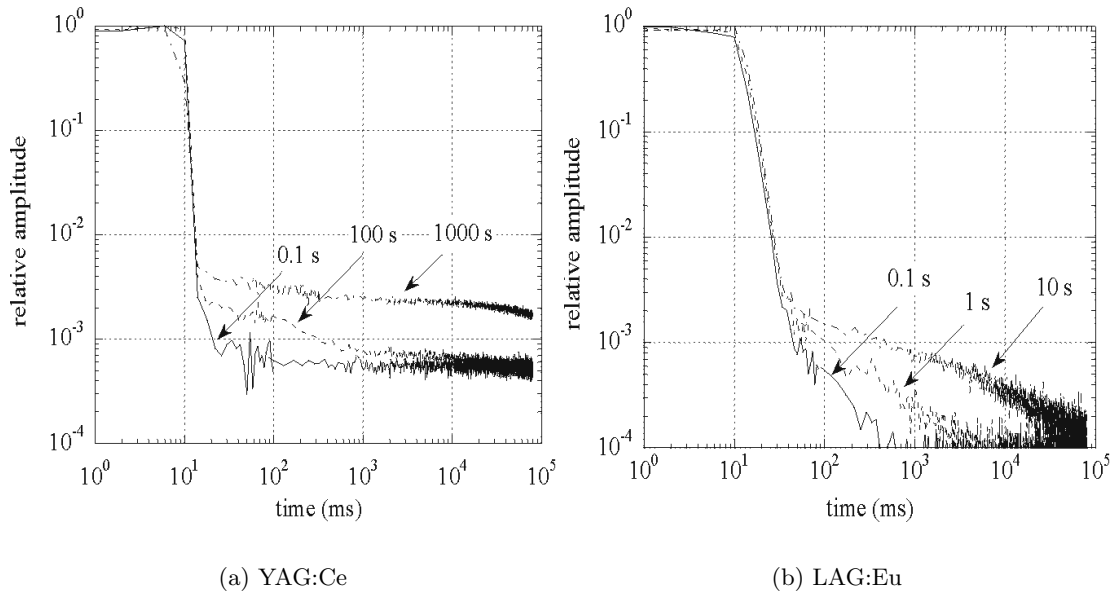


Figure 2.7: Time decay of the luminescence signal of YAG:Ce and LAG:Eu after different illumination times of 0.1, 100 and 1000 s. The shutter was closed at 10 ms. YAG:Ce screens display a pronounced afterglow at the level of 10^{-3} of the relative intensity [KPH⁺99].

The mentioned luminescence of the undoped YAG substrate is partly responsible for the pronounced tails in the LSF of the system: the light created in the substrate can not be focused on the CCD and gives rise to a background signal of non-negligible total intensity. The origin of the luminescence signal could be attributed to unwanted Ce impurities present in the undoped YAG substrate. The relative efficiency of undoped YAG compared to YAG:Ce varies between 1.4 and 6 % and is especially problematic in the case of thin active layers and high energies. A spectral filter with cutoff below the Eu emission (580 nm) reduces this unwanted contribution and a slight improvement of the LSF was experimentally observed.

2.3.3 Fast-readout, low-noise CCD camera (FRELON camera)

The electronic design of a CCD camera has to compromise between dynamic range and acquisition rate. A high acquisition rate requires a high bandwidth of the electronic circuits which in turn increases the noise and reduces the dynamic range. The high intensity of 3rd generation synchrotron beams allows to perform real time imaging experiments with typical exposure times in the order of 100 ms. Consequently, cameras with readout times of the same order are required in order to use effectively the available photon flux. Commercial cameras with fast readout are typically limited to 8 bit dynamic range - and inadequate for quantitative image analysis. Scientific grade slow scan cameras on the other hand provide up to 16 bit dynamic range with characteristic readout times of several seconds (typically 200 kHz pixel readout rate). This apparent discrepancy between available and required specifications led to the development of the ESRF FRELON camera. It is based on Thomson CCD chips (front-illuminated, full frame) of 1024^2 or 2048^2 pixels. The camera is cooled to -20°C (Peltier cooling) and has a very low dark current (i.e. thermally activated electrons) due to operation in MPP (multi-pinned phase) mode. Exposure times up to several minutes are possible without significant increase in noise. The images are coded to 16 bits depth and transferred by a fibre optic link to the

controlling workstation and further to one of the ESRF central file servers.

Figure 2.8 shows the non-linearity residual with respect to a linear fit for each of the four readout channels over the full dynamic range of 14 bit. The remaining non-linearity is smaller than 0.5% and essentially the same for the four output channels (see also table 2.3.3).

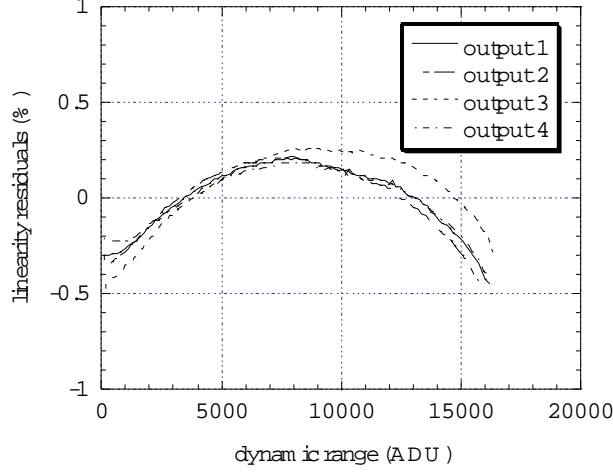


Figure 2.8: Residual of the non-linearity of the four output channels of the Frelon camera (MPP 1024). The plot extends over the full dynamic range of 2^{14} .

	Camera 1024	MPP Camera 1024	MPP Camera 2048
CCD chip	Th7896A	Th7896M	TH7899M
number of pixels	1024^2	1024^2	2048^2
pixel size	$(19 \mu m)^2$	$(19 \mu m)^2$	$(14 \mu m)^2$
sensitivity	$40 e^- / ADU$	$22 e^- / ADU$	$20 e^- / ADU$
readout noise	$44 e^-$ rms	$31 e^-$ rms	$20 e^-$ rms
full-well capacity	$600 \cdot 10^3 e^-$	$350 \cdot 10^3 e^-$	$320 \cdot 10^3 e^-$
dynamic range	13600	11300	16000
dark current	$200 e^- / s$	$3 e^- / s$	$3 e^- / s$
non-linearity	$\pm 0.2\%$	$\pm 0.4\%$	$\pm 0.3\%$
PRNU	0.3%	0.5%	0.5%

Table 2.2: Characteristics of the Frelon camera at the readout speed of 20 Mpixels/s (four channels in parallel). The non-linearity indicates the maximum error range over the complete dynamic range. The pixel response non-uniformity (PRNU) characterizes the non-uniformity in the gain of the different pixels. 1 ADU (analog digital unit) corresponds to 1 grey level.

In standard configuration, e.g. during tomographic acquisition, the camera is read by one channel with a pixel rate of 5 MHz within 200 ms. This mode provides the highest homogeneity and lowest noise level in the images. However, for time-resolved imaging experiments (see § 4.5.1), the camera can also be operated in four channel parallel readout mode, i.e. the image is divided into four quadrants and each of them is read by one of the four on-chip amplifiers. The readout time for a full frame (1024^2) reduces consequently to 50 ms (20 Mhz pixel rate). With typical exposure times in the order of 50 ms, frame rates of 10 images per second are achieved. Small differences in the gain of the different channels result in a slight degradation of the overall noise characteristics in this acquisition mode.

Moreover, permanent operation of the system close to the maximum frame rate requires an extremely fast computer storage medium which can handle continuous transfer rates of up to 40 MByte/s (20 MHz pixel rate, 2 bytes per pixel) and with a capacity in the order of 10 GByte. An intermediate solution consists in writing the images directly to the RAM of the controlling workstation (Sun Ultra 10, 1 GB RAM) and transferring them to a permanent storage medium after the experiment. The latter solution limits the number N_{\max} of recordable full-field (1024^2) images in a sequence to about 400 images in the current configuration. Note, that the operation time of the camera is not limited to N_{\max} images: the memory is organised in a ring-buffer, i.e. the images are periodically overwritten after a complete cycle of N_{\max} images, and the user can trigger either the start or the end of an interesting image sequence.

2.3.4 Detective Quantum Efficiency

The performance of a detector system is usually described in terms of the *quantum efficiency* (QE) and the *detective quantum efficiency* (DQE). The quantum efficiency, is defined as the number of created information carriers (electrons on the CCD) per incident X-ray photon:

$$QE = \frac{\text{Signal}_{\text{out}}}{\text{Signal}_{\text{in}}} = \frac{\text{number of electrons on the CCD}}{\text{number of incident X-ray photons}} \quad (2.26)$$

It is possible to factorise the expression for the QE in terms of the efficiencies of the involved processes

$$QE = \eta_{\text{abs}} \eta_{X/v} \frac{E}{E_v} \eta_{\text{col}} \eta_{v/e} = \eta_{\text{abs}} \eta_{X/e}(E) \quad (2.27)$$

The first factor, $\eta_{\text{abs}}(E, Z, t_l)$ denotes the absorption efficiency of X-rays by the luminescent screen. The latter depends on the X-ray energy as well as on the composition and thickness of the active layer (see Fig. 2.6). Only part $\epsilon_{X/v}$ of the deposited X-ray energy is used for creation of visible light photons with energy E_v . The optical system collects part $\eta_{\text{col}}(NA, n_v) \approx \frac{1}{4} \left(\frac{NA}{n_v} \right)^2$ of the generated photons and projects them on CCD chip where they create electron-hole pairs. The conversion efficiency of the last process is given by $\eta_{v/e}$. The different conversion steps may be summarized by a single conversion factor $\eta_{X/e}(E)$ which is equal to the number of electrons created per *absorbed* X-ray photon of energy E . Table 2.3 gives actual numbers for the case of two currently used optical set-ups, employing YAG and LAG based scintillator screens.

The QE can have values bigger than one (e.g. photomultiplier) and tells little about the noise characteristics of the detector. A more useful description of the detection process is therefore given in terms of the detective quantum efficiency (DQE), defined as the square of the signal-to-noise ratio (SNR) at the output compared to the square of the SNR at the input of the detector

$$DQE = \frac{\text{SNR}_{\text{out}}^2}{\text{SNR}_{\text{in}}^2} \quad (2.28)$$

The SNR at the input is given by Poisson statistics, i.e

$$\text{SNR}_{\text{in}} = \frac{n}{\sqrt{n}} = \sqrt{n} \quad (2.29)$$

where n is the number of incident photons per surface of the converter screen corresponding to one pixel on the CCD. Whereas an ideal, noise-less detector has a DQE of 1, actual detectors have smaller DQE's and require longer exposures in order to achieve the same SNR. In the case

material	YAG ($Y_3Al_5O_{12} : Ce$)	LAG ($Lu_3Al_{4.5}Sc_{0.5}O_{12} : Eu$)
thickness	25 μm	5 μm
substrate	0.5 mm YAG	170 μm YAG
λ_v	550 nm ($\bar{\lambda}$)	580 nm, 700 nm, ...
η_v	1.95	1.95
ρ_{layer}	4.55 g/cm ³	6.62 g/cm ³
$\eta_{\text{abs}}(17.5 \text{ keV})$	0.19	0.15
$\eta_{X/v}$	0.047	0.02
η_{col}	$6 \cdot 10^{-3}$	$1.05 \cdot 10^{-2}$
$\eta_{v/e}$	0.35	0.4
$\eta_{X/e}(17.5 \text{ keV})$	0.77	0.71
objective	Olympus UIS UPLFL	Olympus UIS LCPLFL
magnification, NA	M=10, NA=0.3	M=20, NA=0.4
second lens	Telan lens + PE 2x	Telan lens + PE 2x
effective pixelsize	0.97 μm	0.4 μm

Table 2.3: Characteristic properties of the two high-resolution set-ups employing transparent YAG and LAG scintillator crystals.

of a cascaded detector system, the DQE can be expressed as a function of the gain η_i and relative variance v_i of the individual processes [ZZ95]

$$DQE = (1 + v_1 + \frac{1}{\eta_1}v_2 + \frac{1}{\eta_1\eta_2}v_3 + \dots)^{-1} \quad (2.30)$$

with $v_i = \frac{1}{\eta_i}$ in the case of Poisson statistics and $v_i = \frac{1-\eta_i}{\eta_i}$ in the case of binominal statistics. This yields the following expression for the DQE [KRSS98]

$$DQE(E) = \eta_{\text{abs}}(E) \left(1 + \frac{1 + \eta_{ve}}{\epsilon_{X/e}(E)}\right)^{-1} = \frac{\eta_{\text{abs}}(E)\eta_{X/e}(E)}{1 + \eta_{ve} + \eta_{X/e}(E)} \quad (2.31)$$

It turns out, that the DQE is directly proportional to the absorption in the converter screen. The conversion efficiency $\eta_{X/e}(E)$ should ideally be larger than one. On the other hand, too large values will limit the maximum SNR in the image as the CCD can only collect a limited number of electrons ('full well capacity' N_{max}) during a single exposure:

$$SNR_{\text{out}}^2 = DQE \frac{N_{\text{max}}}{1 + \eta_{ve} + \eta_{X/e}(E)} \quad (2.32)$$

2.3.5 Determination of the transfer function

As pointed out at the end of section 1.3, the detailed knowledge of the detector transfer function is important for quantitative image analysis. If not corrected, the pronounced wings of the LSF lead to nonlinearities in the response of the detector system and hence to errors in the determination of the local absorption in the image. However, the determination of the modulation transfer function (MTF, $R(\tilde{f}, g)$) is not straightforward in the case of hard X-rays. A direct measurement would require the production of sinusoidal intensity modulations for the whole frequency range of interest.

An alternative method to determine the MTF makes use of its relation to the experimentally more accessible line spread function (LSF, $R_l(\theta, x)$) and edge spread function (ESF, $R_e(\theta, x)$).

Although both functions may depend on the inclination θ with respect to the axes of the image plane, the assumption of rotational symmetry is in general reasonably well fulfilled and reduces both functions to one dimensional functions of the parameter $r = \sqrt{x^2 + y^2}$. The LSF and ESF are related by an integral:

$$R_e(r) = \int_0^\infty R_l(r - r') dr' \quad \Leftrightarrow \quad R_l(r) = \frac{dR_e}{dr} \quad (2.33)$$

and the link between the LSF and the MTF is finally given by the Fourier transform

$$\tilde{R}(\omega) = |\mathcal{F}R_l(r)| \quad (2.34)$$

Measurement of the LSF and ESF

We applied to different methods to determine the LSF of the new high-resolution set-up:

- Direct measurement of the LSF by a means of precise slits (polished tungsten carbide blades).
- Measurement of the ESF across one of the blades of the precise slits. In this case the the LSF is obtained by derivation of the edge profile.

Figure 2.9 shows the LSF as determined from the measurements on the precise slits. The profile was obtained by averaging the intensity distribution over the small region depicted in the upper right corner of Fig. 2.9. The alternative approach, using a single blade of the slits as knife edge is illustrated in Fig. 2.10. Both measurements were performed at 10.8 keV.

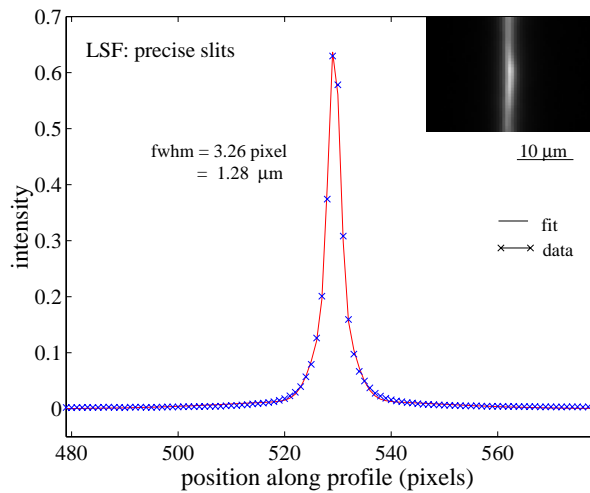


Figure 2.9: Line spread function of the high-resolution set-up ($5 \mu\text{m}$ LAG, $\text{NA}=0.4$, $40\times$) determined with precise slits. The X-ray energy was $E=10.8 \text{ keV}$. The line profile represents the average of the slit image, depicted in the upper right corner of the figure.

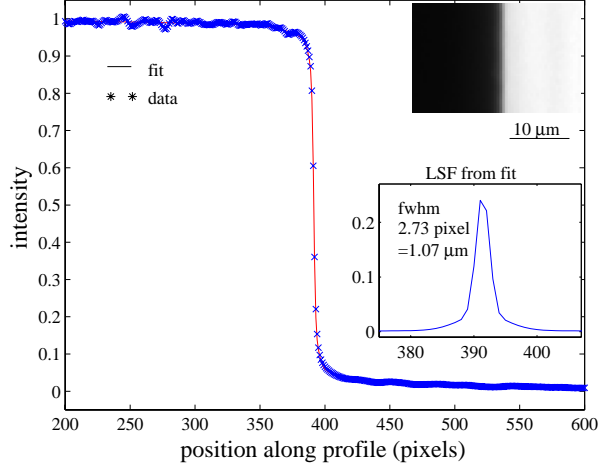


Figure 2.10: Edge spread function of the high-resolution set-up ($5 \mu\text{m}$ LAG, $\text{NA}=0.4$, $40\times$) determined from the image (upper right corner) of an absorbing knife edge (polished tungsten carbide blade). The line spread function is determined via derivation of the edge profile.

In order to suppress high frequency noise present in the experimentally determined profiles, we switched to the following analytical representations of the LSF and ESF [CLD⁺99]:

$$LSF(x) = \sum_{p=1}^j b_p \frac{1}{\sqrt{2\pi}a_p} \exp\left(-\frac{x^2}{2a_p^2}\right) \quad (2.35)$$

$$ESF(x) = c_1 + \sum_{p=1}^j \frac{b_p}{2} \left(1 + \text{erf}\left(\frac{x-x_0}{\sqrt{2}a_p}\right)\right) \quad (2.36)$$

$$(2.37)$$

Using a sum of four Gaussians ($j = 4$) and a linear least squares fitting procedure, a good agreement between the experimental and the analytical profiles can be obtained. The advantage of this method is obvious: once the coefficients a_p and b_p are determined, the remaining functions (MTF, PSF) can be expressed by simple analytic expressions, too:

$$MTF(\nu) = \sum_{p=1}^j b_p \exp(-2\pi^2 a_p^2 \nu^2) \quad (2.38)$$

$$PSF(x) = \sum_{p=1}^j b_p \frac{1}{2\pi a_p^2} \exp\left(-\frac{r^2}{2a_p^2}\right) \quad (2.39)$$

As can be seen from Fig. 2.11, the implementation of the new high-resolution set-up lead to a considerable enhancement of the imaging performance of our high-resolution detector system.

Table 2.4 summarizes the main characteristics of the currently employed high-resolution set-ups.

2.4 The mechanical setup

In the previous section we reported on the progress of X-ray micro-imaging in terms of spatial resolution. However, as desirable as each gain in spatial resolution r_d might be from the stand-

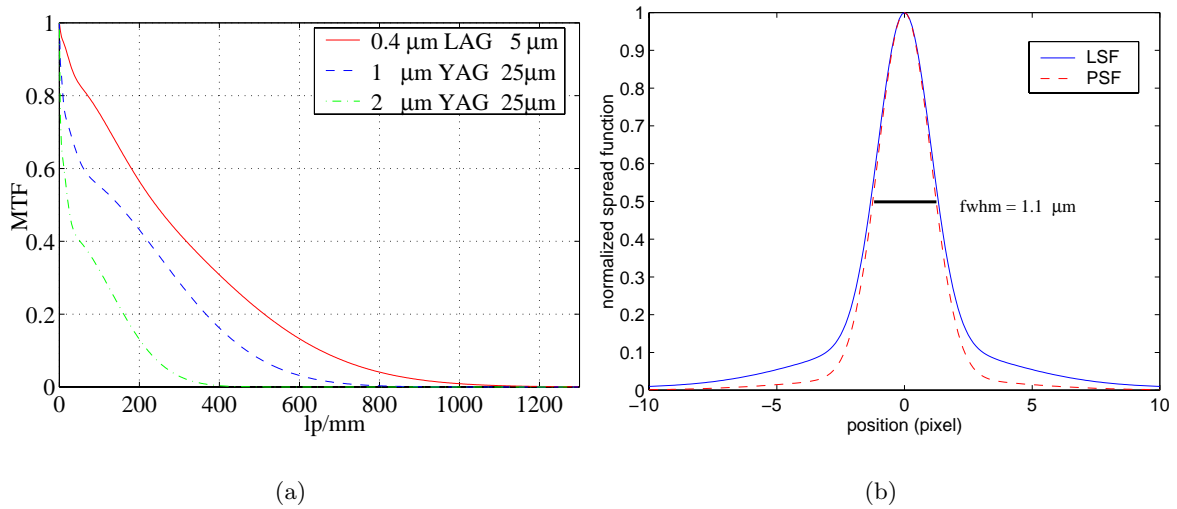


Figure 2.11: (a) Modulation transfer function for the different high resolution set-ups with 0.4, 1 and 2 μm effective pixel size. The new high-resolution set-up with LAG scintillator preserves 10% contrast for spatial frequencies up to 660 line pairs per millimeter. (b) LSF and PSF of the new high-resolution set-up (NA=0.4, 5 μm LAG, 40 \times).

set-up	QE	DQE	SNR	LSF (fwhm)	10% MTF
2 μm	0.14	0.07	410	3.1 μm	224 lp/mm
1 μm	0.14	0.07	410	2.0 μm	470 lp/mm
0.4 μm	0.11	0.05	410	1.1 μm	630 lp/mm

Table 2.4: Relevant characteristics for the different configurations of the high-resolution detector system.

point of imaging, it entails increased sensitivity with respect to unwanted artifacts arising from vibrations and the limited precision of the mechanical movements. This holds particularly true in the case of tomographic imaging, where the sample is turned around an axis: in order to preserve the spatial resolution provided by the detector system, the sample has to be positioned with an accuracy higher than the spatial resolution of 1 μm . The key elements of a tomographic set-up are therefore precise, sample rotation and translation units.

We implemented such a high precision tomographic sample stage on a set-up, which consists of two distinct blocs: a diffractometer serving as base unit for alignment of the sample stage and a separate translation table, which allowed us to change the distance between the sample and the detector system.

As the diffractometer is routinely used for other imaging experiments, this set-up has the drawback that it requires a time-consuming alignment procedure, each time the configuration is changed. In view of the increasing demand for tomographic imaging experiments we designed a new instrument, dedicated for this particular application. This new device combines the precision sample stage and the detector unit on the same base frame and provides additional degrees of freedom, required for the alignment procedure (see appendix A for details).

Chapter 3

Methods

In this chapter we will present our contribution to the development of new X-ray imaging methods: holotomography and topo-tomography.

Holotomography is based on the numerical reconstruction of the X-ray phase shift from a series of Fresnel diffraction patterns, recorded at different distances from the object. After an introduction to the basic concept of this technique we will demonstrate its application to the case of an Al/Si alloy. This example will also allow to compare holographic phase reconstruction to conventional absorption imaging and to phase sensitive imaging under weak defocus conditions.

Topo-tomography is the combination of X-ray diffraction imaging (topography) and tomographic reconstruction. Applied to perfect single crystals, this technique allows to analyse the three-dimensional arrangement of crystalline defects like dislocations and inclusions.

3.1 Holotomography

Our method of holographic phase reconstruction is based on an approach similar to the one of focus variation in high-resolution transmission electron microscopy [CJBD92, BDC96]. A detailed discussion of the adaption of this technique to the case of hard X-rays can be found in [Clo99].

After a short introduction to the principle of holographic phase reconstruction for the special case of a 'weak' phase object (§ 3.1.1) we will address the question, in how far the same approach may be also applied to the case of absorbing objects (§ 3.1.2). It turns out, that we may still obtain quantitative information about local variations of the phaseshift, provided the object has a smoothly varying absorption envelope. This new approach will then be demonstrated with the help of a practical example (§ 3.1.2).

3.1.1 Case of 'weak' phase objects

The principle of holographic phase reconstruction can be most easily understood in the case of a weak phase object $T(\mathbf{x}) = \exp i\varphi(\mathbf{x})$ and plane wave illumination of unit amplitude. In this case one may rewrite equation (1.27) in the form [Gui77]

$$\tilde{I}_D(\mathbf{f}) = \delta(\mathbf{f}) + 2 \sin(\pi\lambda D \mathbf{f}^2) \tilde{\varphi}(\mathbf{f}) + \tilde{I}_{NL}(\mathbf{f}) \quad (3.1)$$

valid for

$$|\varphi(\mathbf{x} + \lambda D \mathbf{f}) - \varphi(\mathbf{x})| \ll 1 \quad \forall \mathbf{x}. \quad (3.2)$$

Note that condition 3.2 is more general than strictly weak phase ($\varphi \ll 1$) and applies also to objects having a large phase 'envelope' $\varphi(\mathbf{x}) > 1$. Only the variation between points separated by $\lambda D \mathbf{f}$ has to be small compared to 1. Equation 3.1 states that the spectrum of the intensity is directly related to the spectrum of the phase. The contrast factor $2 \sin(\pi \lambda D \mathbf{f}^2)$ defines in how far the various frequencies \mathbf{f} , present in the spectrum of the phase, are transferred to the spectrum of the intensity. It turns out that the phase contrast factor is zero for frequencies fulfilling $\lambda D \mathbf{f}^2 = n$ ($n = 0, 1, 2, \dots$ integer).

One might think to recover the phase directly by applying the inverse filter $1/2 \sin(\pi \lambda D \mathbf{f}^2)$ to the spectrum of the recorded intensity distribution $\tilde{I}_D(\mathbf{f})$. This has however to be avoided, as the zeros in the contrast factor will lead to a strong amplification of the noise for frequencies, where the image contains no or little information about the phase. This problem may be circumvented by the summation of images taken in different distances D_m from the object.

Taking the sum of images at different distances, we will be interested in the solution $\tilde{\varphi}(\mathbf{f})$ which minimizes the difference between the observed ($\tilde{I}_m^{\text{exp}}(\mathbf{f})$) and the calculated intensity distributions $\tilde{I}_m\{\tilde{\varphi}(\mathbf{f})\}$ in a least squares sense. This leads to the following expression for the cost functional which has to be minimized with respect to the phase $\tilde{\varphi}(\mathbf{f})$

$$S_c = \frac{1}{N} \sum_m \int |\tilde{I}_m^{\text{exp}}(\mathbf{f}) - \tilde{I}_m\{\tilde{\varphi}(\mathbf{f})\}|^2 d\mathbf{f} \quad (3.3)$$

If the non-linear terms in expression 3.1 are negligible the derivation of 3.3 yields

$$\Delta'(\mathbf{f})\varphi(\mathbf{f}) = \frac{1}{N} \sum \Delta'_m(\mathbf{f})\tilde{I}_m^{\text{exp}}(\mathbf{f}) \quad (3.4)$$

with

$$\Delta'_m(\mathbf{f}) = \tilde{R}_m(\mathbf{f}) \sin(\pi \lambda D_m \mathbf{f}^2) \quad (3.5)$$

$$\Delta'(\mathbf{f}) = \frac{1}{N} \sum \tilde{R}_m^2(\mathbf{f}) 2 \sin^2(\pi \lambda D_m \mathbf{f}^2) \quad (3.6)$$

$$\tilde{R}_m(\mathbf{f}) = \tilde{R}(\mathbf{f}) \gamma^c(\lambda D_m \mathbf{f}) \quad (3.7)$$

Equation 3.4 is a first approximation to the solution of the inverse problem. The phase is obtained via linear filtering of the experimentally determined intensity distributions $\tilde{I}_m^{\text{exp}}(\mathbf{x})$ in Fourier space.

The determination of smooth variations in the object remains problematic with this differential phase method: the ideal filters $\Delta'_m(\mathbf{f})/\Delta'(\mathbf{f})$ can not be applied for the low frequencies. The inverse of the ideal filters is zero for $\mathbf{f} = 0$ and they grow initially with the square of the modulus of the spatial frequency. To some extend this problem can be solved by considering physically meaningful constraints (equ. 1.9) and applying an iterative non-linear least squares method for further optimization of the initial solution [CJBD92, Kir84, Clo99].

There is no conceptual difficulty to extend the outlined approach to a three-dimensional imaging technique: the reconstructed phase maps are projections of the refractive index decrement δ . Provided we acquire a large set of such projections for different angular settings of the object, we can apply the standard tomographic reconstruction procedure to reconstruct the 3D distribution of the refractive index decrement. In practice this procedure involves the acquisition of tomographic scans at several distances D from the object (Fig. 3.1). The reconstruction is then carried out in two steps:

1. Phase retrieval. The images for a given angular setting are carefully aligned by cross-correlation techniques and the phase shift is determined by applying the filters (equ. 3.4). This procedure is repeated for all angular settings of the object.
2. Tomographic reconstruction. The phase maps are the required input for the quantitative reconstruction of the 3D refractive index distribution.

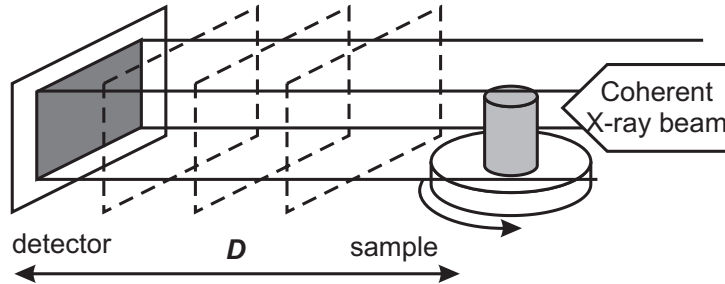


Figure 3.1: Principle of holotomography: for each distance D a complete tomographic scan (N images over 180°) is recorded. The reconstruction is divided into two steps: (i) Holographic reconstruction of the X-ray phase shift from images in different distances (this procedure is repeated for all angular settings) and (ii) Tomographic reconstruction of the refractive index from the phase maps, determined in the first step.

We have demonstrated the applicability of this approach for the case of a weak phase object (polystyrene foam), where it was possible to determine the overall phase shift ($\cong 7$ rad), introduced by the object [CLB⁺99]. We will now address the question in how far this approach may also be extended to the case of strong absorbing objects, provided condition 3.2 is still fulfilled.

3.1.2 Approximate solution for the case of an absorbing object

Although equation 3.1 is strictly only valid in the case of a pure phase object, we may still obtain an approximate solution, if we use the same approach for an absorbing object. It can be shown (see Appendix B) that this approach is based on the assumption, that the absorption term $A(\mathbf{x})$ does not vary significantly over distances $\lambda D f_{\max}$, where f_{\max} is the maximum frequency of the band-limited spectrum of the object phase $\tilde{\varphi}(\mathbf{f})$.

This condition is for instance ideally fulfilled in the case of a plan-parallel plate of a heterogeneous material, where the different constituents give only rise to a weak modulation of the absorption, whereas the modulation of the X-ray path length is comparable to the X-ray wavelength (i.e. $\varphi \approx 2\pi$). In this (ideal) case the holographic phase reconstruction would allow to determine the local differences in the phase shift with respect to the mean phase shift of the object.

The condition of a smoothly varying absorption profile is still reasonably fulfilled if we consider the case of an object of cylindrical shape, imaged perpendicular to the cylinder axis. In this case, which is of special interest for tomographic imaging, the phase shift may be decomposed into two components: (i) a large, smooth envelope due to the cylindrical shape of the object and (ii) small variations due local variations in the refraction index. There will be a large difference in the phase shift between points located at different distances with respect to the cylinder axis (1 mm of Al at 12.4 keV corresponds to a phase shift of $\Delta\varphi \approx 100\pi$). Due to the vanishing contrast

factor for low spatial frequencies, the holographic reconstruction will not allow to reconstruct the large envelope of the phase profile perpendicular to the cylinder axis.

It turns out, that we may nevertheless obtain quantitative information about the relative phase changes inside the object if we apply the holographic phase reconstruction to images from which we have removed the strong intensity modulation caused by the absorption.

The above mentioned elimination of the absorption profile in the defocussed images ($D > 0$) is achieved by the division with the absorption image ($D = 0$). These modified images are then used as input for the holographic reconstruction, still based on equation 3.1, in which we replace the Fourier transform of the defocussed images \tilde{I}_D by the Fourier transform of the normalized images

$$\tilde{I}_D(\mathbf{f}) = \mathcal{F}\{I_D(\mathbf{x})\} \leftrightarrow \mathcal{F}\left\{\frac{I_D(\mathbf{x})}{I_0(\mathbf{x})}\right\} \quad (3.8)$$

The modified version of equation 3.1 reads now

$$\mathcal{F}\left\{\frac{I_D(\mathbf{x})}{I_0(\mathbf{x})}\right\} \approx \delta(\mathbf{f}) + \tilde{\varphi}(\mathbf{f}) \sin(\pi\lambda D \mathbf{f}^2) \quad (3.9)$$

and summation over several distances yields (cf. equ. 3.4)

$$\Delta'(\mathbf{f})\tilde{\varphi}(\mathbf{f}) = \frac{1}{N} \sum \Delta'_m(\mathbf{f})\mathcal{F}\left\{\frac{I_m(\mathbf{x})}{I_0(\mathbf{x})}\right\} \quad (3.10)$$

where $\Delta'_m(\mathbf{f})$ and $\Delta(\mathbf{f})$ are the ideal filter functions, which have already been defined in the case of the weak phase object (equ. 3.5 and 3.6).

The normalization of the defocussed images by the absorption image might be considered as a high-pass filter. From equ. 3.9 it is clear that this operation will also suppress the low frequency modulation of the reconstructed phase shift and that we will only retain the information about relative variations of $\varphi(\mathbf{x})$ which are contained in the high frequency part of the spectrum. Tomographic reconstruction from a set of such phase maps will consequently not yield the absolute value of the refractive index distribution (for this the overall phase envelope has to be known) but the relative variation of the refractive index with respect to its mean value in the surrounding matrix.

It can be shown that the outlined approach (division by the absorption image) is based on the introduction of two approximations in the general formulation of the imaging process (see Appendix B). As will be shown in the next section this approach provides excellent results and has been adopted as a working solution.

Depending on the values of cylinder radius, the mean refractive index decrement, the detector resolution and the distance between the object and the image plane, it may be necessary to introduce an additional correction for an effect which we have neglected so far in our discussion: the large, spatially varying phase shift, imposed by the geometry of the cylinder will lead to an angular deviation of the propagation direction of the transmitted radiation ($\Delta\alpha \sim \nabla\varphi$). Images at different distances behind the object will consequently suffer from different degrees of deformation in the direction perpendicular to the cylinder axis.

As a first approximation, the effect of a cylindrical object may be considered equivalent to the one of a divergent, one-dimensional lens with focal length

$$f = \frac{R}{2\delta} \quad (3.11)$$

where R denotes the radius of curvature of the (parabolic) lens profile.¹ In this case the deformation may be described by a simple magnification which depends on the propagation distance. One can consequently account for this effect by applying the inverse magnification prior to the holographic reconstruction.

3.1.3 Experimental results

In order to demonstrate the different variants of tomographic imaging (absorption contrast, phase sensitive imaging in the edge-detection regime and holotomography) we have chosen the example of an aluminium alloy, containing small (1-5 μm) Si inclusions. The characterization of this material is challenging and will allow to demonstrate the current state-of-the-art in hard X-ray micro-imaging in terms of spatial resolution and sensitivity:

- The X-ray attenuation coefficients of Al and Si are very close to each other. At the chosen X-ray energy of 10.7 keV we expect only poor absorption contrast, the 1 % thickness of Si being 1.6 μm . Phase contrast will be a prerequisite to detect these inclusions.
- The size of the smaller Si inclusions is close to the resolution limit of our experimental set-up. We used the new high-resolution set-up (0.4 μm pixelsize) with 5 μm LAG converter screen. Tomographic imaging at this resolution is currently only possible with the use of the high bandwidth multilayer monochromator in order to limit the overall acquisition time for a single scan to a few tens of minutes (compared to almost a day with the Si double crystal monochromator).

A cylindrical sample of 300 μm diameter was prepared from a piece of cast Al alloy AS03G7 (composition in at. %: Si (7.0), Fe (0.1) Mg (0.3), Ti (0.12), Sb (0.13), Cr (0.2)). Four tomographic scans (900 projections each) were then recorded at distances $D = 5, 20, 55$ and 305 mm from the object.

Figure 3.2 shows projections of the same part of the sample, recorded at the different distances. The images are displayed with identical contrast (proportional to the local transmission). The transmission in the center of the absorption image (Fig. 3.2a) is in the order of 15 % and reveals the presence of isolated absorbing inclusions.² The absorption images provides no indication for the presence of the micrometer sized Si particles. Increasing the sample to detector distance, the contours of the absorbing inclusions are outlined by black-white contrasts of increasing amplitude (Fig. 3.2b,c) and the formerly uniform image background has become a granular character. This granularity, best seen at $D = 55$ mm indicates now the presence of the small, micrometer sized inclusions. Finally, at $D = 300$ mm (Fig. 3.2d) one can observe the transition of the formerly isolated black-white contrasts into a more complicated interference pattern.

Figure 3.3 shows the result of the holographic phase reconstruction (§ 3.1.2), based on the defocus series in Fig. 3.2. The images at $D = 20, 55$ and 305 mm distance were corrected for the changing magnification and divided by the image recorded at $D = 5$ mm, which served as approximation for the absorption image.³ Before application of the holographic reconstruction procedure, the normalized images were carefully aligned, using cross-correlation techniques.

¹Note that this principle was recently used to build the first refractive lenses for hard X-rays, where a series of cylindrical holes act as focusing elements [SKSL96].

²SEM and EDS analysis revealed the presence of two different types: AlSiFe intermetallics of elongated shape and rather spherical inclusions containing mainly Sb and Mg [Sav00].

³The current mechanical set-up does not allow to reduce the sample to detector distance below this value.

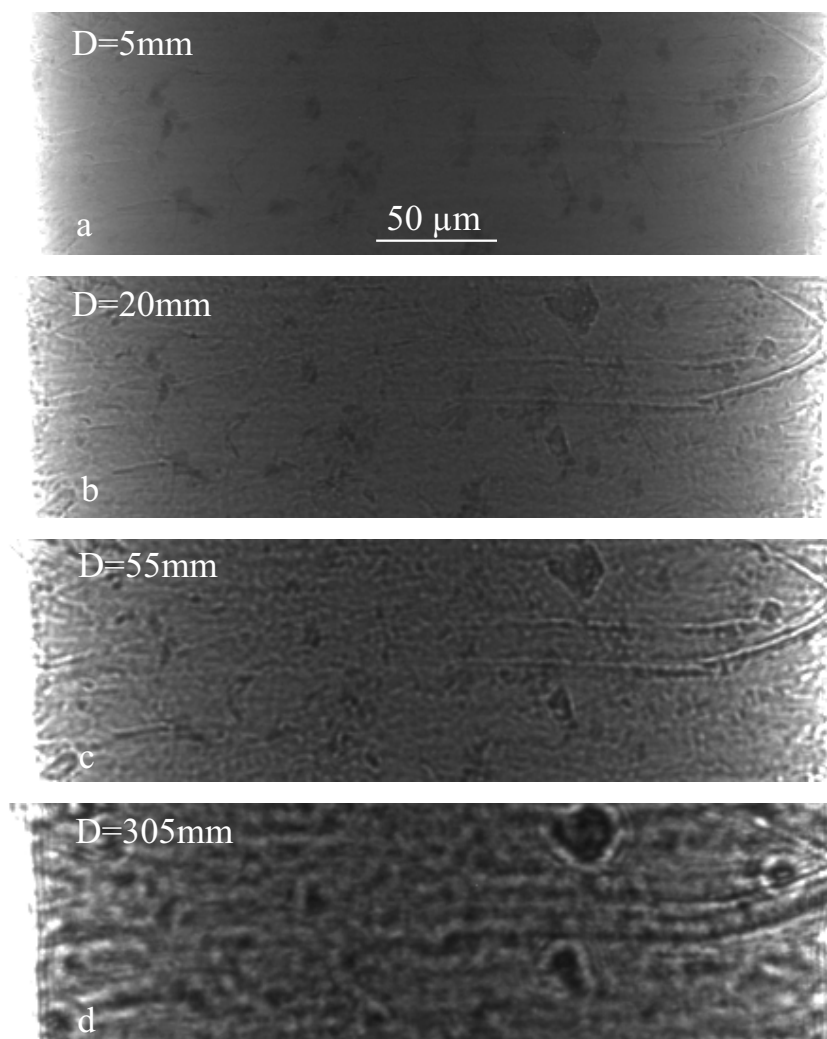


Figure 3.2: Defocus series of a cylindrical sample of cast Al alloy containing small ($1\text{-}5\ \mu\text{m}$ Si and somewhat larger ($5\text{-}20\ \mu\text{m}$) Fe rich inclusions (dark contrasts). The images were recorded at distances $D = 5, 20, 55$ and 305 mm from the sample. Whereas the Si particles cannot be detected in the absorption image, they give rise to a granular contrast, best seen in the image at 55 mm distance. The curved line-shaped contrast at the right border is due to a strong surface corrugation at this position.

This last step is of crucial importance and reveals the current limitations of the multilayer monochromator: the surface slope errors introduce a slight distortion of the image in the vertical direction. As we have to align the images with an accuracy better than the pixel size ($0.4\ \mu\text{m}$) this distortion poses a problem for the simultaneous alignment of particles, at different vertical positions in the image. The restriction of the vertical image size to $100\ \mu\text{m}$ has proven a workable solution to limit the alignment problems.

Note that the phase reconstruction reveals clearly the presence of small (few μm) white contrasts. Higher gray values correspond to a positive phase shift compared to the surrounding Al matrix. At the energy used for our experiment ($10.7\ \text{keV}$), the refractive index decrement of Si is slightly smaller compared to the one of Al ($\delta_{\text{Si}} = 4.27 \cdot 10^{-6}$, $\delta_{\text{Al}} = 4.77 \cdot 10^{-6}$) and one expects indeed a positive value for the Si particles compared to the Al matrix. The remaining

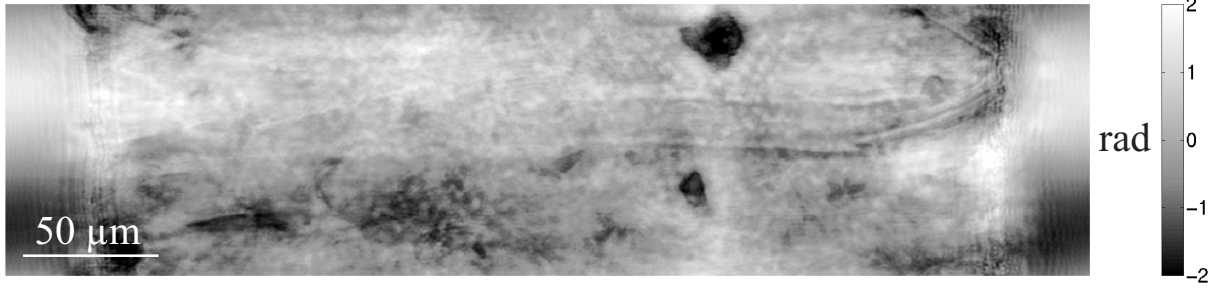


Figure 3.3: Result of the holographic phase reconstruction based on the defocus series in Fig. 3.2. The gray values in the image correspond to the relative phase shift $\varphi(\mathbf{x})$ with respect to the surrounding Al matrix. Note that the micrometer sized Si particles are now clearly discernible as isolated white contrasts (lower electron density).

non-uniformity of the image background is comprised in the interval $[-2...2 \text{ rad}]$ and may be attributed to: (i) the approximate solution for the correction of the image distortion and (ii) the approximation introduced by the normalization of the defocussed images.

The phase reconstruction was repeated for the 900 angular positions of the object in order to obtain the necessary input for the tomographic reconstruction. The computing time for a single phase map was in the order 30 s (650 Mhz, dual processor).

Figure 3.4a shows the result of the tomographic reconstruction based on the reconstructed phase maps (holotomography). The image contrast is proportional to differences of the refractive index with respect to its mean value in the surrounding Al matrix. The Si particles are detected with excellent contrast. One observes further the two different types of inclusions which have been characterized in electron microscopy: elongated, plate like particles (of type AlSiFe) and spherical clusters containing mainly Sb and Mg [Sav00]. Due to the fact that the tomographic reconstruction is based on a large number of projections, the background non-uniformity, observed in the individual phase-maps has been averaged out completely. The values of the reconstructed refractive index difference between the Si particles and the Al matrix $\Delta\delta$ are slightly below the expected value of $\Delta\delta \cong 5 \cdot 10^{-7}$. Part of this difference may be attributed to the partial volume effect [KS88]: the size of the reconstructed objects is small compared to sampling volume and voxels (volume elements) on the border of the Si particles will receive the average value, determined by the volume fraction occupied by the different materials.

Note that the contrast in the 'absorption' image ($D = 5 \text{ mm}$) is already influenced by phase contrast: one would expect a slightly higher attenuation of the Si particles compared to the Al matrix ($\mu_{\text{Al}} = 54.5 \text{ cm}^{-1}$; $\mu_{\text{Si}} = 61.0 \text{ cm}^{-1}$ at $E=10.7 \text{ keV}$). Edge enhancement (cf. § 1.4.2) leads already to contrast inversion in the small Si particles, which appear slightly darker compared to the Al matrix. The value of the absorption coefficient in the Al matrix corresponds well to the expected value of $\mu_{\text{Al}} \cong 54.5 \text{ cm}^{-1}$.

Figure 3.5 shows two volume renderings of the microstructure of the investigated material. Due to the excellent contrast in the (holo) tomographic reconstruction, a simple threshold algorithm can be used to visualize only the Si particles (i.e. all voxels below a certain threshold are set to transparent). Note that the segmentation would not have been possible in absorption mode because of insufficient contrast.

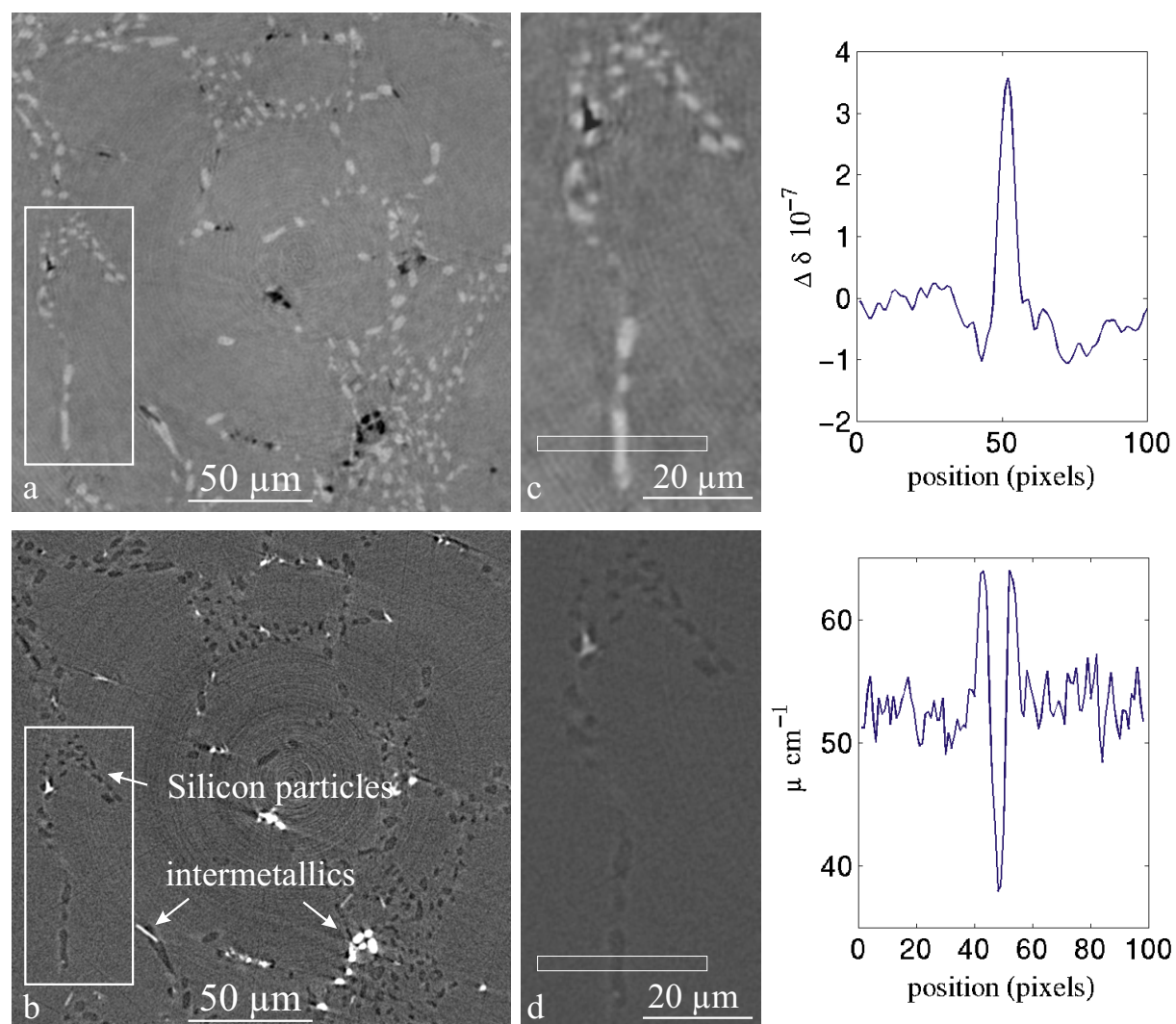


Figure 3.4: Comparison of (a) holotomography and (b) absorption tomography. The contrast in the holographic reconstruction is proportional to the local difference of the refractive index decrement δ with respect to its mean value in the Al matrix. Silicon particles down to a few pixels in size ($1\text{-}2\ \mu\text{m}$) are still detected with excellent contrast and resolution. Due to the finite recording distance ($D = 5\ \text{mm}$), the contrast of the Si particles in the 'absorption' scan (b) is already governed by phase effects. The plots on the right side correspond to the profiles indicated in the zoomed images (c) and (d)

Edge enhancement

If we do not require the information about the quantitative values of the refractive index decrement, it will be interesting to use the simpler, direct variant of phase sensitive tomography (§ 1.4.2). As already observed in the case of the single projections (Fig. 3.2, discontinuities of the refractive index decrement lead to the formation of black-white contrasts. The amplitude of this contrast increases with the propagation distance. We may consequently improve the visibility of sample inhomogeneities in the tomographic reconstruction by taking advantage of this contrast mechanism (edge enhancement). Figure 3.6 illustrates this mode in the case of our Al alloy.

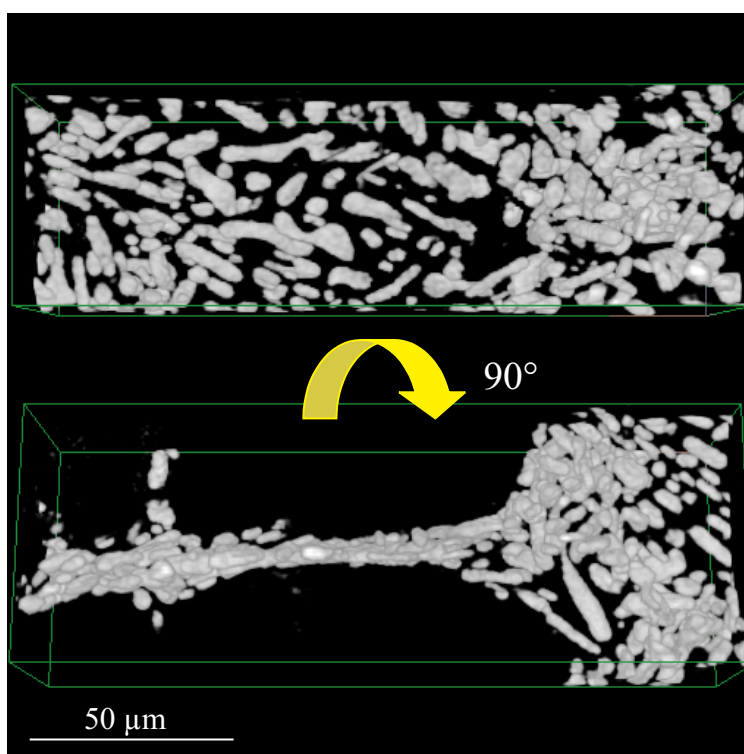


Figure 3.5: Volume rendering of the microstructure of the Al alloy. The image was obtained by setting all voxels below a certain intensity threshold to transparent and reveals the preferential location of the Si particles on boundaries (the Si particles are formed during the solidification of the eutectic phase between the dendrites of the primary Al).

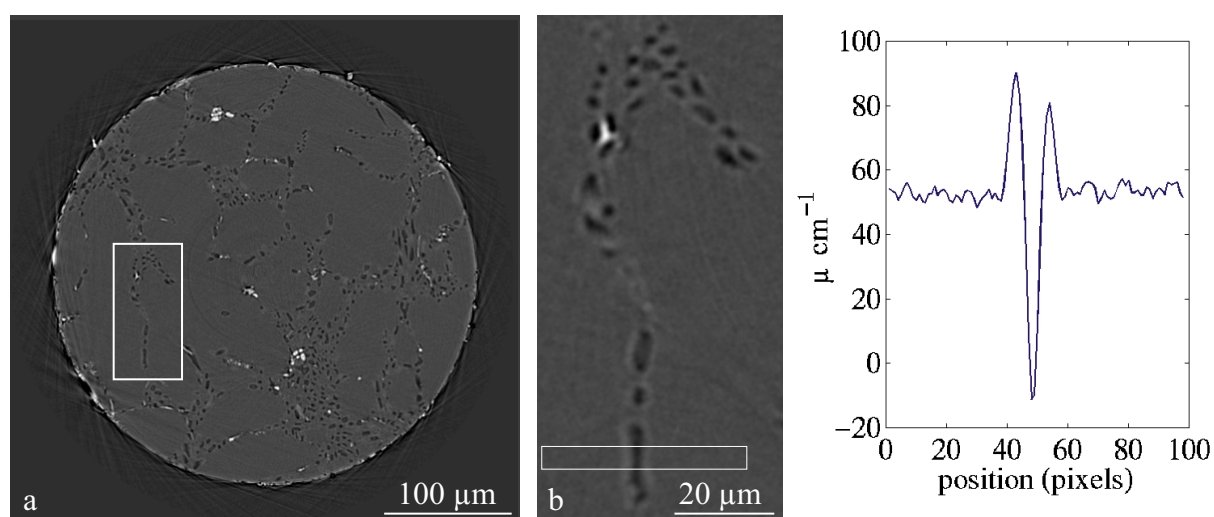


Figure 3.6: Result of tomographic reconstruction in the edge-detection regime (phase-contrast tomography). The image contrast is governed by the 'edge enhancement' at the singularities of the refractive index distribution in the material (i.e. interfaces between the Si particles and the Al matrix).

3.1.4 Conclusion

We have demonstrated the extension of holographic phase reconstruction to the case of absorbing objects with smoothly varying absorption profile. The holographic reconstruction is based on the numerical processing of a series of defocussed images and provides quantitative information about local variations of the phase shift with respect to the mean value in the surrounding matrix. Tomographic reconstruction based on a large number of such phase maps yields quantitative information about local variations of the refractive index decrement $\delta(\mathbf{r})$ with respect to its mean value in the material. The holographic reconstruction provides excellent spatial resolution and enhanced sensitivity compared to conventional absorption imaging.

If one is only interested in the detection of sample inhomogeneities (e.g. 3D distribution of inclusions, detection of cracks,...) the simpler variant of phase-sensitive tomography (i.e. a single tomographic scan under weak defocus conditions) may already provide sufficient information.

3.2 Topo-Tomography

3.2.1 Motivation

So far we considered tomographic imaging for the case of amorphous or polycrystalline materials and we neglected deviations from the ideal transmission behaviour due to diffraction effects. We now address the question, in how far we may extend tomographic imaging to the case of rather perfect single crystals, taking advantage of Bragg diffraction as a contrast mechanism. The latter technique, known as X-ray diffraction imaging or X-ray topography [Tan76], is widely employed for the characterization of high quality crystalline materials.

Conventional X-ray diffraction imaging allows to visualize long range strain fields induced e.g. by crystalline defects like inclusions or individual dislocations. Due to the fact that the three-dimensional arrangement of the defects is projected on a two-dimensional image ('topograph'), this technique does not easily allow to determine the exact position of the defects within the bulk of the crystal. The knowledge of the three-dimensional defect structure is however important, for instance, if a "good quality" sample has to be cut out from a bulky crystal. This has been achieved in the past either by performing "stereo-pair" diffraction topographs [Lan80] (which provide two views of the defects, angularly separated by twice the Bragg angle, $2\theta_B$) and, more recently, by carrying out a number of closely spaced 'section' topographs [MROM97, OST⁺00]. These methods are experimentally easy to implement but provide only more or less good approximations to a true three-dimensional visualization of the defects.

We propose a new approach to perform a three-dimensional characterization of crystalline defects in the bulk of rather perfect single crystals. The basic idea is to combine tomographic and topographic imaging. The tomographic reconstruction yields a three-dimensional map of the local Bragg reflectivity inside the crystal. A description of the principle of 'topo-tomography', together with a short discussion of the experimental conditions which have to be fulfilled will be given in the next section. We then present the experimental set-up and discuss first results obtained from a synthetic diamond crystal.

3.2.2 The principle

Crystalline defects like inclusions and dislocations give rise to variations in the local Bragg reflectivity $R_g(\mathbf{r})$ in the crystal. The spatial distribution and the geometry of such defects can consequently be determined from the knowledge of the three-dimensional distribution of the local reflectivity in the bulk of a crystal. As we have seen in § 1.5, it is possible to reconstruct the three-dimensional distribution of an unknown object function from knowledge of its 2D Radon-transform, i.e. from a set of two-dimensional projections.

Provided a number of conditions are fulfilled, a special kind of contrast in X-ray diffraction topographs (so-called *direct image*, [Tan76]) may be proportional to projections of the Bragg reflectivity $R_g(\mathbf{r})$ along the diffracted beam (wavevector \mathbf{k}_h). In this case the diffracted intensity may be decomposed into contributions arising from (i) the perfect crystal matrix (constant, homogeneous diffraction background) and (ii) the lattice distortion around crystal defects. The necessary conditions to observe *additional* intensity along the direction of the diffracted beam, the direct image, may be formulated in the following way:

1. The incoming beam must be divergent and/or non-monochromatic with respect to the

width of the perfect crystal reflection curve (integrated wave topography)

$$\alpha \gg w_g^\theta \quad (\alpha = \text{angular source size}) \quad (3.12)$$

$$\Delta\lambda \gg w_g^\lambda \quad (3.13)$$

where w_g^θ and w_g^λ denote the width of the reflection curve, defined in angular and in wavelength space respectively:

$$w_g^\theta = \frac{\lambda}{\Lambda_g \sin \theta_B} \quad (3.14)$$

(symmetrical Laue case)

$$w_g^\lambda = w_g^\theta \lambda \cot \theta_B \quad (3.15)$$

The parameter Λ_g is called the 'Pendellösung' length

$$\Lambda_g = \frac{\pi V_c \cos \theta_B}{r_e \lambda C (F_g F_{\bar{g}})^{\frac{1}{2}}} \quad (\text{symmetrical Laue case}) \quad (3.16)$$

where V_c denotes the volume of the unit cell, C the polarization factor, F_g the structure factor and r_e the classical electron radius.

2. The effective misorientation $\delta\theta(\mathbf{r})$, the parameter describing the deformation of the crystal lattice around the defects, must be large compared to the width of the perfect crystal reflection curve

$$\delta\theta(\mathbf{r}) \gg w_g^\theta \quad (3.17)$$

The effective misorientation is defined as

$$\delta\theta(\mathbf{r}) = \frac{1}{g \cos \theta_B} \frac{\partial}{\partial \mathbf{s}_g} [\mathbf{g} \cdot \mathbf{u}(\mathbf{r})] \quad (3.18)$$

where \mathbf{s}_g is the unit vector in direction of the diffracted beam and $\mathbf{u}(\mathbf{r})$ is the lattice deformation field.

3. The (individual) deformed parts of the crystal are small compared to the Pendellösung length Λ_g
4. The absorption in the crystal must be small $\mu t \leq 1$ (t = thickness of the crystal)
5. The crystal is thick enough to diffract dynamically ($t \geq \Lambda_g$)

The origin of the direct image may be understood from the behaviour of the integrated reflectivity as a function of the crystal thickness (see Fig. 3.7). The small deformed regions diffract components of the incoming beam which do not participate to the diffraction by the perfect matrix (i.e. the intensity is proportional to the extent Δ of these regions) whereas the integrated intensity of the crystal matrix is nearly constant over the lengthscale of Δ .

Provided the above conditions are fulfilled, the local reflectivity may be considered as the sum of (i) an (almost) constant background signal from the perfect crystal matrix R_0^{perf} and (ii) the additional signal due to the presence of defects $R_g^{\text{def}}(\mathbf{r})$

$$R_g(\mathbf{r}) \cong R_0^{\text{perf}} + R_g^{\text{def}}(\mathbf{r}) \quad (3.19)$$

The intensity on the detector (projection of the reflectivity along the direction of the diffracted beam \mathbf{k}_g) may therefore be decomposed into an (almost) constant background signal from the perfect crystal matrix and an additive contribution proportional to the projection of the locally enhanced reflectivity due to the presence of defects $\int R_g^{\text{def}}(\mathbf{r}) d\mathbf{k}_g$.

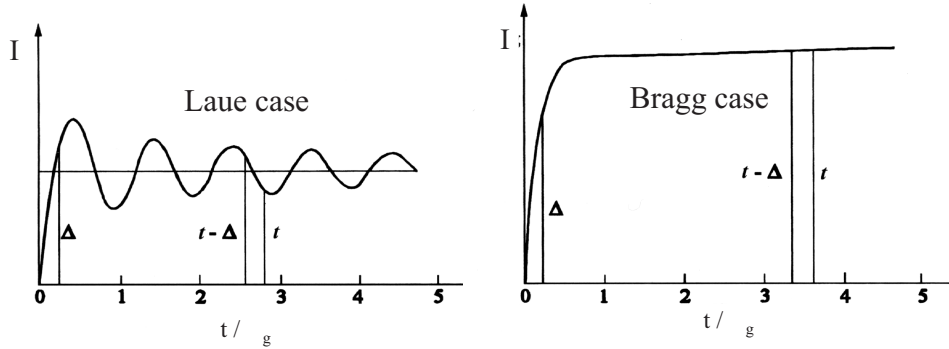


Figure 3.7: Integrated intensity in the Laue and in the Bragg case. A deformed region of size Δ causes only a small change in the integrated reflectivity of a bulk crystal $\delta I = I(t) - I(t - \Delta)$. The deformed region diffracts slightly different wavelengths and contributes the additional intensity $I(\Delta) > \delta I$.

3.2.3 The experimental set-up

Figure 3.8 shows a scheme of the experimental set-up used for 'topo-tomography'. The sample, a few millimeters in size, is illuminated with a large ($7 \times 7 \text{ mm}^2$), monochromatic (40 keV) beam, as delivered by the double crystal Si 111 monochromator (§ 2.2.1). An adapted configuration of the high-resolution detector system with $6.65 \mu\text{m}$ effective pixel size and a powder phosphor as converter screen was used for this experiment. Compared to conventional tomography, 'topo-tomography' requires two additional degrees of freedom (tilt 3&4) in order to align the sample with respect to the rotation axis. The sample is set for Bragg diffraction (transmission case) associated with the reciprocal lattice vector \mathbf{g} and it is mounted such way that it can be rotated around \mathbf{g} by means of the rotation stage. Consequently, the rotation axis \mathbf{a} and the diffraction vector \mathbf{g} have to be carefully aligned (better than 0.001°) with help of the crossed tilts 3 & 4 by an iterative procedure until the sample stays approximately in diffraction over a full turn around the axis \mathbf{a} . During tomographic acquisition, the crystal will be turned stepwise around the rotation axis \mathbf{a} (angle ω).

Due to the dispersive set-up, only part of the sample will be illuminated for a given angular setting. Therefore, an additional scan (tilt 2) over the width of the rocking curve has to be performed for each position ω , while the diffracted intensity is integrated on the detector (integrated projection topograph).

Note that this set-up differs from the standard acquisition geometry in one important respect: the rotation axis is not perpendicular to the incoming beam like in the parallel beam case, but *inclined* by the angle $\pi/2 - \theta_B$ and the diffracted intensity is projected along the direction \mathbf{k}_h . This somewhat particular geometry corresponds to an extreme case of the *cone-beam* acquisition geometry used in conventional CT (see Fig. 3.9): it is as if the sample was set far off-axis with respect to the cone. Due to the large distance from the source the cone angle is practically constant over the dimensions of the sample (parallel beam) and equals θ_B . As the individual lines in the 2D projections are no longer independent, the tomographic reconstruction requires a somewhat more complex reconstruction algorithm for the cone beam case [FDK84].

We recorded 500 integrated projection topographs of a synthetic diamond crystal ($4 \times 4 \times 1.5 \text{ mm}$). The crystal was set for the 220 reflection and an energy of 40 keV ($\mu t = 0.08$ t = thickness of the crystal) was chosen. The corresponding Bragg angle was $\theta_B = 7.1^\circ$. The images were recorded on a high-resolution detector system based on a $5 \mu\text{m}$ thick Gadox powder phosphor,

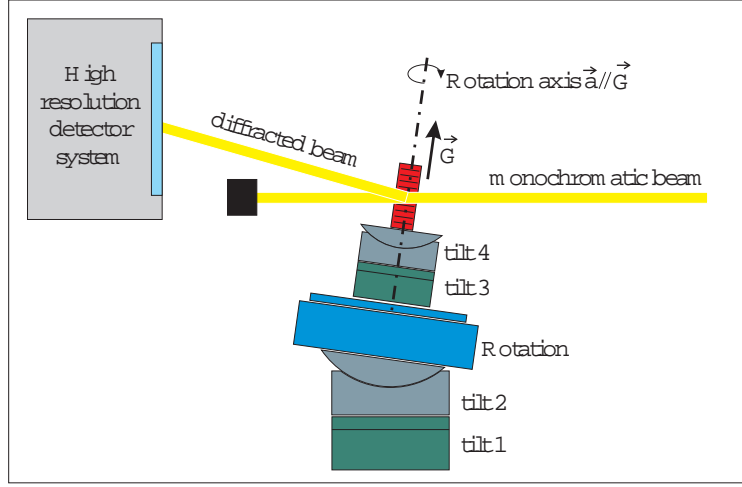


Figure 3.8: Experimental set-up used for topo-tomographic data acquisition. During the tomographic scan, the crystal is turned around the rotation axis \mathbf{a} (angle ω). The projection of the axis \mathbf{a} on the detector screen is aligned parallel to the columns of the detector (tilt1). The rotation axis is inclined by $\pi/2 - \theta_B$ with respect to the incoming monochromatic beam (tilt2). The crystal has to be aligned such that \mathbf{g} is parallel to \mathbf{a} (tilt 3 & 4). At each angular position ω , the crystal is scanned through the rocking curve (tilt2) and an integrated topograph is recorded on the CCD detector system.

light optics and a CCD camera (ESRF Frelon camera [LSBM96]). The effective pixel size was $6.6 \mu\text{m}$ and typical exposure times for an integrated topograph were in the order of 15 seconds. During each exposure, the crystal was continuously scanned over a small interval ($\theta_b \pm 0.001^\circ$).

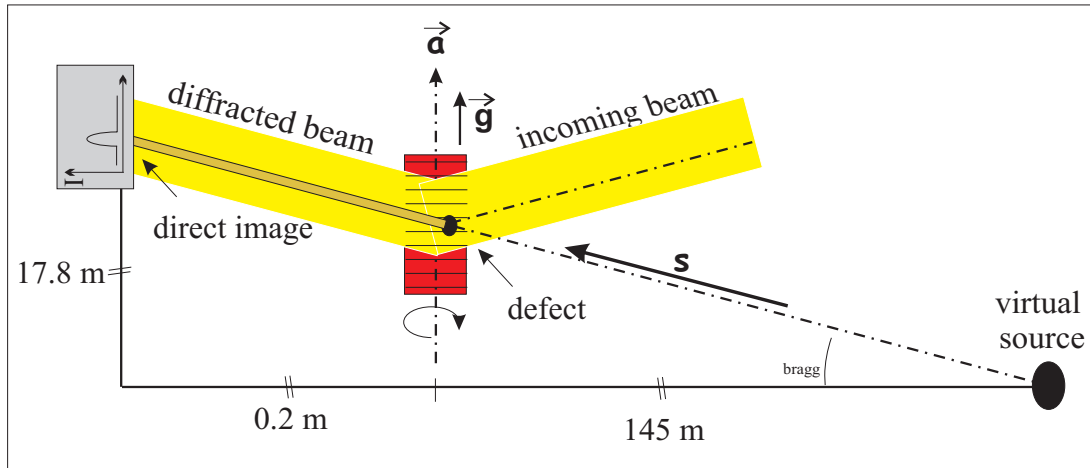


Figure 3.9: The acquisition geometry corresponds formally to an off-axis cone beam set-up with azimuth angle $\Psi = \theta_B$ in conventional CT. The intensity on the detector corresponds to projections of the local Bragg reflectivity along rays from the virtual source point.

3.2.4 Results

The recorded topographs were corrected for a constant background (additive dark current of the CCD) and subject to an approximate flat field correction to account for inhomogeneous

illumination (incoming beam) and non-uniformities in the pixel response (local variations of the gain of the scintillator and CCD chip). These non-linearities must be taken into account in order to avoid severe degradation of the reconstructed images. Note that it is *not* possible to apply the usual flatfield correction like in transmission mode (division by an image of the incoming beam without sample). We used an approximate correction obtained by taking for each pixel an average over the 500 projections. Due to the rotation of the sample, the contrast of individual dislocations is averaged out and one obtains a sufficiently uniform image. Provided a perfect, dislocation free diamond single crystal was available, an alternative solution would consist in recording a flatfield with the help of such a crystal.

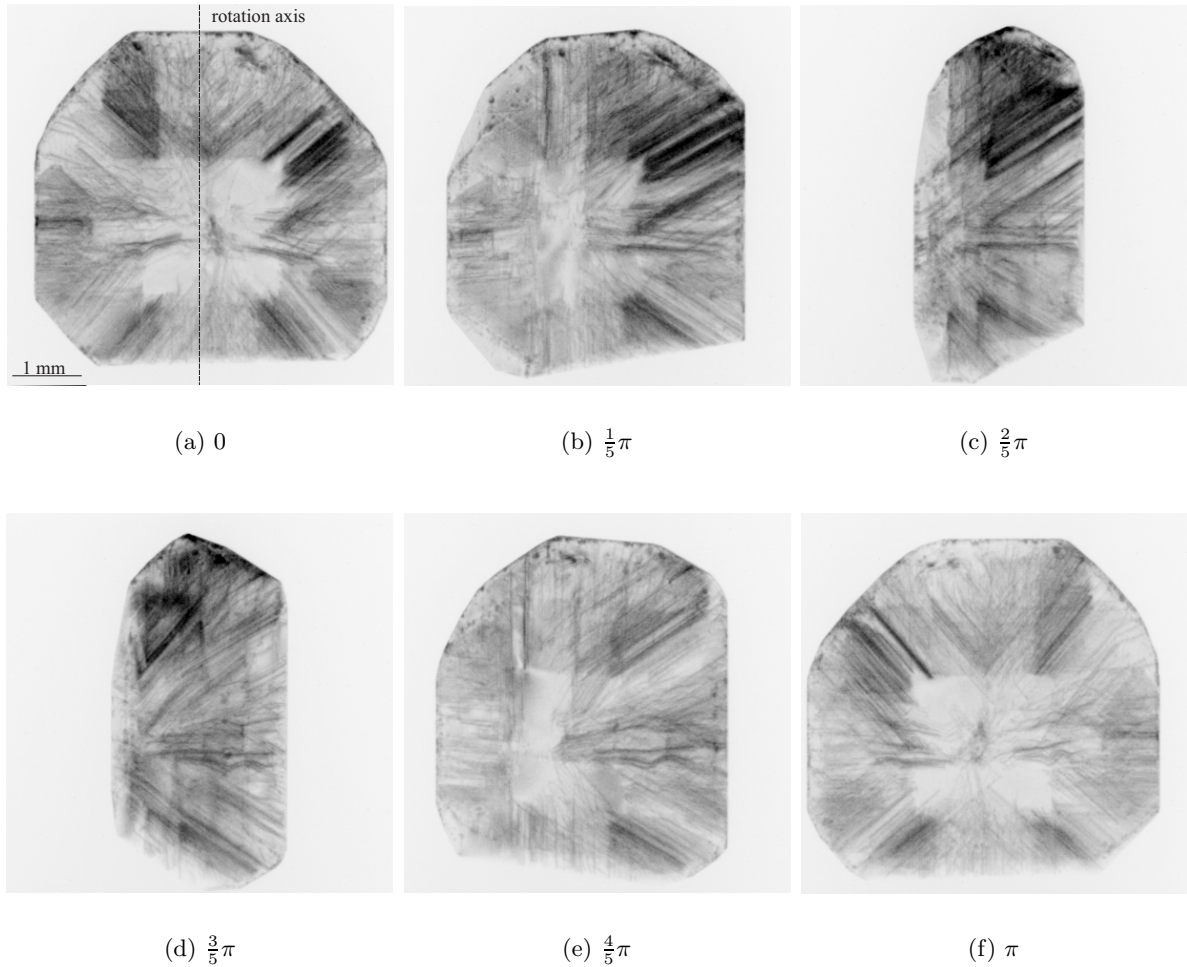


Figure 3.10: Monochromatic beam diffraction topographs (40 keV, $g = 220$ of synthetic diamond for different angular settings ω . At each position ω the rocking curve is scanned and integrated on the two-dimensional high-resolution detector system.

Figure 3.10 shows 6 (out of 500) integrated diffraction topographs for different angular settings ω with respect to the vertical rotation axis. Black contrast corresponds to higher projected X-ray reflectivity (usual topography convention). Note, that the images at 0° and 180° are not exactly mirror images as the axis is inclined by $\pi/2 - \theta_B$ with respect to the direction of the diffracted beam. This is taken into account by choosing appropriate geometrical input parameters for the cone beam reconstruction algorithm. The diffracted beam can be considered as a ray emerging

from a virtual source, located upstream of the sample and inclined by θ_B with respect to the rotation plane. We have chosen the source to sample distance equal to the real one on beamline ID19 (145 m). In this case the distance with respect to the axis has to be set to ($\Delta z = 17.8$ m) in order to make the azimuthal angle equal to θ_B . It is clear that this angle is practically constant over the vertical extent of the sample (4 mm).

Figure 3.11a shows a reconstruction of the local Bragg reflectivity $R_{\mathbf{g}}(\mathbf{r})$ perpendicular to the rotation axis. The position of this slice is indicated by the dashed line in Fig. 3.11c. White corresponds to higher reflectivity. The image reveals the outline of the trapezoidal crystal, as well as point like contrasts of different size and intensity. Setting all pixels below a certain intensity threshold to transparent, the reconstructed volume data were visualized with a commercial volume rendering software package. A volume rendition of the upper part of the crystal is shown in Fig.3.11b. This image reveals the presence of line shaped contrasts, traversing the crystal in preferential directions.

3.2.5 Discussion

In the discussion of the principle (§ 3.2.2) we stated, that we may apply the tomographic reconstruction, provided the images correspond to projections of the local reflectivity. We further defined the experimental conditions, under which the recorded intensity may be considered as a projection of the reflectivity $R_{\mathbf{g}}^{\text{def}}(\mathbf{r})$ (direct image). Concerning the case of the diamond crystal diffracting at 40 keV, it can be shown, that these conditions were fulfilled: the relative bandwidth of the radiation ($\Delta\lambda/\lambda \cong 10^{-4}$) delivered by the Si(111) double crystal monochromator is large compared to the intrinsic width of the chosen reflection ($\mathbf{g}=220$) in the diamond crystal $w_g^\lambda/\lambda \cong 2 \cdot 10^{-5}$. The effective misorientation induced by defects like dislocations and inclusions is large compared to w_g^θ and fulfills conditions 2 and 3. We have selected the X-ray wavelength to work in the 'low-absorption' case $\mu t_{\text{max}} = 0.08$. Finally, the thickness of the crystal matrix ($t \cong 2$ mm) was such that its integrated reflectivity has already reached its saturation ($t \gg \Lambda_g, \Lambda_g = 107 \mu\text{m}$).

In principle the absorption of the scattered radiation has to be taken into account if one want to determine exactly the projection of the additional, diffracted intensity. Working with $\mu t_{\text{max}} = 0.08$ we could neglect this correction. Provided, the constant contribution of the perfect crystal matrix has been subtracted from the recorded topographs, we may conclude that the measured intensity is well approximated by the projection of the local reflectivity along the diffracted beam. The reconstruction of these projections by means of standard tomographic algorithms yields consequently the three-dimensional distribution of $R_{\mathbf{g}}^{\text{def}}(\mathbf{r})$. Regions close to dislocations (deformed lattice) have a positive value of $R_{\mathbf{g}}^{\text{def}}(\mathbf{r})$ and appear more white in the reconstruction.

Note that the images of individual dislocations have a width in the order of [Tan76]

$$w(\mathbf{b}, \lambda, F_g) \simeq \Lambda_g \frac{(\mathbf{g} \cdot \mathbf{b})}{2\pi} = \frac{V_c \cos \theta_B (\mathbf{g} \cdot \mathbf{b})}{2 r_e \lambda C (F_g F_{\bar{g}})^{\frac{1}{2}}} \quad (3.20)$$

where \mathbf{b} denotes the Burgers vector. In order to resolve individual dislocations the resolution of the detector, the density ρ and the width w of the dislocation images have to fulfill certain conditions. As a first condition we may state that the resolution of the detector should be smaller than the width of a dislocation image $r_d < w$. Moreover, in order to prevent the superposition of dislocations in the bulk of the sample, their density $\rho[\frac{m}{m^3}]$ should be small compared to

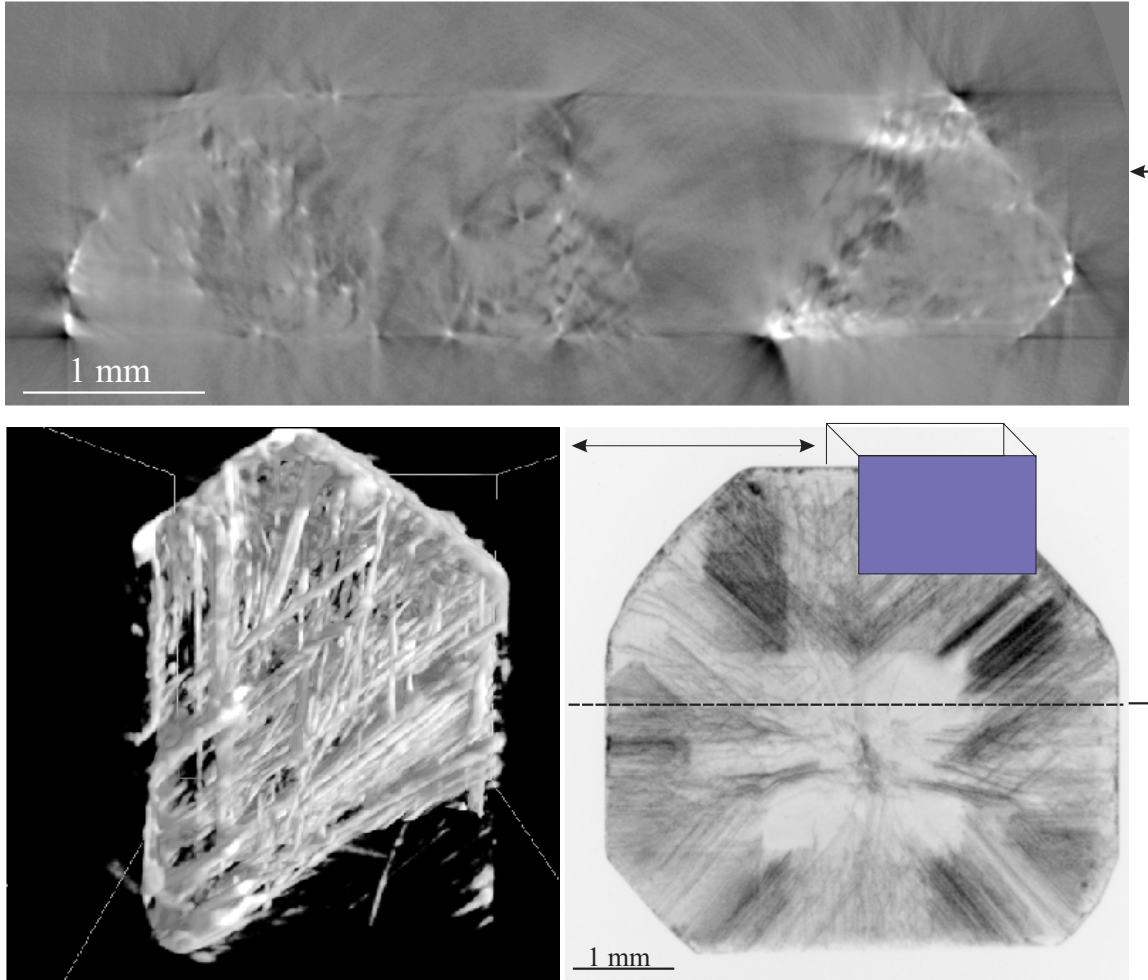


Figure 3.11: (a) Tomographic reconstruction of the local Bragg reflectivity $R_g(\mathbf{r})$ in a slice (see dashed line in Fig. 3.11c) perpendicular to the rotation axis. Lighter gray levels correspond to higher values of the local Bragg reflectivity $R_g(\mathbf{r})$. Dislocations threading the layer show up as point-like contrasts. (b) Volume rendition of the upper part of the crystal, indicated in Fig. 3.11c. Volume elements below a certain threshold are set to transparent. Line shaped contrasts, corresponding to dislocations with preferential orientations are observed

$\rho \ll 1/w^2$. Note that the apparent superposition of dislocations on single projections (2D) is *not* a limitation of this method. The tomographic reconstruction will correctly account for this case and reproduce the three-dimensional arrangement.

In order to minimise the width of the dislocation images and hence to improve the spatial resolution of the technique, the choice of a reflection with high structure factor and of rather large X-ray wavelength would be favourable from a "topographers" point of view. However, there are conflicting constraints:

1. The quality of the tomographic reconstruction depends critically on the azimuth angle ($\Psi = \theta_B$). Best resolution is obtained for $\Psi = 0$ and reconstructions are typically performed with Ψ values smaller than 5° .
2. Increased absorption will lead to artifacts in the reconstructed images as it alters the relation between the reflectivity and the recorded intensity in a non-linear way.

Consequently, a tradeoff between the conflicting requirements of topographic and tomographic imaging has to be made.

We shall also note that in addition to the presence of direct image contrast we may encounter pronounced interference effects, which depend in a complicated way on the sample geometry, surface quality, diffraction conditions, crystal quality,... In this case the diffracted intensity corresponds no longer to projections of the reflectivity and tomographic reconstruction does not produce satisfactory results. Such problems were encountered during our initial attempts to apply topo-tomography to the case of a perfect LBO crystal sample.

Let us finally remark that Fig. 3.11a can be considered as a virtual *section topograph* [Tan76], which could be obtained by restricting the width of the incoming beam to $\cong 7\mu\text{m}$. There are nevertheless two differences with respect to an actual experimental section topograph: (i) the plane of an experimental section topograph is inclined by θ_B with respect to the diffraction vector and (ii) our tomographic section was obtained from *integrated* projection topographs where most interference effects are averaged out. In the case of an actual section topograph these interference effects would be visible and provide further information about the strain field around defects. This information is not available in the case of topo-tomography which provides on the other hand the *three-dimensional* information about the position and geometry of the defects in the bulk of the crystal.

3.2.6 A possible variant for polycrystalline material

So far we have considered the case of a perfect single crystal. With the help of the same principle it should be possible to visualize individual grains in the bulk of polycrystalline material. In conventional absorption tomography one usually neglects deviations from the ideal transmission behaviour due to occasional diffraction effects when individual grains happen to fulfill Bragg's law for certain angular positions. These grains appear less intense on the detector, the 'missing' intensity being transferred to the diffracted beam. Due to the fact that the reconstruction is based on a large number of projections, these occasional diffraction effects do not lead to noticeable image degradation.

Another situation arises, if one intentionally aligns the polycrystal in such way, that the diffraction vector of a strong reflection in one of the crystal grains is parallel to the rotation axis. In this case the grain will diffract for all angular settings during the tomographic scan and the volume occupied by this grain will receive a higher attenuation coefficient, as the grain appears more absorbing in the projections.

This special configuration can consequently be used to determine the position and shape of an individual grain in the bulk of polycrystalline material in a *non-destructive* way. Note that this information is inaccessible in conventional absorption mode, where the individual grains cannot be distinguished. This technique might be of great interest for the time-resolved, three-dimensional analysis of grain-growth in the bulk of polycrystalline material.

3.2.7 Conclusion

We propose a new three-dimensional crystal characterization technique, based on the combination of X-ray diffraction topography and computed microtomography. The approach is applicable to high quality single-crystals, provided the dominant contrast mechanism is the *direct image* one. Integrated, monochromatic beam diffraction topographs may then be regarded as projections of the local Bragg reflectivity. Rotating the sample around the diffraction vector

will not significantly vary the diffraction conditions and allows to acquire a complete set of projections (Radon transform) which serves as input for the tomographic reconstruction. The reconstruction yields an approximation of the three-dimensional distribution of the local Bragg reflectivity inside the crystal and allows to analyse the orientation and position of individual dislocations inside the crystal.

A possible extension to the case of polycrystalline material is suggested. It is expected, that the same principle allows to determine the shape and position of individual grains in the bulk of a polycrystal.

Part II

Applications

Chapter 4

Grain boundary wetting

This chapter is devoted to the application of Synchrotron Radiation micro-imaging to a specific phenomenon in metallurgy: the wetting of grain boundaries by a liquid metal. After a short introduction and bibliographic survey of previous work we will present our experimental results obtained in the system aluminium - liquid gallium. In-situ measurements of the penetration process in bulk specimens allowed for the first time to demonstrate the direct link between grain boundary wetting and grain separation in this system. Combining different X-ray characterization techniques, we could also establish a method to analyse the wetting process in bulk polycrystalline material. We will conclude this chapter by the tentative interpretation of the results in terms of a fracture mechanism.

4.1 Introduction

When a polycrystalline solid is exposed to a liquid phase, rapid penetration ($10^{-3} - 100 \mu\text{m/s}$) of the liquid phase along the grain boundaries takes place in a variety of metallic and ceramic systems [CG92]. This process leads to the formation of liquid films with a typical width in the order of $0.1 - 10 \mu\text{m}$. The presence of such macroscopic, intergranular liquid films can be used to assist certain industrial manufacturing processes like high strain rate superplastic forming and sintering or chip fragmentation in rapid machining. On the other hand, the contact with a liquid metal may also entail severe degradation of the mechanical strength of the material. The latter phenomenon, known as liquid metal embrittlement (LME) [NO79, FJ97, JPB99, Gli00] is of relevance when structural metals are exposed to liquid metal environments under the simultaneous action of external or internal stresses. This is for example the case in common industrial processes like galvanising, soldering and welding (see e.g. [FCJ94]). The subject has gained renewed interest in recent years due to the active international efforts to develop 'safe' (undercritical), accelerator driven nuclear reactors where liquid metals serve as targets and cooling fluids.

Despite numerous efforts, the detailed mechanism(s) which lead to the formation of intergranular liquid films are still far from being well understood. A variety of models have been proposed in recent years [Fra94, BKA95, Rab98, GN99], however none of them can fully account for the different aspects of the penetration process. This might indicate, that the working mechanism is not the same in different systems. The situation is further complicated by the fact, that the problem is not well defined from an experimental point of view. The results depend not only on parameters like temperature, composition of the involved materials and the detailed nature of the grain boundary but also on parameters like:

- impurity segregation from the melt at the solid liquid interface
- total amount of liquid metal
- geometry of the sample (e.g. thin foils in TEM versus bulk specimens in SEM)
- thermo-mechanical treatment of the base material (residual stress)
- surrounding atmosphere (presence of oxygen, water, . . .)
- sample preparation and observation technique (in-situ versus ex-situ, volumetric changes during solidification)

Differences in these conditions complicate and may even prevent the comparison and analysis of experimental results. The analysis of the experimental data is further complicated by the fact, that the process takes place in the bulk of the sample - whereas conventional observation techniques are restricted to the sample surface (or polished sections) and thin foils. As a consequence, there is only limited and rather scattered data available, which might serve to corroborate or reject the different models which have been proposed.

4.2 General background about GBW

In order to adequately describe the thermodynamical properties of polycrystalline material, one has to take into account the phase transitions which may take place at the grain boundaries in the bulk of the material [Cah77, RSS91]. Among these phase transitions, grain boundary wetting (GBW) has attracted a lot of attention in recent years and will be considered in more detail.

Consider a bicrystal in contact with a liquid phase L (Fig. 4.1). If the grain boundary (GB) energy γ_{gb} is lower than twice the solid-liquid interface energy γ_{sl} , the boundary will not be wetted by the liquid phase and an equilibrium dihedral angle θ

$$\gamma_{gb} = 2\gamma_{sl} \cos \theta \quad (4.1)$$

will establish at the groove root (Fig. 4.1a). If the interface energies γ_{sl} and γ_{gb} depend on the temperature in a different way (Fig. 4.1c), there will exist a critical temperature T_{w1} , called the wetting temperature at which $\gamma_{gb} = 2\gamma_{sl}$ and the angle θ tends to zero. Above T_{w1} no grain boundary of this type can exist in equilibrium with the liquid phase: it will be replaced by two solid-liquid interfaces. GBW has been observed in a variety of metal systems (e.g. Cu-In, Ni-Bi, Al-Sn, Al-Ga . . .) and it has been experimentally verified, that the transition to zero dihedral angle occurs at different temperatures for grain boundaries of different energy [SMGP92, SGM94].

Most wetting experiments have been performed by applying presaturated liquid¹ to the external surface of pure solid metal. The level of saturation of the liquid metal is an important parameter, as it determines whether or not the penetration will be accompanied by dissolution processes. Note, that wetting could also be established by annealing of a saturated solid solution. The latter type of experiments is e.g. used to elucidate the relation between grain boundary segregation and grain boundary wetting transitions [CRS⁺99].

¹i.e. liquid of equilibrium composition according to the solid metal - liquid metal (binary) phase diagram

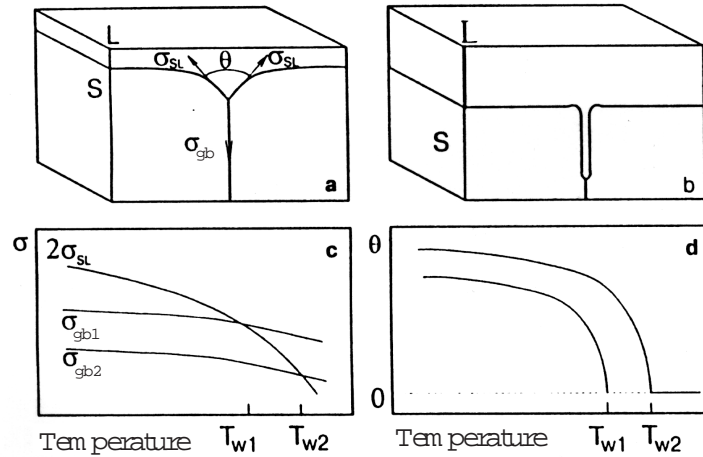


Figure 4.1: a) Grain boundary groove with equilibrium dihedral angle $\theta > 0$ ($T < T_w$). b) Wetted grain boundary with $\theta = 0$ ($T > T_w$) c) Temperature dependence of surface and grain boundary energies. d) Resulting temperature dependence of equilibrium dihedral angle for different grain boundaries [SGM94].

Whereas these basic characteristics of GBW are well established, the details of the atomistic and kinetic mechanisms which lead to GBW are far from being understood. Before presenting the key ideas of the different models dealing with this problem, we shall give a short definition of commonly encountered terms in the discussion of grain boundary wetting and related phenomena

Grain boundary diffusion. Compared to bulk crystalline material, grain boundaries have a less dense structure with a typical width in the order of 0.5 nm. They act therefore as short-circuits for diffusional mass transfer in solids. Grain boundary diffusion coefficients are considerable higher than diffusion coefficients in solid metal and depend strongly on the orientation and inclination of the boundary [KG89]. However, GBW is usually much faster than GB diffusion processes would allow and the observed linear kinetics are not in agreement with GB diffusion kinetics.

Thermal grooving. At the intersection of grain boundaries with the external sample surface thermal grooves with characteristic profiles and growth kinetics develop during annealing. The shape and temporal evolution of these *Mullins* grooves is well described in terms of a curvature driven surface diffusion model [Mul57]. The model has been extended recently in order to account for anisotropy effects [RKS00] which may lead to formation of singular (flat) groove walls. The equilibrium dihedral angle (governed by capillary forces $\gamma_{gb} = 2\gamma_{sv} \cos\theta$, where γ_{sv} denotes the solid-vacuum surface energy) is usually obtuse and close to 2 rad for most metals. It is possible to estimate the energy of different grain boundaries via the analysis of their dihedral angles [SMGP91]. Thermal grooves have convex groove walls and show a slow temporal evolution ($\sim t^{1/3}$ for bulk diffusion and $\sim t^{1/4}$ for the case of small grooves, where surface diffusion is the rate controlling process). Typical groove dimensions are in the order of a few micrometers after one hour of annealing.

Liquid grooving. If the external sample surface is exposed to liquid metal, the grooving mechanism is modified due to the additional transport mechanisms in the liquid phase (diffusion, convection). The dihedral angles and grooving rates depend further on value of the

spreading coefficient $S = \gamma_{gb} - 2\gamma_{sl}$:

- $S < 0$. The liquid phase does not wet the grain boundaries in this case. One observes again the formation of Mullins like grooves (see Fig. 4.1a), however with modified kinetics [Mul60].
- $S > 0$. The shape and kinetics of the liquid grooves differ significantly from the Mullins regime. One observes narrow, extended grooves with two characteristic shapes: i) finger like grooves with nearly parallel walls and a non-zero dihedral angle at the groove root which has convex-down curvature. ii) wedge shaped grooves. In this case it is often difficult to define the length of the groove as their width decreases continuously and can no longer be resolved with standard characterisation techniques. The growth of these liquid grooves is a non-equilibrium process which tends to establish perfect wetting. The term grain boundary wetting (see below) is therefore sometimes used as a synonym for the grooving process.

Grain boundary penetration. There is experimental evidence, that ahead of the finger-like grooves the grain boundary is already penetrated by atoms of the liquid phase. The concentration profile of the penetrating atoms is almost constant over distances of several tens of micrometers and cannot be explained by regular grain boundary diffusion. Systematic studies of the penetration of Zn along grain boundaries in Fe-Si alloys [RSSS91, NRS⁺91, SNS⁺92] have been interpreted as experimental evidence of so-called prewetting transitions, predicted theoretically by Cahn [Cah77]. Another interpretation of such abnormal concentration profiles in terms of stress driven diffusional drift has been proposed recently by Glickman [GN99].

Liquid metal embrittlement (LME) describes the reduction in ductility and strength of solid metals when they are loaded in the presence of a liquid metal. Note, that grain boundary wetting will also result in a macroscopic brittle failure of the material. Some authors proposed therefore wetting or penetration as one of the mechanisms of LME [GA82]. We will keep a distinction between both processes and refer to LME only in the presence of external or internal stresses.

Whereas there is common agreement about the role of surface energies and their minimization during the wetting process, the details of the grooving mechanism are still controversially discussed. Among the open questions are such fundamental points like the destination of the solid material: is it dissolved in the liquid phase and redeposited behind the groove root or is it pushed ahead of the moving groove tip? Unclear is further the kinetics of the penetration process, both in theory and in experiment. For the same system, some authors have observed linear, others parabolic penetration kinetics. This might serve as example for the importance of well defined experimental conditions. The transition from linear to parabolic kinetics suggests a change of the rate controlling process. Linear kinetics are compatible with an interface controlled mechanism. Parabolic kinetics on the other hand are expected for a diffusion controlled process. It might be speculated, that diffusional mass transfer through the liquid phase becomes the rate controlling process in the case of long grooves. Consequently, the experimental results depend also on the typical lengthscale of observation (a few tens of micrometers in TEM, millimeters in microscopy).

Finally, as pointed out by Rabkin [Rab98], it is unclear why such thick grooves are formed: due to screening effects in metals, the gain in free energy should be the same for a few monolayers of liquid and for a layer of 1 μm thickness.

4.3 Peculiarities of GBW in the Al/Ga system

It has been recognized for a long time, that the system Al/Ga shows a peculiar behavior compared to other solid metal/liquid metal systems. The following quotation of a materials science basic course [AJ86] might serve to illustrate this statement:

'A favorite scientific party trick is to put some aluminium sheet in a dish of molten gallium and watch the individual grains of aluminium come apart as the gallium whizzes down the boundary. . . . This wetting of the grain boundary can be a great nuisance, . . . cracks can spread along the grain boundaries until the metal fails apart completely'

It seems well established, that GBW plays a key role in the spectacular behavior of liquid Ga and Al. However, none of the proposed mechanisms of GBW (see appendix C) can account for the extremely high penetration rates (up to 100 $\mu\text{m/s}$) observed in this system.

Before presenting the essential results of previous studies, we give a short overview of relevant physical properties of the elements Al and Ga.

4.3.1 Material properties

Aluminium ($T_m=660^\circ\text{C}$) is a ductile metal (face-centred-cubic) of low density ($2.7\text{ g}\cdot\text{cm}^{-3}$) and high electric and thermal conductivity. Aluminium reacts in a highly exothermic way with oxygen and is covered by a protective oxide layer (Al_2O_3) which prevents further reaction in air. Aluminium is weakly absorbing and well suited as base material in high resolution X-ray imaging experiments. The mechanical properties of Al and its alloys depend strongly on the composition and the thermo-mechanical treatment of the material.

Gallium is a ductile metal (orthorhombic) of low melting point ($T_m=29.8^\circ\text{C}$) and the longest liquid range ($T_b=2205^\circ\text{C}$) of all elements. Ga contracts on melting ($\approx 1\%$) and is stable in water and air. Liquid Ga wets glass, porcelain and most other surfaces apart quartz, graphite and teflon.

The binary system Al/Ga (Fig. 4.2) shows the absence of any intermetallic phases and the existence of a low melting (26°C) eutectic with 8 at. %Al.

4.3.2 GBW and LME in the Al/Ga system

Several teams have studied the different aspects of grain boundary penetration and embrittlement of aluminium by liquid gallium. Many different techniques like optical and electron microscopy (SEM, TEM), secondary ion mass spectroscopy (SIMS), residual activity measurements (^{72}Ga), radiography, texture analysis, acoustic emission, and fractography have been used. A short summary of the results and the interpretations proposed by the corresponding authors is given below.

Embrittlement as a three-step process. Observations of a French team [RAL70, PRAW72, RAL73] indicate, that the embrittlement by liquid gallium may proceed as a three step process

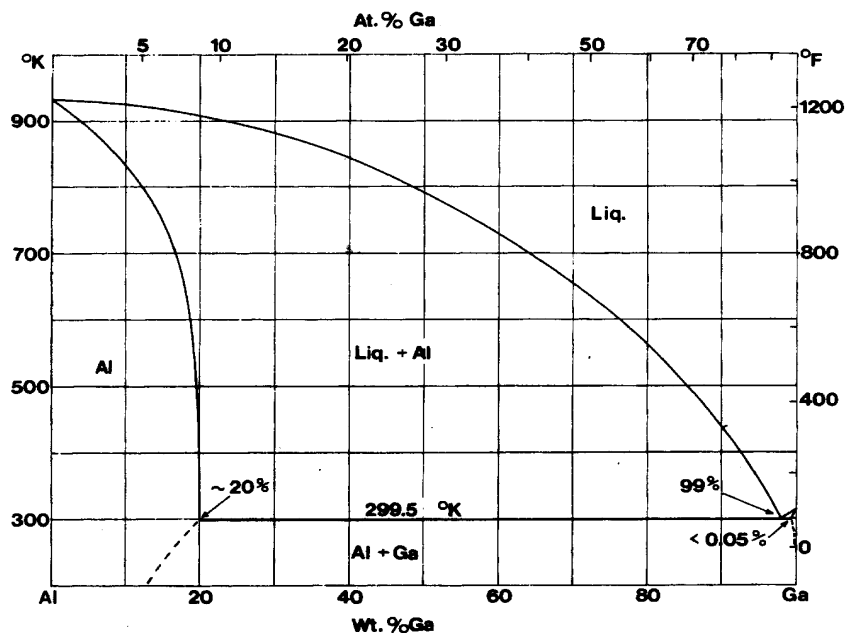


Figure 4.2: Phase diagram of the Al/Ga system [Mon76].

- During the first stage of penetration a thin Ga film (\sim monolayers ?) invades the grain boundary. This penetration does not provoke embrittlement - a finding which was confirmed by measurements on polycrystalline Al samples, electroplated with a thin ($0.1 \mu\text{m}$) depot of the radionuclid ^{72}Ga . The experimental technique (residual activity measurements) did not allow to determine the kinetic law during this penetration step.
- Macroscopic wetting layers ($\sim \mu\text{m}$) propagate along the grain boundaries (provided a sufficient supply of gallium). The propagation is accelerated by the external stress. Attempts to determine the penetration kinetics by interrupted X-ray radiography [Roq71] or mechanical testing were not conclusive. For large penetration times and distances (hours, several cm) $t^{1/2}$ kinetics seem to prevail.
- Finally, crack propagation is supposed to occur by an iterative process: the cracks start from the wetting front and propagate along the part of the grain boundary which is already weakened due to previous penetration of a liquid film. The crack length depends on the extent of the penetration zone and on the applied stress.

The French team clearly worked out the delayed failure mechanism due to the intergranular penetration of liquid gallium. Due to the high penetration rates, even in the absence of external stresses, it is experimentally difficult to distinguish between GBW and LME in this system. Experimental studies, reporting on instantaneous, "catastrophic" failure of Al/Ga should therefore be reviewed in the light of these findings.

First Principles calculations. The energetics of Ga on Al surfaces with low Miller indices and in a special grain boundary ($\Sigma 11(113)50.48^\circ$) have been simulated by ab-initio computer calculations. These calculations indicate, that Ga covered Al(100) surfaces have lower surface energies than Ga covered Al(111) or Al(110) surfaces [SF96]. These results are in agreement with the experimental observation, that cleavage surfaces of Al single-crystals which have been stressed during contact with liquid Ga are always Al(100) surfaces [OT79].

The segregation of Ga in a $\Sigma 11(113)50.48^\circ$ grain boundary revealed the importance of 'tight sites' in the boundary structure [THP⁺00]. The preferential occupation of these sites by Ga was explained in terms of a *two-radii* model for Ga atoms. To what extent these results are relevant also for general grain boundaries remains unclear.

In-situ TEM observations. Hugo and Hoagland performed a series of in-situ observations of the penetration process in thin TEM specimens of pure Al [HH98, HH99]. They observed linear penetration kinetics (0.1-10 $\mu\text{m/s}$) and a linear thickening rate ($\cong 0.1 \text{ nm/s}$) of the Ga layer. The penetration front is accompanied by a moving stress field which interacts with lattice and grain boundary dislocations. From these interactions they estimate that the initial width of the liquid film is in the range of 1-6 monolayers (below their instrumental resolution). Penetration rates depend strongly on the character of the grain boundary and are slow or absent for low angle and low Σ boundaries. Penetration speeds vary considerably for general high angle boundaries and atomistic simulations of these boundaries indicate that structural barriers influence the penetration kinetics in this case [HH00].

Apart the tendency of gallium to wet aluminium surfaces and to provoke LME or decohesion of the grains, the couple displays further intriguing characteristics like:

- small additions of Ga lead to accelerated grain growth [SSR⁺96]
- Ga increases the mobility of grain boundaries in Al(Ga) alloys [MCG⁺95]
- Ga may lead to superplastic behaviour of Al alloys [Mar76]

It turns out, that apart the TEM observations, none of the experimental techniques was capable to determine the kinetics of the penetration and/or wetting process in a direct way. It seems further well established, that the initial steps of penetration involve only small quantities of Ga (monolayers). Clearly, this length scale is inaccessible in X-ray imaging experiments based on absorption contrast. An attempt to characterize the wetting process and its kinetics by X-ray imaging will therefore be limited to the observation of macroscopic GB wetting layers² and/or liquid grooving at the sample surface.

4.4 Sample preparation

Our experiments were performed with aluminium samples of different composition and purity. The first experiments, feasibility studies, were performed with a commercial aluminium alloy (Al 5083). We then switched to aluminium of higher purity (99.8% and 99.996%). In-situ observations in polycrystalline material revealed the need for bicrystals of well defined boundary geometry for quantitative measurements. High quality aluminium bicrystals are not commercially available and require special preparation techniques. We received four such bicrystal specimens from a collaborating research group (M. Biscondi, K. Wolski and N. Marié, Ecole des Mines, St.Etienne).

The optimum size and shape of the samples depend on the imaging technique. Tomographic imaging is usually performed on cylindrical samples in order to take advantage of the entire field of view and to avoid reconstruction artefacts at sample borders. Radiography on the other hand

²The term *macroscopic* will be used to designate wetting layers which already have the characteristics of bulk liquid (\approx hundreds of monolayers).

is best performed on parallel, polished plates in order to ease quantitative contrast analysis and to avoid spurious image contrast arising from surface irregularities. In the hard X-ray spectral region, optimum sensitivity for detection of thin gallium layers is obtained close to the Ga K-edge at 10.4 keV. The thickness of the Aluminium substrate should be chosen close to $\mu t \approx 2$ in order to optimise the signal to noise ratio for a given exposure time in the case of absorption imaging [GE91].

4.4.1 Initial wetting contact

In-situ observation of liquid film propagation requires an experimentally simple method which allows to control the onset of the process. One possibility is to 'freeze' the process immediately after the wetting contact. The sample can then be transferred to the experiment and the process will continue as soon as the gallium is melted on the temperature controlled sample holder (Peltier heating element).

Although Ga has a strong tendency to wet Al surfaces [SF96], no wetting is observed on Al samples which have been exposed to air. This is due to the high reactivity of Al which leads to formation of a very stable surface oxide layer (Al_2O_3). However, if this oxide layer is broken locally and liquid Ga gets in direct contact with Al, the wetting will proceed until the whole (external) surface is covered by Ga.

A simple method to establish the initial wetting contact is to deposit a small droplet of liquid gallium on the sample and to scratch the surface under the droplet. It turned out difficult to observe the penetration right after (manual) deposition of liquid gallium. Instead of breaking the oxide mechanically, one can also remove it chemically, e.g. by immersion in a basic solution. The latter method allows to establish a more homogeneous wetting contact and avoids plastic deformation of the sample.

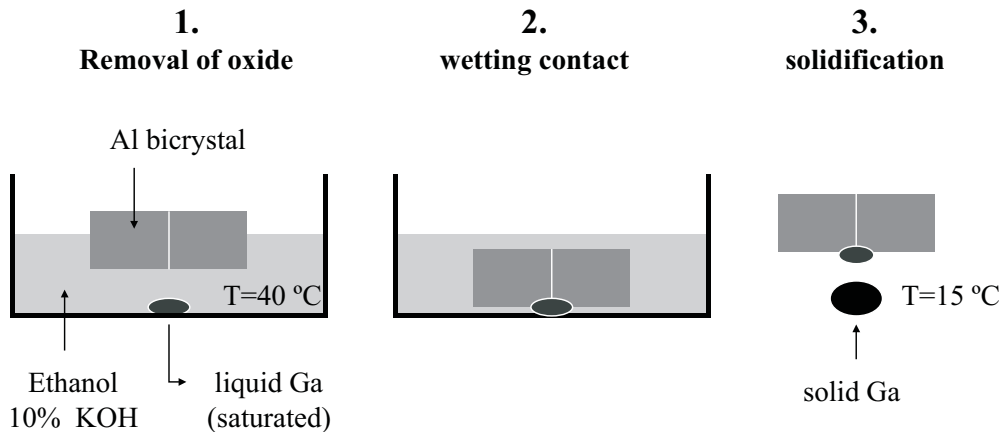


Figure 4.3: Ga deposition. 1. The surface oxide of the Al sample is removed by immersion in a 10 % KOH (Ethanol) solution ($T = 40^\circ\text{C}$, $t = 30$ s). 2. Wetting contact with a small droplet of liquid Ga (saturated with Al)($t = 5$ s). 3. The liquid Ga is immediately solidified by contact with solid Ga at $T = 15^\circ\text{C}$.

Just before the X-ray experiment the samples were immersed (≈ 30 s) in a solution of ethanol + 10% KOH in order to remove the oxide layer and to facilitate wetting with a small droplet of liquid Ga (saturated with Al), also immersed in the same solution. As soon as the Ga wetted the Al surface, the sample was removed from the solution and the Ga droplet was immediately

solidified by contact with solid Ga at $T = 15^\circ\text{C}$. The samples were rinsed, dried and kept below room temperature. The experiments itself were performed a few minutes afterwards in air and at room temperature (after a short heating to 30°C in order to remelt the Ga). Once remelted, the Ga remains liquid even at room temperature due to its pronounced tendency for undercooling [PA91]. The described method does not allow to control the thickness and the absolute amount of deposited gallium. This was however not required in our experiments because we were interested in an 'infinite' source of liquid metal in order to ensure that the wetting process would not be limited by the supply of liquid metal.

4.5 2D characterization of GBW

We characterized the wetting process in Al by two different imaging techniques: (i) X-ray micro-radiography and (ii) X-ray micro-tomography.

We will first present our results obtained with X-ray micro-radiography. This two dimensional imaging technique provides high spatial resolution ($\cong 1\mu\text{m}$) combined with high temporal resolution (typically fractions of seconds compared to several minutes acquisition time in tomographic imaging).

X-ray tomography was used to characterize the occurrence of GBW in the bulk of polycrystalline material (ex-situ observations after penetration) and will be presented in the second part. For the first time it was possible to observe these wetting layers without the need of sample preparation (polishing, sectioning) which might be a source of artifacts.

4.5.1 In-situ radiography

In order to ease quantitative image interpretation, X-radiography is best performed on thin Al plates, containing coarse grains which extend over the whole thickness of the sample. In this case, the images contain projections of individual grain boundaries which do not overlap.

A number of such samples were prepared from a $600\mu\text{m}$ thick sheet of 99.8 %Al. The material was first annealed 30 min at 600°C , then cold-rolled to 8 % and annealed again for 30 min at 600°C . This procedure resulted in an average grain size of 5 mm.

Typical X-ray radiographs ($E=14.5\text{ keV}$) of the coarse-grained 99.8 %Al polycrystal plates are shown in Fig. 4.4. The image on the left is taken 20 minutes after the deposition of liquid Ga at a sample border, about 5 mm away from the observed zone. The image shows a three grain junction with two wetted grain boundaries. The third boundary seems to be free of Ga. Close inspection of the image reveals however, that the boundary is already wetted by a thin film of Ga, however the thickness of the wetting layer is close to the resolution/sensitivity limit of the set-up. Figure 4.4b shows the same sample, imaged 55 min after the deposition of Ga. Although the contrast is still weak, grain boundary 'C' is now clearly distinguishable.

The transmission curves along the profiles (1) and (2) (see Fig. 4.4b) are shown in Fig. 4.5 a and b respectively. At the intersection between the GB and the sample surface, the profiles exhibit two strong minima. This surplus of Ga at the intersection is attributed to the formation of surface grooves (see § 4.2). The observed variations in transmission can be translated into variations of the Ga layer thickness. The profile in Fig. 4.5a shows that the amount of Ga in grain boundary C is not yet sufficient to be clearly observed after 20 minutes. One can just estimate that the projected Ga layer is not thicker than about 100 nm. However, the projected layer thickness within grain boundary C can be estimated after 55 minutes: one obtains about

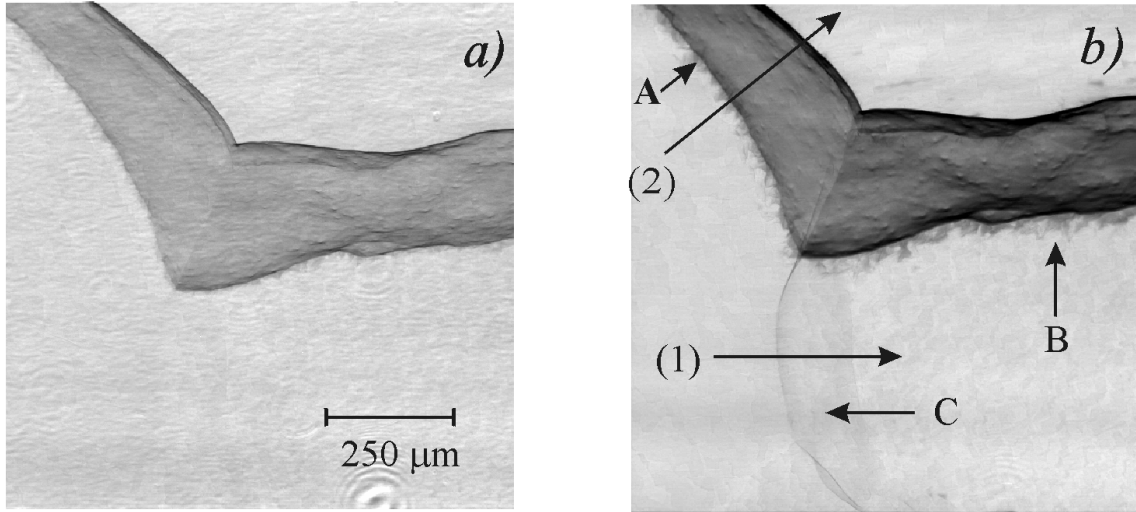


Figure 4.4: X-ray radiographs of a $600 \mu\text{m}$ thick, coarse grained Al sample. The images show the vicinity of a triple junction, for two different times, a) 20 min and b) 55 min, after application of Ga. The three grain boundaries are noted as A, B and C. The incident X-ray beam direction is perpendicular to the sample surface.

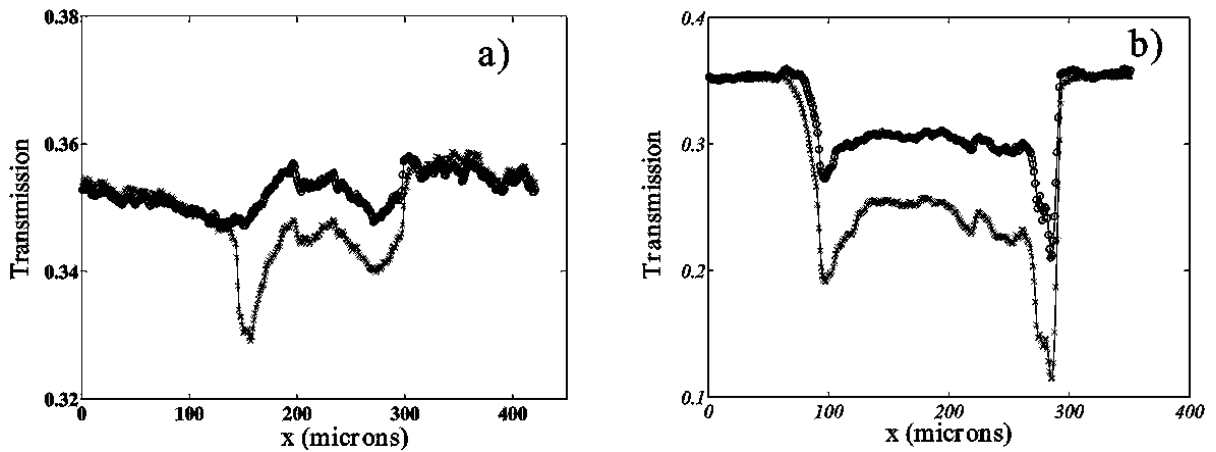


Figure 4.5: a) Transmission along profile (1), (o) and (x) correspond to 20 and 55 minutes, respectively, after the deposition of Ga; b) idem for profile (2).

500 nm. For grain boundary A, one gets $t_p = 2.7 \mu\text{m}$ and $6.4 \mu\text{m}$, respectively for 20 and 55 minutes after the Ga application. These values correspond to the projected thickness t_p which has to be corrected since the GB is inclined by an angle φ with respect to the incoming X-ray beam (see Fig. 4.6). The angle φ can be estimated from the known sample thickness and the apparent width of the GB in Fig. 4.4. With this correction (multiplication by $\sin \varphi$) one gets the following estimates for the thickness of the Ga layers: $t_l = 150 \text{ nm}$ for grain boundary C (55 min), and $t_l = 1.1 \mu\text{m}$ ($2.6 \mu\text{m}$) for grain boundary A, 20 min (55 min) after the deposition. Note, that changes in the inclination of the GB give rise to local contrast variations due to the change of the effective layer thickness (see Fig. 4.6).

The chosen example is representative for GBW in Al in a number of aspects. Firstly, it shows that the thickness of the wetting layer varies significantly between grain boundaries. It further

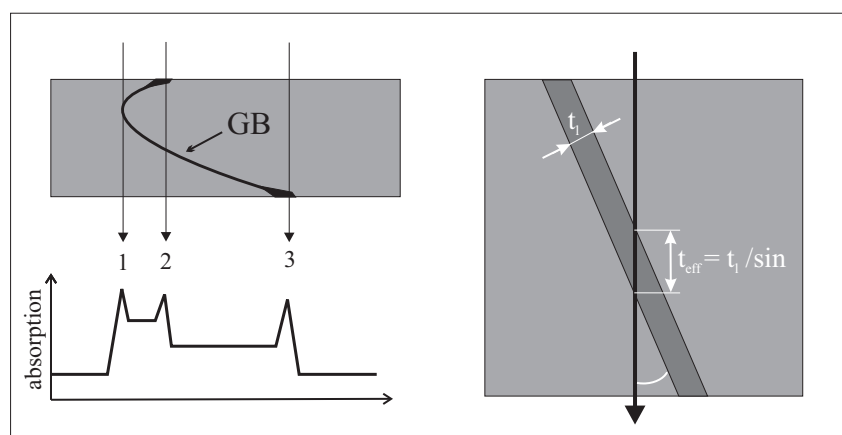


Figure 4.6: Contrast variations in the radiographs may arise from the surplus of Ga at the intersection of the GB with the sample surface (formation of liquid grooves) as well as from differences in the inclination of the grain boundaries with respect to the direction of the X-ray beam.

reveals, that the total amount of Ga increases with time and that the rate of increase depends again on the individual grain boundaries. Finally, the sample is observed to disintegrate into individual grains under weak mechanical load after the experiments.

Grain displacement during wetting

The formation of micrometer thick wetting layers, as observed in the previous example may take place by two different mechanisms:

1. removal of the solid material from the liquid groove by some kind of dissolution and/or diffusion mechanism
2. separation of the grains by a distance corresponding to the thickness of the intruding liquid film.

The comparison of tomographic reconstructions before and after application of liquid Ga revealed a displacement of the grains in aluminium alloy (§ 4.6.3) and gave already evidence for the second mechanism. However, these experiments did not allow to decide whether the displacement occurred *during* or *after* the wetting process (e.g. by sliding of the wetted grains).

We studied the relation of both processes, i.e. the thickening of the liquid film and displacement of the grains by means of fast radiographic imaging during penetration of an Al polycrystal of identical preparation and geometry like in the previous example.

Figure 4.7 shows two out of a series of 300 images recorded during the thickening of the wetting layer. The exposure time was 0.5 seconds per image, resulting in an acquisition rate of one image per second.

Logarithmic subtraction of the images before the onset of wetting allows to calculate the projected thickness³ of the wetting layer. The temporal evolution of the mean projected thickness in the three rectangular regions (A,B & C) is depicted in Fig. 4.8. A first continuous increase of

³Due to the unknown boundary geometry it is not possible to determine the absolute thickness in a reliable way

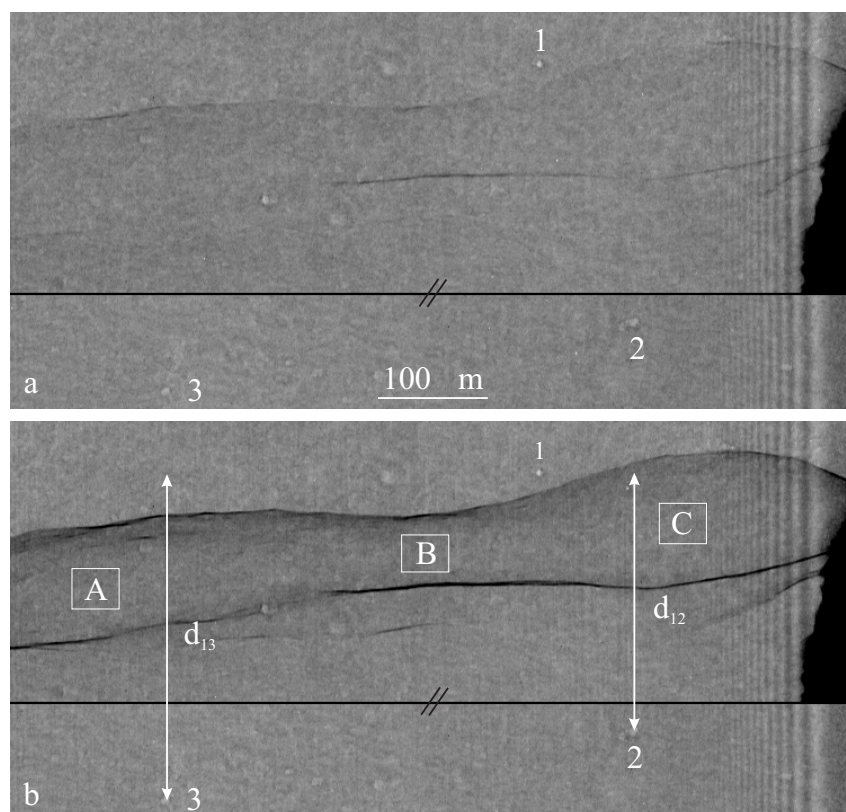


Figure 4.7: Two radiographs illustrating the discontinuous character of wetting in polycrystals. The images were taken at $t=140$ s and $t=150$ s and show the sudden increase of the Ga layer thickness during this time interval. The points 1,2,3 correspond to small porosities. The distance between porosities (1,2) and (1,3) increases at the same rate as the wetting layer grows in thickness.

the thickness is discernible in the time interval between 80 and 140 seconds. Inspection of the corresponding images reveals, that weak Ga contrast is already observed all along the boundary. The image in Fig. 4.7a was recorded at $t=140$ s. Within a few seconds a sudden increase of the layer thickness occurs and leads to the situation depicted in Fig. 4.7b. After this 'accident' the thickness continues to increase with the slow initial rate.

The displacement of both grains was determined by observation of the position of small porosities on either side of the boundary. Using cross-correlation techniques, we determined the time evolution of the relative vertical displacement between points 1 and 2 (d_{12}) and points 1 and 3 (d_{13}). The shape of these curves shows the same characteristics: a slow, continuous increase and a sudden displacement at $t=150$ s.

The complicated shape of the boundary, as well as the rather low image acquisition rate did not allow to determine the propagation rate of the wetting layer along the boundary in a reliable way. Nevertheless, an estimate in the order of $25 \pm 10 \mu\text{m/s}$ can be given.

At this point we shall mention an interesting observation, obtained during first feasibility studies for in-situ radiographic observation of the penetration process. These initial tests were performed with thin plates ($400 \mu\text{m}$) of an extruded Al alloy (see §4.6.3), which finally proved to be less adapted due to its complicated microstructure (Al5083, see § 4.6.3). Figure 4.9 (a-e) shows five images which have been recorded with a frame rate of 1 image/s during the penetration process. The images have been divided by an image before the arrival of the Ga

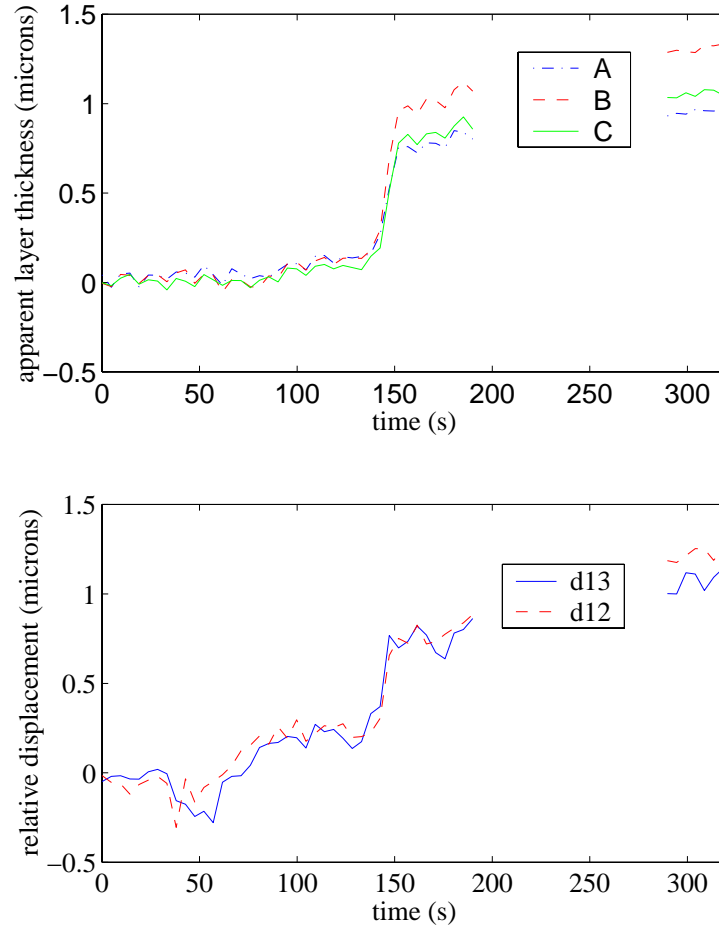


Figure 4.8: (a) Temporal evolution of the projected layer thickness in regions A,B and C, (Fig. 4.7) (b) evolution of the relative vertical displacement between points 1-2 and 1-3 (Fig. 4.7).

front, i.e. image contrast is only due to the presence of Ga. Between images (b) and (c) ($\Delta t = 1$ s) a sudden displacement of the Ga front over a length of $\cong 170 \mu\text{m}$ is observed. The discontinuous character of the propagation is further illustrated by the images in the lower row, which show the relative change between the consecutive images (a)-(e). Only weak changes are detected between images (a-b) and (d-e), whereas strong changes occur between images (b-c) and to a lesser extend also between images(c-d).

Summarizing, the presented in-situ observations on polycrystalline material (99.8%Al and Al5083) revealed the following characteristics:

- the thickness of the wetting layer increases with time and may reach a few μm .
- the thickening of the wetting layer and the displacement of the adjacent grains are correlated in time
- propagation along the GB is very rapid (several tens of $\mu\text{m/s}$)
- both processes, thickening and propagation have a discontinuous character

The experiments revealed further, that quantitative measurements of the penetration kinetics require higher image acquisition rates and grain boundaries of perfect geometrical shape.

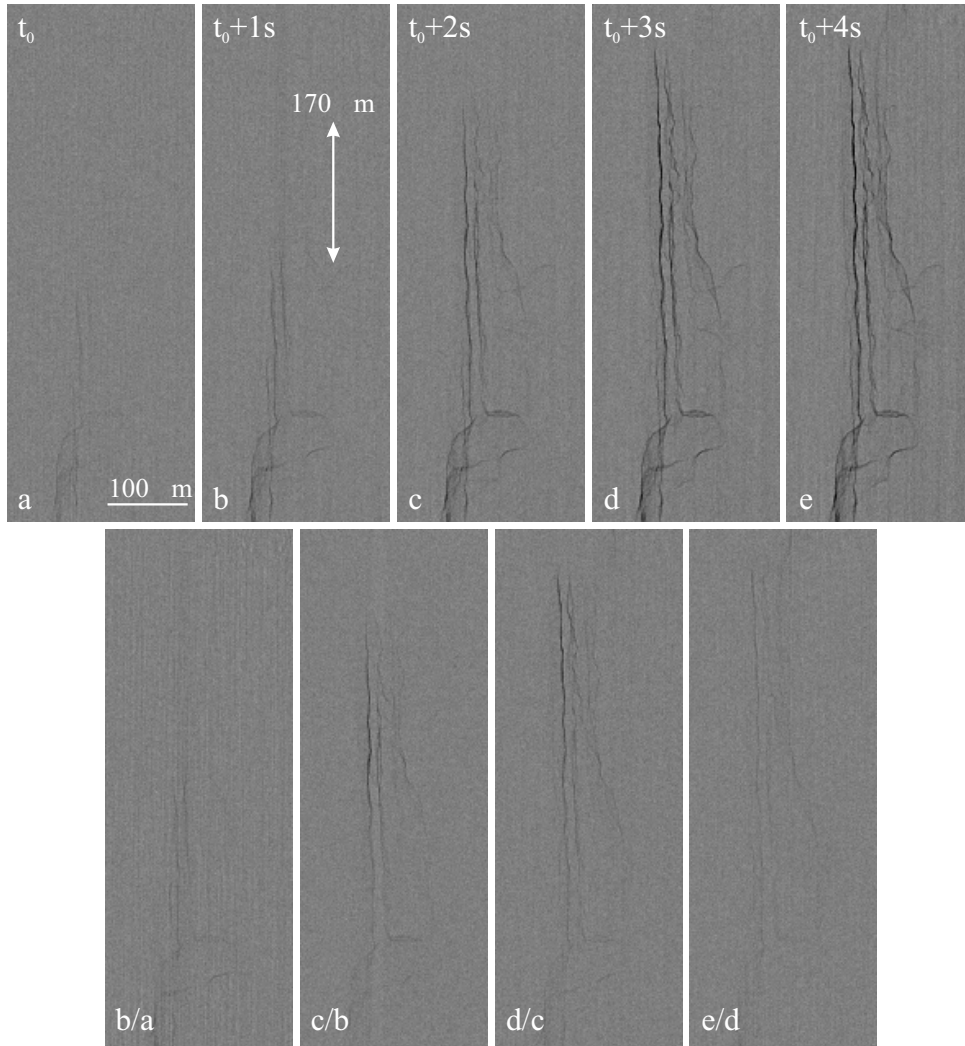


Figure 4.9: In-situ observation of the propagation of liquid Ga along the grain boundaries in a thin plate ($400\ \mu\text{m}$) of extruded Al alloy (Al5083). Five consecutive images (a)-(e) show the rapid penetration of the intruding Ga film. The process has a discontinuous character, as demonstrated by the images in the bottom row, which represent the change in the amount of Ga between the images of the top row.

4.5.2 Observations with Al bicrystals

The measurement of the propagation kinetics is best performed in perfect bicrystal boundaries, prepared by special growth techniques. We received four such bicrystal samples from a collaborating research group (M. Biscondi et al., Ecole des Mines, St. Etienne). The $600\ \mu\text{m}$ thick slices were spark-cut from two 99.996% Al bicrystal ingots with different misorientation:

150° symmetrical tilt around $\langle 110 \rangle$ (general boundary)

$129^\circ 30'$ symmetrical tilt around $\langle 110 \rangle$ (113 twin boundary)

Previous experiments showed, that the standard available image acquisition rate was not sufficient for adequate characterization of the penetration kinetics. We used an optimized acquisition

mode (see §2.3.3) which allowed us to monitor the penetration with a frame rate of 6.3 images/s. Figure 4.10 shows four out of the series of 270 images which have been recorded during the initial stage of wetting. The image of the sample before penetration has been subtracted logarithmically from the images shown in Fig. 4.10, i.e. the contrast is proportional to the amount of Ga, projected along the X-ray path.

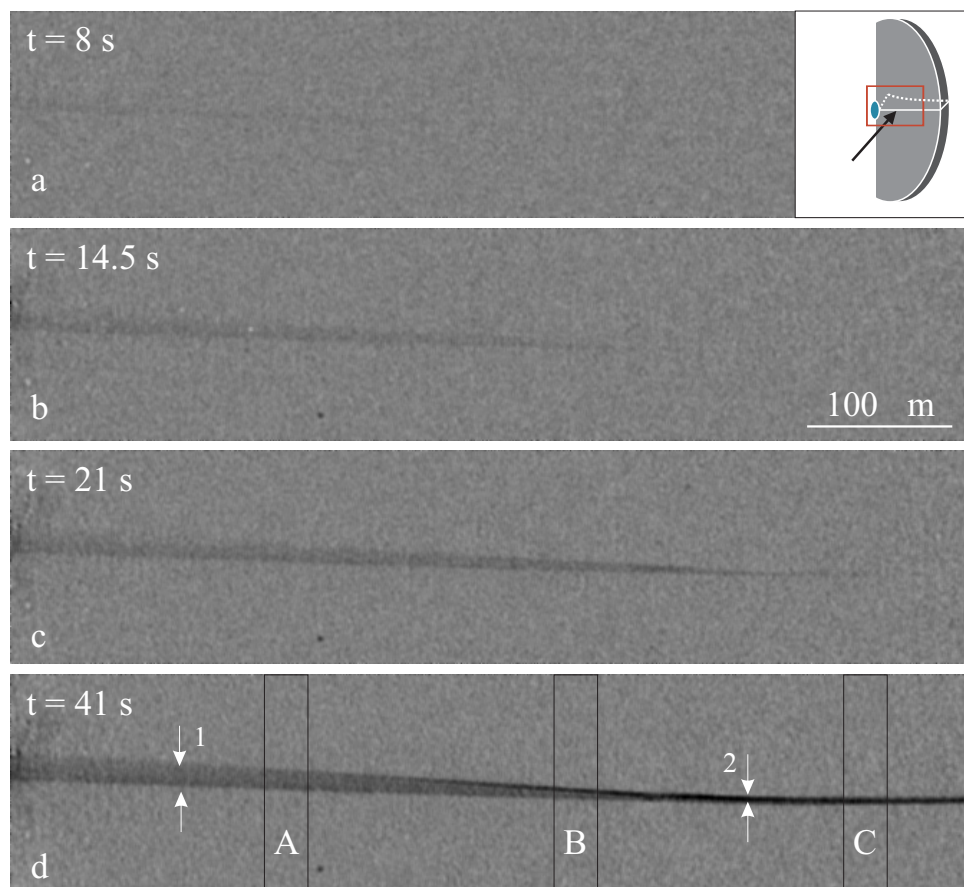


Figure 4.10: In-situ observation of GBW in Al bicrystal (150° symmetrical tilt around $\langle 110 \rangle$). The images show the propagation and thickening of the liquid film. The boundary is almost parallel to the beam direction: the different widths at positions (1) and (2) result from a slight curvature of the boundary plane and is *not* connected to the thickness of the Ga layer itself.

The leading edge of the penetration front is not clearly distinguishable by eye. However, the analysis of the absorption signal, averaged over small stripes like the ones depicted in Fig. 4.10d shows a distinct time offset which depends on the position along the grain boundary (Fig. 4.11 a).

The depicted absorption profiles show a linear increase of the Ga layer thickness with time. The thickening rate depends on the position along the boundary and varies between 0.8 and 1.4 nm/s. At the end of the image sequence ($t = 45$ s), the thickness of the Ga layer was still increasing. For technical reasons it was not possible to continue the observation directly after acquisition of the sequence. An image taken 10 min after the onset of wetting revealed an average film thickness in the order of $0.46 \mu\text{m}$.

In order to determine the penetration rate of the liquid film along the GB, we divided the image in equi-spaced stripes of $20 \mu\text{m}$ width and calculated the temporal evolution of the absorption

signal in each of these stripes. A straight line was fitted to these absorption profiles (linear least squares fit). The time of the passage (t_i) of the penetration front in the individual stripes was determined from the intercepts of the straight lines with the base line (e.g. times t_1 , t_2 and t_3 in Fig. 4.11a).

Figure 4.11b is a plot of t_i for the different stripes along the grain boundary. It turns out, that the boundary is almost simultaneously wetted over the first 200 μm . For larger distances (200-600 μm), the penetration is well described by a linear law. Fitting a straight line to this part yields a mean penetration speed of 25 $\mu\text{m/s}$.

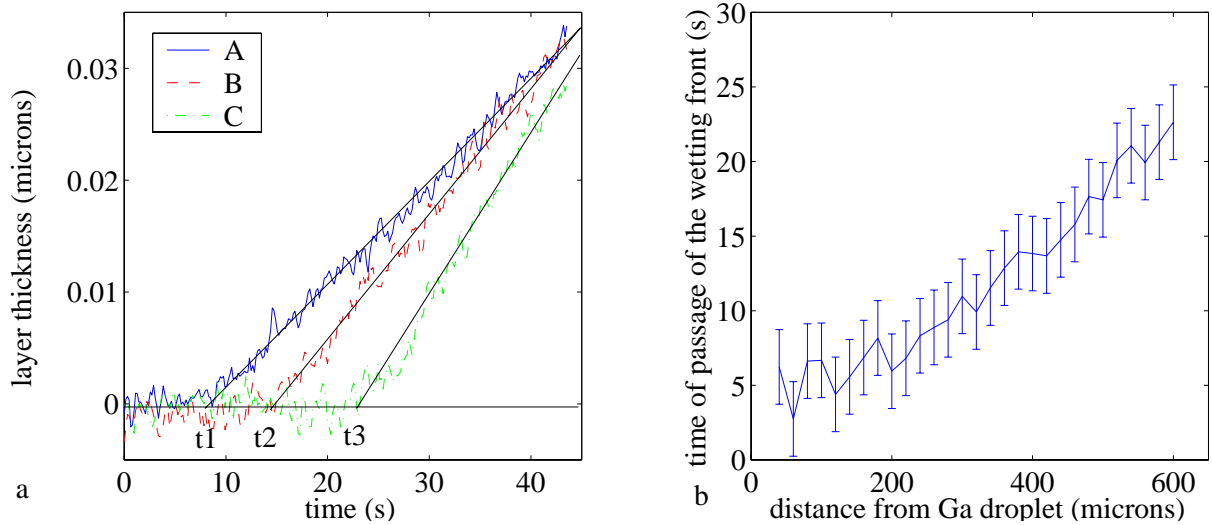


Figure 4.11: (a) Temporal evolution of the Ga layer thickness in regions A, B and C (see Fig. 4.10), (b) time of passage of the penetration front as function of the distance from the external Ga reservoir.

A second experiment with an identical bicrystal (cut from the same ingot) was performed at a lower acquisition rate (1.5 images/s). In this case it was possible to monitor the thickness of the Ga layer continuously until it reached a stable value of about 260 nm some 160 s after onset of the wetting process. Due to the poorer contrast (stronger inclination of the GB with respect to the X-ray beam), the mean propagation speed could not be determined by the same automatic procedure. Nevertheless, visual inspection of the images allowed to estimate the mean propagation rate in the order of 10 $\mu\text{m/s}$. It is interesting to note, that the thickness stops to increase after 270 s seconds. It is likely that this sudden change in the temporal evolution of the layer thickness corresponds to the time of arrival of the wetting front at the other end of 4.5 mm long grain boundary. In this case the mean propagation speed would be slightly higher ($\cong 17 \mu\text{m/s}$).

No wetting layer could be detected in the second type of bicrystals containing a $129^\circ 30'$ $\langle 110 \rangle$ symmetrical tilt boundary (113 twin boundary). Increasing the temperature up to 200 $^\circ\text{C}$ did not change this situation. It is known that 113 twin boundaries have a lower energy compared to general grain boundaries. The absence of wetting might be an indication for a negative wetting coefficient $S = \gamma_{gb} - 2\gamma_{sl}$ in this case.

We will now compare these results to tomographic observations of GBW in Al/Ga. The possibility to analyse the wetting layers in three dimensions eliminates the uncertainties arising

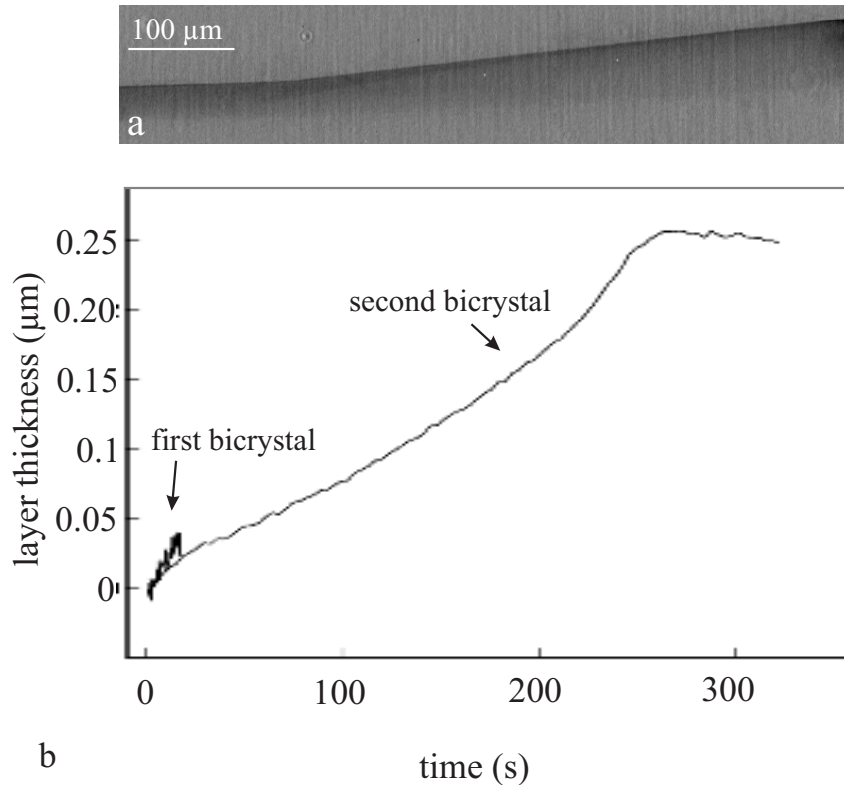


Figure 4.12: (a) Radiograph of the second bicrystal 300 s after the onset of wetting. (b) Temporal evolution of the mean Ga layer thickness (corrected for the inclination of the GB plane).

from the unknown GB geometry. Moreover, combined with adequate diffraction techniques, a large number of GB can be analysed simultaneously.

4.6 3D characterization of GBW in polycrystals

The use of well defined bicrystals is common practice for quantitative and systematic studies of grain boundary properties. Nevertheless, it is always instructive to perform complementary studies with polycrystalline material, containing a random distribution of grain boundaries. The energy distribution of grain boundaries in polycrystalline material is expected to influence the wetting behaviour: grain boundaries with an energy $\gamma_{gb} < 2\gamma_{sl}$ will not be wetted by the liquid phase (negative spreading coefficient S).

The interpretation of experimental results is however complicated by the fact that the grain boundary energy γ_{gb} cannot be determined in a simple and reliable way. There is no general expression which allows to calculate the grain boundary energy γ_{gb} from knowledge of the 5 macroscopic parameters defining the boundary geometry⁴ [Ran93]. However, in the case of low angle boundaries ($\theta < 10^\circ$) and for some special boundary geometries (periodic, coincidence site lattice (CSL) boundaries) the GB energy depends in a linear way on the misorientation θ between the grains. The analysis of a big number of such grain boundaries should therefore allow to study the influence of the spreading coefficient S on the wetting process.

⁴Two lattices of arbitrary orientation can be aligned by a rotation θ around an axis \mathbf{a} (3 parameters). The orientation of the boundary itself is determined by the GB normal \mathbf{n} (2 parameters).

From an experimental point of view this analysis is demanding: in-situ observations of the wetting process in a polycrystalline material have to be combined with a technique which allows to determine the grain boundary nature (defined by the five macroscopic GB parameters). We explored the possibility to perform this type of analysis by two complementary, three-dimensional X-ray imaging techniques:

1. X-ray microtomography was used to characterize the spatial distribution and amount of liquid Ga in the bulk of a wetted polycrystal.
2. The X-ray tracking technique [PNL⁺] was used to determine the orientation and shape of the individual grains. Based on X-ray diffraction, this method is independent of whether or not liquid Ga is present in the grain boundaries.

As the automatic processing of the X-ray tracking data is not yet available, so far only a limited number of these data could be analysed by S. F. Nielsen, Risø. Nevertheless, these first results serve to demonstrate the interest and potential of this combined approach for the characterization of GBW in bulk polycrystals.

4.6.1 Microtomographic characterization of Al polycrystals

Coarse grained Al polycrystals of cylindrical shape were prepared from 99.996% pure Al. The samples were annealed during 12 hours at 500°C in order to reduce the mosaic spread of the grains. We performed tomographic scans before and after application of Ga to the surface. Apart some small spherical porosities no contrast is visible inside the samples before application of Ga (Fig. 4.13a). Figure 4.13b shows the same section of the sample, 30 min after application of liquid gallium. A network of wetted grain boundaries (white lines) is visible after application of Ga to the sample surface. The greyscale in the images is proportional to the linear attenuation coefficient with white corresponding to highest X-ray attenuation. The dark lines which seem to prolongate the straight sections of the wetted grain boundaries have no physical meaning but are reconstruction artifacts.⁵ The reconstruction in Figure 4.13b is representative for pure Al, and shows a number of interesting characteristics:

1. The apparent width of the wetting layer varies from boundary to boundary. Variations inside a given boundary are less frequent and often connected with changes in the inclination of the boundary.
2. There are 'missing' grain boundaries, i.e. boundaries which are apparently not wetted by liquid Ga (see Fig. 4.13d) (at least within the actual resolution/sensitivity limit of our technique)
3. The distance between small porosities in different grains increases after application of liquid Ga. Relative displacements up to 4 μm can be detected between porosities which are separated by wetted grain boundaries. The displacement increases with the number of crossed boundaries and no displacement could be detected for porosities which are located in the same grain.

The latter point is illustrated in more detail in Fig. 4.13c. It shows the difference of images 4.13a and 4.13b. Both images have been carefully aligned with respect to porosity (3): no contrast

⁵caused by the tails of the LSF of the detector system

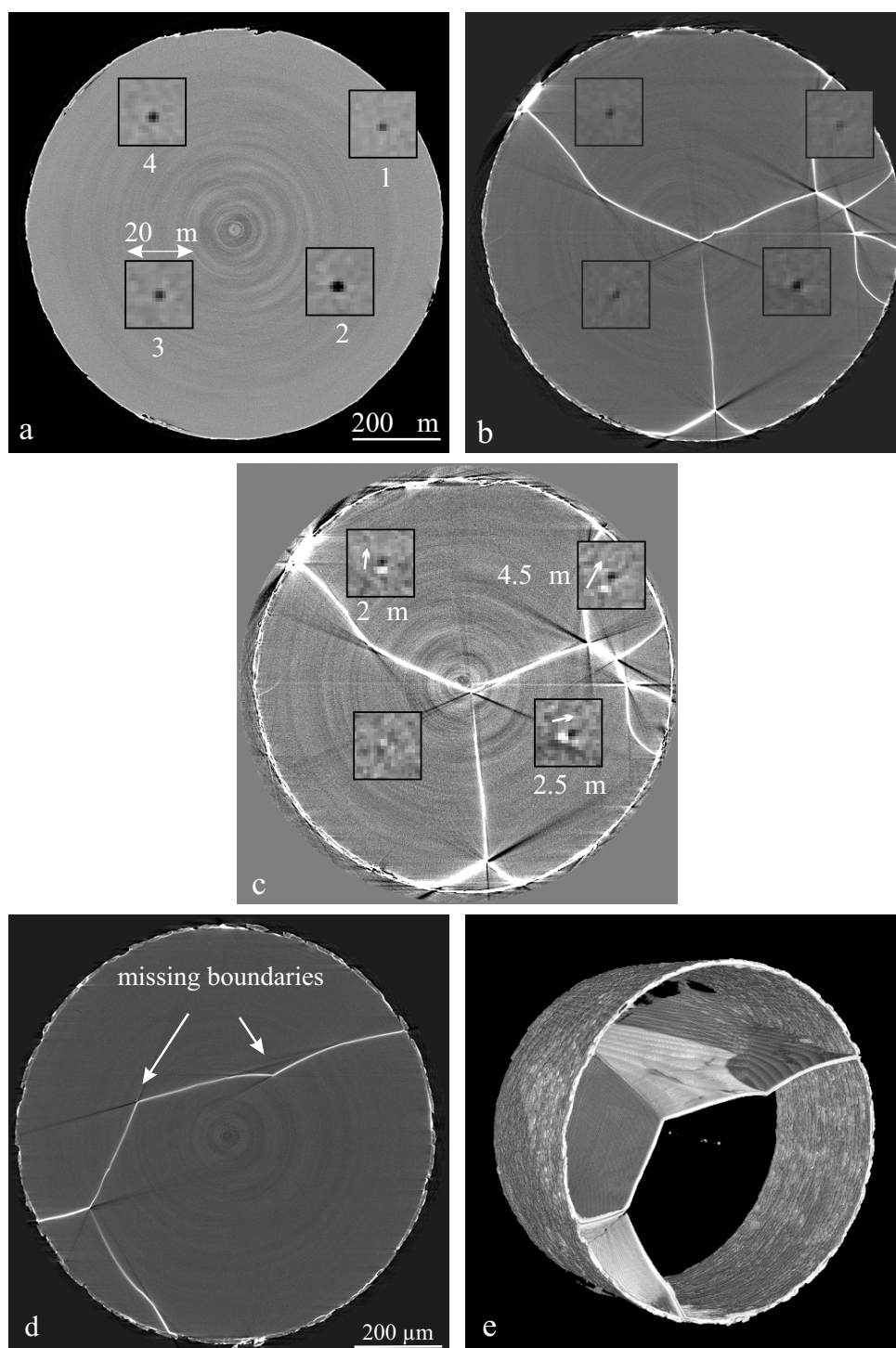


Figure 4.13: (a) Tomographic reconstruction of a 99.996% pure Al sample before application of Ga. The four zoomed regions ($8\times$) show small, micrometer sized porosities in the material. (b) Same section (see porosities) 30 min after application of liquid gallium. (c) Difference of images (a) and (b), centered on the porosity #3. The displacement vector corresponds well to the thickness of the wetting layers between the porosities. (d) Section through the same sample, showing two triple points with not wetted boundaries. (e) Volume rendering of the wetting layers .

is observed for this porosity. However, distinct black white contrasts are observed for the three other porosities, indicating, that the grains moved with respect to each other. The direction of the movement is indicated by arrows, and corresponds well to the expected movement due to the grain boundary structure.

These observations have been complemented by the analysis of the actual grain structure in the *same* sample by means of the X-ray tracking technique, presented in the next section.

4.6.2 Characterization by X-ray tracking

The X-ray tracking technique [PNL⁺] has been developed and implemented recently at the ESRF (ID11B) by members of the RisceNational Laboratory, Denmark (H.F. Poulsen, S.F. Nielsen et al.). The goal of this technique is to determine the position, shape and crystallographic orientation of the individual grains in the bulk of polycrystalline materials in a non-destructive way.

The technique is based on a monochromatic high energy X-ray beam (50 - 80 keV) and a 2-dimensional detector. The principle is sketched in Fig. 4.14. The incoming beam is focused by a bent Laue monochromator [LSH⁺98] into a line that defines a horizontal layer ($\approx 5 \mu\text{m}$ width) within the sample. All grains that happen to fulfill Bragg's conditions in this layer give rise to diffraction spots on the detector. The diffraction spots are the projected image of the corresponding diffracting grains in the observed layer. While an exposure is made, the sample is oscillated over a range $\Delta\omega$ to obtain a complete integration of the Bragg intensity. The necessary $\Delta\omega$ value depends on the mosaic spread of the grains. The intensity-weighted centre-of-mass (CM) of each diffraction spot is computed and this procedure is repeated at several sample - detector distances corresponding to different L values in Fig. 4.14. Linear fits through corresponding CM points extrapolate to the CM of the diffracting grains and provides the angles 2θ and η (see Fig. 4.14). To obtain the cross-sectional grain shape, the periphery of the diffraction spot in the image acquired at the closest distance is projected into the illuminated sample plane along the direction determined by the fit. The periphery of the diffraction spots is determined by setting a fixed intensity threshold. By rotating the sample around an axis ω , perpendicular to the illuminated plane, all grains will come to fulfill the Bragg condition and a complete map of all grain boundaries and grain orientations in the plane is thus produced. A three-dimensional map can then be obtained simply by translating the sample in z and repeating the procedure for several layers.

Images were acquired at three different detector positions ($L = 6, 8$ and 10 mm), and 30 ω -settings ($\pm 15^\circ$, $\Delta\omega = 2^\circ$). The data acquisition time was typically of the order of 11 minutes for one layer in the sample.

The analysis of the tracking data has been performed by S.F. Nielsen, Risce. First results are presented in Fig. 4.15 which shows the grain boundaries in four different layers, separated by $100 \mu\text{m}$. The determined grain boundaries in Fig. 4.15 represent the raw data with no interpolation or averaging. The accuracy in the determination of the grain boundary position is in the order of $40 \mu\text{m}$. When the sample is rotated in ω , several reflections will be observed from the same grain. A better fit of the grain boundary ($\cong 10 \mu\text{m}$) structure could be obtained by averaging between the different reflections from the same grain or taking the neighbouring grains into account.

In the left row of Fig. 4.16 the tomographic reconstructions, corresponding to the sections in Fig. 4.15 are shown. The middle row shows the superposition of the results obtained with tomography and X-ray tracking. Note that the tracking technique detects the 'missing' grain

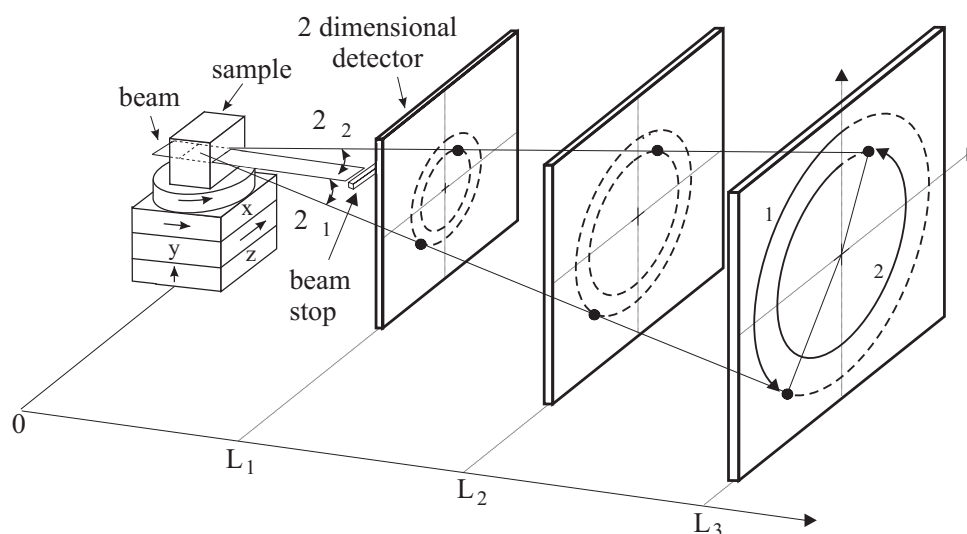


Figure 4.14: Illustration of the tracking technique. When the detector is translated away from the sample the diffraction spots will move outwards on the detector. The positions of the diffracting grains in the sample are determined by linear fits of the position of the diffraction spots. The fits also provide the 2θ and η values.

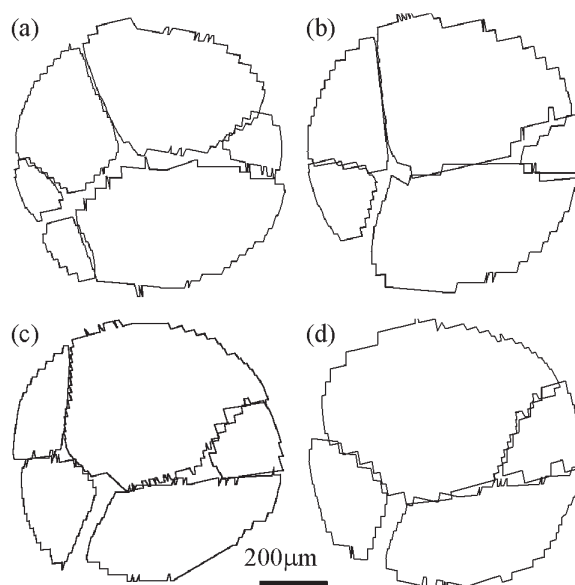


Figure 4.15: Four sections through the cylindrical Al sample reconstructed by X-ray tracking. The black lines correspond to the grain boundaries. The depth of the four sections are from the top of the sample: (a) $100\ \mu\text{m}$ (b) $200\ \mu\text{m}$ (c) $300\ \mu\text{m}$ (d) $400\ \mu\text{m}$.

boundaries which are not decorated with Ga. Moreover, the X-ray tracking provides not only the approximate shape, but also the crystallographic orientation of each grain. The misorientation between neighbouring grains, calculated from the grain orientations, are listed in the schematic representation shown in the right column of Fig. 4.16. Full lines correspond to boundaries determined by both techniques and dotted lines to boundaries only detected in the tracking experiment. At present only two boundaries that are not decorated with Ga have been detected

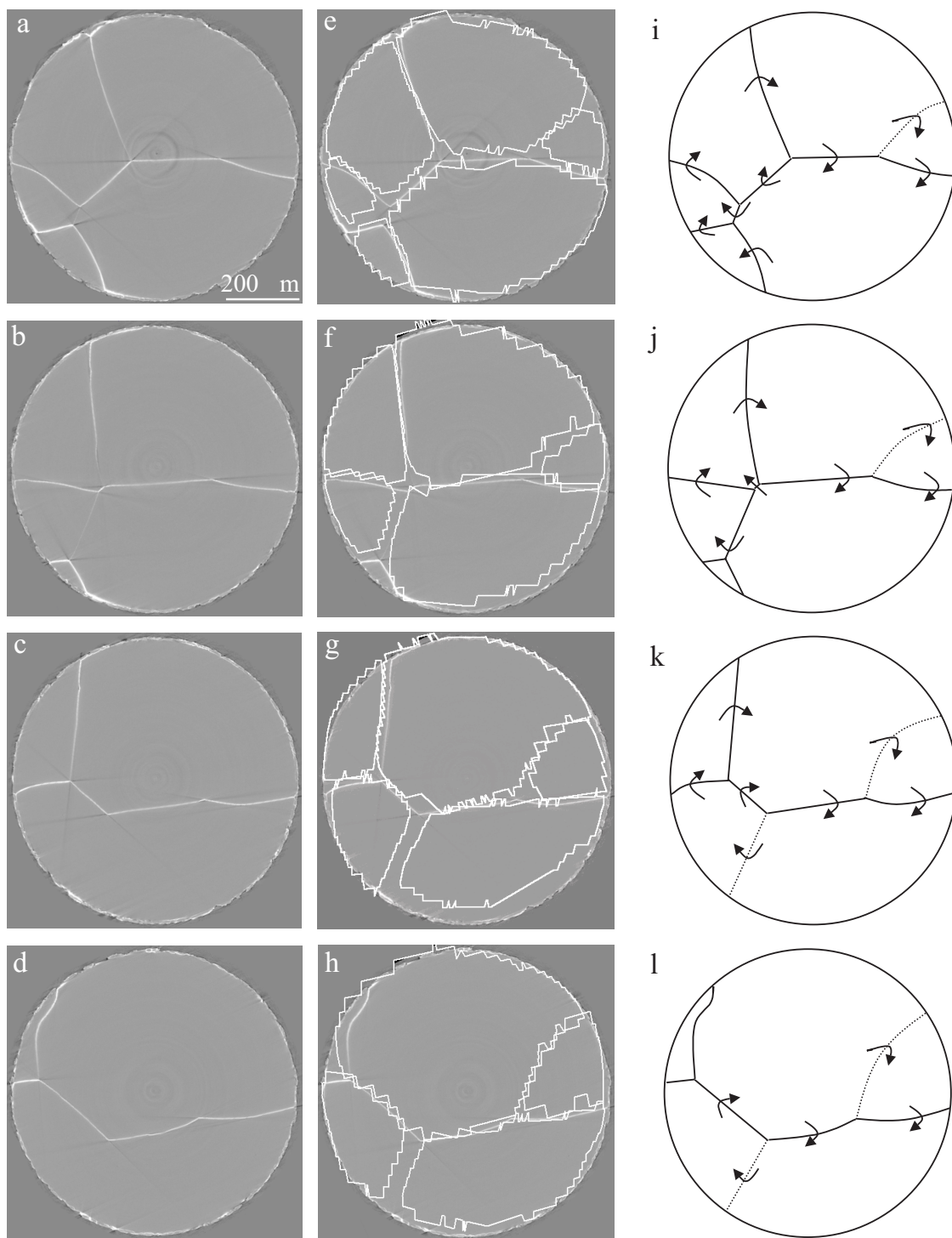


Figure 4.16: Comparison of X-ray tracking and microtomography. Images (a)-(d) are the tomographic reconstructions corresponding to the four slices depicted in Fig. 4.15. The superposition of both results is shown in the central column, (e)-(h). Images (i)-(l) show a schematic representation of the tracking data, including the angle of misorientation between adjacent grains. Dotted boundaries are those which have only been detected by the X-ray tracking technique.

by the tracking technique, one low and one high angle boundary. The low angle boundary maintains a misorientation of 3.7° and is not decorated with Ga in either section. The high angle boundary shows a slight change (0.4° in misorientation) and changes from the wetted to the not wetted state in the third section, see Fig. 4.16c). It is interesting to note that this change occurs approximately at that elevation, where the small grain in the bottom left corner of Fig. 4.16b disappears. There could be several explanations for this, for example changes of the grain boundary energy as a function of the misorientation angle or grain boundary plane inclination. Also the boundary may be wetted (in Fig. 4.16c), but with considerably less Ga.

4.6.3 Tomographic observations with industrial Al alloy

A series of tomographic observations were performed with a commercial aluminium alloy (Al 5083, composition in at. %: Si (0.15), Fe (0.19), Cu (0.04), Mn (0.56), Mg (4.1), Cr (0.12), Ti (0.02)). The extruded material was annealed at 700 K for 24 h, then at 800 K for another 24 h. Optical inspection after surface etching (10 % HF) clearly revealed a columnar structure with elongated grains (1-3 mm) of the material. In the plane perpendicular to the deformation direction, the grain size ranges from tens to hundreds of microns.

Cylindrical samples with a diameter of 0.8 mm were machined from the base material, with the cylinder axis parallel to the major axis of the elongated grains. Figure 4.17 shows three tomographic reconstructions at the same position in one of our samples. The first scan (Fig. 4.17 a) was taken before application of liquid metal and shows the initial state of the material. Random distributed iron rich inclusions, commonly observed in this type of material, give rise to the point like, white contrasts. Figure 4.17b shows the same section through the sample after wetting by liquid Ga and moderate annealing of 4 h at about 50°C . A network of line-shaped contrasts, corresponding to macroscopic gallium wetting layers has appeared. Figure 4.17c shows the effect of an additional annealing of two hours at 300°C . The contrast has changed: the formerly sharply defined lines have become more diffuse and inhomogeneous: white isolated Ga droplets and small (few μm) cavities (dark) can be detected. Note, that the same pattern of inclusions can be observed in the different reconstructions. This indicates that we are looking at identical virtual slices in the sample.

The careful investigation of the relative position of the inclusions before and after the application of Ga reveals again a displacement of the grains with respect to each other (Fig. 4.18) [LB00]. As expected, the particles belonging to the same grain do not change their relative position. However, the distance between particles from different grains has evolved. A small increase (δ), comparable to the thickness of the wetting layer at the grain boundary ($\gamma \cong 2 - 3 \mu\text{m}$) is detected. The additional annealing at 300°C did not induce significant further movement of the inclusions.

Comparison with EBSD mapping

In order to verify, if the contrasts correspond to the real grain structure of the material, we compared the tomographic reconstruction with an EBSD mapping (Electron Back-Scatter Pattern, also: *grain orientation imaging*) [Ada97, Sch97] recorded on the sample surface. This technique is based on the automatic analysis of the diffraction patterns (Kikuchi lines) of backscattered electrons in the electron microscope. It is restricted to the sample surface and requires a special surface preparation (mirror finish and electro-chemical polishing). The spatial resolution and the accuracy in the determination of the grain orientation are in the order of $1 \mu\text{m}$ and 1° respectively.

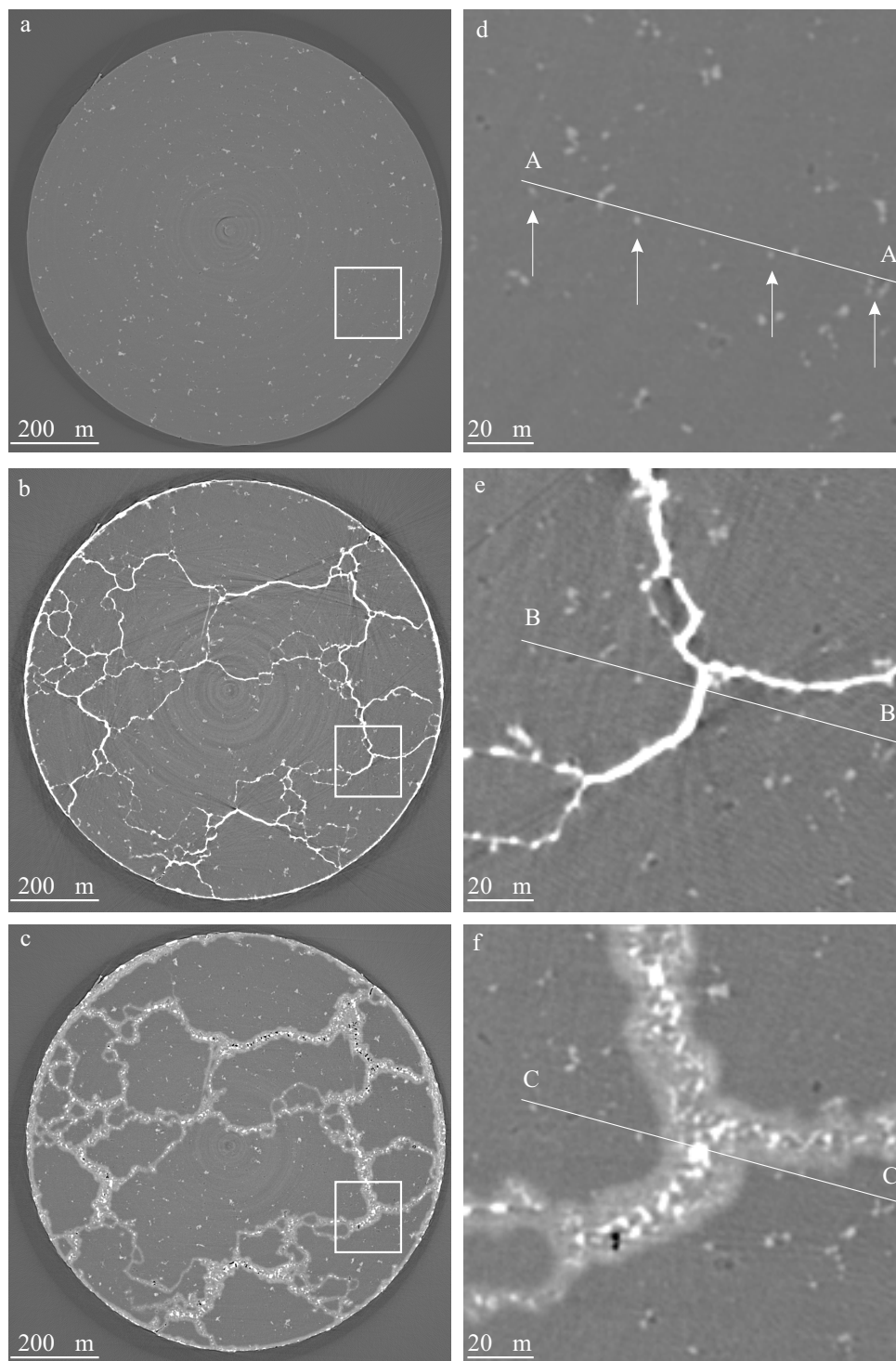


Figure 4.17: Tomographic slices perpendicular to the axis of the cylindrical sample (Al5083): (a) before application of Ga; (b) after application of Ga and an annealing of 4 h at 50 °C; (c) after 2 h of additional annealing at 300 °C. Pictures (d)-(f) correspond to the squared regions indicated in (a)-(c). The depicted slices correspond to exactly the same section in the sample, as can be seen from the identical distribution of small inclusions and porosities.

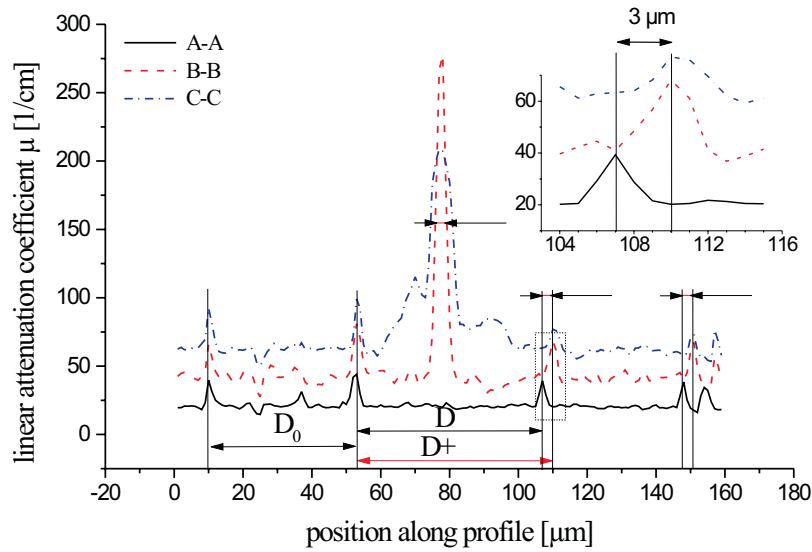


Figure 4.18: Plots of the linear attenuation coefficient along the lines A-A, B-B, C-C as indicated in Fig. 4.17. Whereas the relative position of inclusions (see arrows in Fig. 4.17d) belonging to the same grain does not change (D_0 is constant for the three profiles), the distance between particles separated by the grain boundary increases by $\delta \approx 3 \mu\text{m}$. The width of the grain boundary profile γ is comparable to δ . Profiles B-B and C-C are plotted with a vertical offset of 20 cm^{-1} and 40 cm^{-1} , respectively.

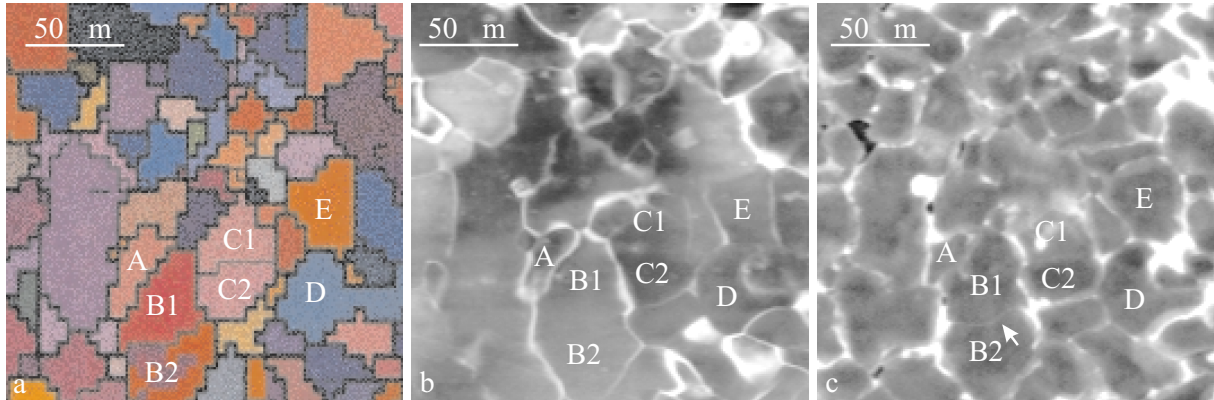


Figure 4.19: a) Grain structure at the surface of an Al5083 sample, as revealed by electron diffraction (EBSP). (b) Tomographic reconstruction close to the sample surface after application of liquid Ga and 30 min annealing at 50°C and (c) after additional annealing of 60min at 150°C

A sample of the same alloy (Al 5083, parallelepiped of $0.7 \times 0.7 \text{ mm}$ cross-section) was first characterized by EBSP, then wetted by gallium and characterized by microtomography. Figure 4.19a shows the grain structure as determined by electron diffraction. The zig-zag pattern is produced by the relative coarse spatial sampling rate ($5 \mu\text{m}$) of the electron beam. The accuracy in the determination of the shape of the individual grains is therefore limited by the sampling rate and not by the intrinsic resolution of the technique itself. The orientation information is

coded in the colour representation: similar colours indicate weak misorientation between grains.⁶

The sample was then wetted with liquid Ga and a first tomographic scan was performed after an initial anneal for 30 min at 50°C (Fig. 4.19b). Although the gallium was applied to the opposite side, the surface of interest was covered by a surplus of gallium which prevented close comparison: Fig. 4.19b is a virtual slice $\approx 5\mu\text{m}$ below the sample surface. The outline of large grains like the ones indicated by letters are well reproduced. Due to the slight displacement relative to the surface, the comparison works less well for small grains. Nevertheless, grains of sizes down to 10-20 μm can still be distinguished in the reconstruction and allow to give an estimate of the minimum detectable grain size.

A second tomographic scan (Fig. 4.19c) was performed after an additional anneal of 60 min at 150°C. As in the previous example (Fig. 4.17c), the annealing leads to a thickening of the contrast due to the diffusion of Ga into the adjacent grains. However, we observe in addition the appearance of new grain boundaries (e.g. the low angle boundaries B1-B2 and C1-C2), not visible after the first anneal at low temperatures. This might be the manifestation of a wetting transition (see Fig. 4.1) caused by the different temperature dependencies of the surface energies γ_{sl} and γ_{gb} . In-situ X-ray imaging experiments at elevated temperatures⁷ should allow to elucidate this point in more detail.

Concluding, we may state that the network of wetting layers, as revealed in tomographic reconstructions corresponds to the actual grain boundary structure in the material. Only a small fraction ($\lesssim 5\%$) of the total number of grain boundaries appears to be free of wetting layers (low energy grain boundaries) after a moderate annealing of 30 minutes at 50°C.

Influence of thermo-mechanical processing

Samples of the same alloy (Al5083, see § 4.6.3) were subject to different thermo-mechanical treatments in order to study the influence of parameters like the grain size and plastic deformation on the wetting behaviour of the material.

Thin plates (1.5 mm) of the extruded Al5083 alloy were cold-rolled to 70 % of their initial thickness and then annealed for 30 minutes at 370 °C. After this processing, which leads to recrystallization of the material, an average grain size in the order of 30 μm was observed by optical inspection after surface etching. Part of the recrystallized material was further subject to plastic deformation (3 % relative elongation) in a tensile stress rig. Cylindrical samples of $\cong 800\mu\text{m}$ diameter were then machined from the different materials. The samples were then wetted by liquid Ga and annealed for 30 min at 50 °C.

Figure 4.20 shows tomographic reconstructions of the material in its different microstructural states. The image of the extruded material (Fig 4.20a) shows the typical characteristics as already observed in Fig.4.17: a network of clearly delineated wetting layers of different widths (up to 3 μm) and randomly spread inclusions. Figure 4.20b shows the recrystallized (small-grained) material, wetted by liquid Ga. The wetting behaviour has completely changed: although the images are displayed with identical contrast, the liquid films are now only merely discernible and almost absent in the center of the sample. However, if liquid Ga is applied to the recrystallized *and* deformed material one can again observe the formation of relative thick (1-2 μm) wetting layers (Fig. 4.20c).

⁶e.g. grains B1-B2 and C1-C2

⁷A small furnace, compatible to the tomographic setup is currently under construction.

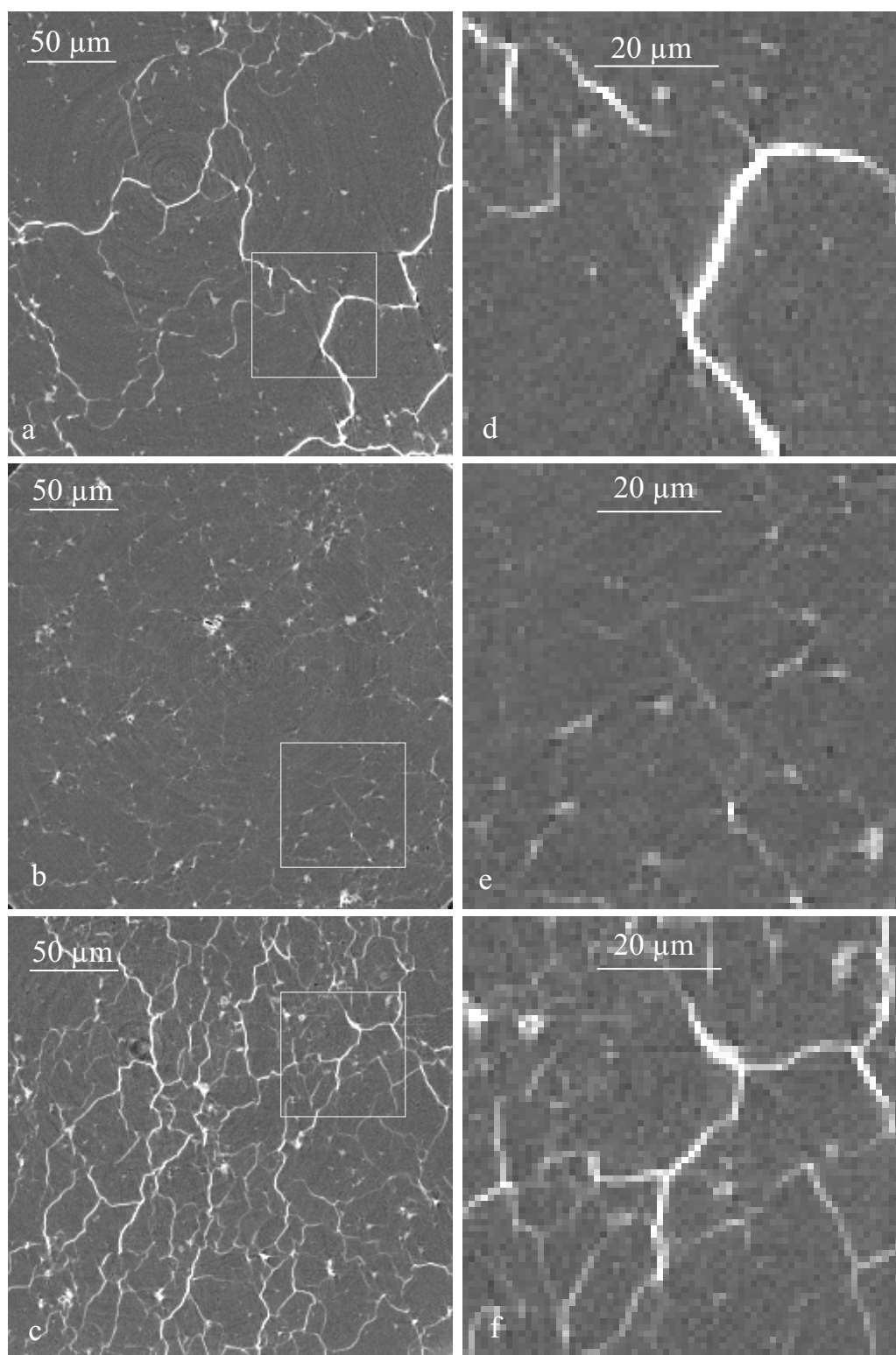


Figure 4.20: Tomographic reconstructions of Al alloy (Al5083), wetted by liquid Ga after different thermo-mechanical treatments: (a) Extruded material (c.f. Fig. 4.17), (b) small grained, recrystallized material : the wetting layers are merely discernible, (c) recrystallized and deformed (3 % elongation) material.

These observations compare well with the experimental finding, that parameters like the grain size and internal stresses have a strong influence on the susceptibility of certain metal couples to fail in intergranular brittle mode (LME) [NO79].

4.7 Discussion

4.7.1 Possibilities and limitations of X-ray micro-imaging

The use of SR X-ray micro-imaging techniques allowed us to observe the penetration of liquid Ga into the grain boundaries of Al polycrystals and bicrystals. It is to our knowledge the first time that this process could be observed *in-situ* and in the bulk of millimeter sized specimens. This constitutes an important progress compared to previously employed characterization methods which were either limited to ex-situ observations on polished or fractured specimens or restricted to thin foils, containing only a two-dimensional arrangement of grain boundaries.

The direct observation of GBW by X-ray imaging is not a new idea [Roq71] in itself. However, previous attempts were limited by the performance of available X-ray imaging systems. The advent of synchrotron radiation sources and ongoing progress in instrumentation have changed this situation in recent years: X-ray micro-imaging has developed into a quantitative imaging technique, combining micrometer spatial resolution with high temporal resolution (currently $\cong 100$ ms). We contributed to this development by the optimization of the high resolution detector system (§ 2.3.2) and the implementation of the large bandwidth multilayer monochromator (§ 2.2.2).

Before we proceed with the analysis and interpretation of our experimental observations, it will be instructive to estimate the detection limits of X-ray imaging in absorption mode.

Detection limits

The amount of Ga required to produce discernible absorption contrast depends on the X-ray energy, the acquisition geometry and on the achievable signal to noise ratio (SNR, see table 2.4). Highest sensitivity in the hard X-ray regime is obtained for energies slightly above the K-edge of Ga (10.4 keV, $\mu_{\text{Ga}} \approx 1330 \text{ cm}^{-1}$, Fig. 1.1). The logarithmic subtraction of images before and during the penetration process yields directly the values of $\mu_{\text{Ga}} t_{\text{Ga}}$ and hence the projected thickness t_p of the Ga layer.

A value of practical concern is the so-called 1 % thickness $t_{1\%}$, i.e. the thickness necessary to provoke 1 % absorption contrast.

$$\frac{I}{I_0} = 0.99 = \exp -\mu t_{1\%} \quad \Leftrightarrow \quad t_{1\%} \approx \frac{0.01}{\mu} \quad (4.2)$$

A rough estimate of the 1 % thickness can be obtained for the following two limiting cases:

1. The grain boundary is perpendicular to the X-ray beam: in this case the effective thickness t_p is equal to the thickness of the wetting layer t_l and $t_{1\%} = 0.01/\mu \approx 75 \text{ nm}$.
2. The grain boundary is parallel to the X-ray beam. In the idealized case of a perfectly flat boundary, $t_p = t_l/\sin \varphi = 75 \text{ nm}$ could be obtained for virtually any layer thickness t_l by selecting the angle φ between the GB and the X-ray beam small enough (see also Fig. 4.6). The finite resolution of the detector would be the limiting factor for $\varphi=0$. In

the latter case the 1 % thickness can be approximated by $t_l = r_d/100 \cong 10$ nm, where r_d is the spatial resolution of the detector ($\cong 1 \mu\text{m}$).

A similar estimate can also be obtained for the case of tomographic imaging. Under typical imaging conditions it is possible to distinguish 5% variations of the reconstructed values of the attenuation coefficient in the aluminium matrix. The width t of a Ga wetting layer which gives rise to a 5% change of the mean attenuation coefficient in the spatial resolution element ($\cong r_d^3$ with $r_d =$ resolution of the *tomographic* imaging system) is given by

$$\frac{t_{\text{Ga}}}{r_d}(\mu_{\text{Ga}} - \mu_{\text{Al}}) = 0.05\mu_{\text{Al}} \quad (4.3)$$

With $r_d \cong 2 \mu\text{m}$ and the values of μ at 10.4 keV, we obtain $t=4$ nm as the thickness of the Ga wetting layer which should still produce detectable contrast.

Note that in the case of thin wetting layers ($t_l < r_d$), the reconstructed values of the attenuation coefficient correspond to the mean attenuation coefficient averaged over the resolution element (partial volume effect, [KS88]). Moreover, the apparent width of the wetting layers, as observed in 2D tomographic reconstruction does not exactly correspond to the actual width of the layer: the inclination of the boundary with respect to the tomographic slice as well as the finite resolution of the detector system lead to a broadening of the actual width of the boundary.

Consequences

Recent TEM observations of GBW in the Al/Ga system [HH98] indicate, that during the first steps of penetration only monolayers of liquid Ga propagate along the grain boundaries. The above estimates of the detection limit indicate, that the observation of these first steps is out of reach in X-ray absorption imaging.

As a consequence, we measured not the propagation rate of the penetration front, but rather the displacement of the point where the thickness of the travelling film reaches the detection limit. However, the procedure used to determine the kinetics of the penetrating film (linear fits of the thickening profiles and extrapolation to the base line, Fig. 4.11) should be quite independent of the actual detection limit as long as the thickening profiles are adequately described by linear functions.

If there was a kind of precursor film (below the sensitivity limit) which spreads already before the onset of the macroscopic wetting process we may state, that the propagation rate of this precursor film can only be higher than the rate of the macroscopic wetting front.

We observed a linear displacement over a distance of $400 \mu\text{m}$. Under the assumption that GBW is a continuous, smooth process, it seems justified to infer the same linear kinetics for the penetration front itself. It is interesting to note, that the ratio of the thickening versus the propagation rate observed in our experiments is the same as the one reported in the TEM observations by Hugo [HH98].

4.7.2 Interpretation of the experimental results

The most important results of our experimental observations are recalled in in Fig. 4.21. We now address the question, in how far these observations can help to clarify the mechanism of grain boundary wetting in the Al/Ga system. Let us recall some of the open questions of GBW:

1. What is the destination of the Al from the groove root? Is it removed from the groove tip? If yes - where does it go and what is the mechanism of removal?
2. Why do we observe macroscopic wetting layers? The thermodynamic driving force (minimization of surface energies) should disappear after adsorption of a few monolayers.
3. What is the relation between the diffusion ahead of the penetration front and the macroscopic wetting process?

Destination of the solid material

The different models which have been proposed to explain the mechanisms of GBW (see appendix C) agree in a common point: the solid metal is removed by a fast diffusional mechanism from the groove tip.

However, a number of experimental observations are in contradiction to such a mechanism based on diffusional removal of Al:

1. The comparison of tomographic reconstructions before and after the penetration process reveals a displacement of the grains adjacent to a wetted grain boundary. The absolute values of the displacement are comparable to the width of the wetting layers. Diffusional removal through the liquid phase should not lead to such grain displacements.
2. In-situ radiography reveals that the grain displacement occurs *during* the penetration process and confirms the tomographic observations.
3. The temporal evolution of the wetting layer thickness shows pronounced discontinuities (except for the case of bicrystals). Diffusion processes should show a smooth temporal evolution.
4. The penetration process (without external stress) is accompanied by acoustic emission [KCKH94].

We shall note, that one of the models, proposed recently by Glickman et al. predicts in fact a swelling of the solid material during the penetration process ([GN99], see also appendix C.4). These authors consider the possibility of a stress driven diffusional drift of the solid material *ahead* of the advancing groove tip. Whereas this model reflects well the characteristic behaviour of metallic systems at elevated temperatures (e.g. Ni/Bi), it can not account for the rapid penetration of room temperature systems like Al/Ga and Zn/Ga. More precisely, the material flux along the grain boundary, necessary to evacuate the Al from the groove tip is far in excess of the theoretical estimates of the GB diffusion flux in Al.

We conclude, that the most plausible interpretation of our observations is the one of a liquid film intruding into an open *crack*. A possible mechanism which may lead to rapid propagation of the liquid phase is outlined in the next section.

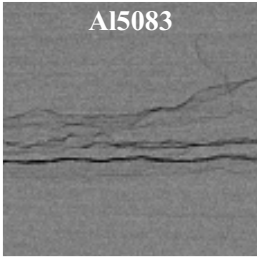
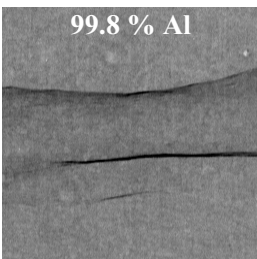
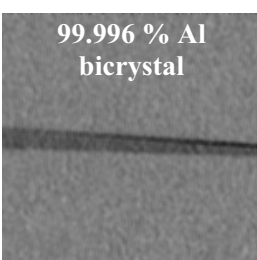
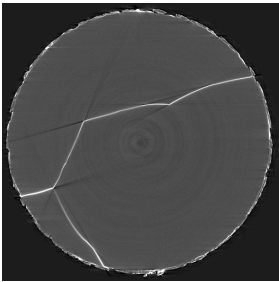
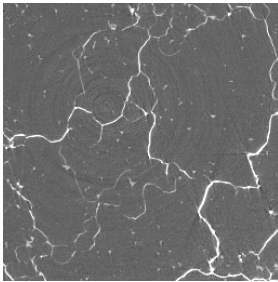
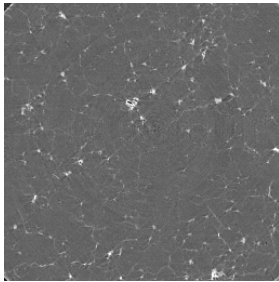
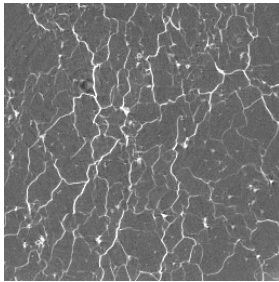
In-situ Radiography	dL/dt penetration rate	de/dt thickening rate	remarks
	discontinuous up to 170 $\mu\text{m/s}$ mean rate: 60 $\mu\text{m/s}$	not available	Al5083, extruded complicated microstructure prevents quantitative analysis discontinuous character of dL/dt
	mean rate: 25 $\mu\text{m/s}$ difficult to determine exactly	large dispersion: 0.003 - 5 nm/s	99.8 % Al polycrystal rather smooth time evolution with sudden discontinuities grain displacement
	~ linear propagation 1: 30 $\mu\text{m/s}$ 2: 10 $\mu\text{m/s}$	~ linear thickening 1: 1 nm/s 2: 0.7 nm/s	99.996 % Al bicrystals smooth time evolution some differences between two identical samples no penetration in (113) twin GB
Tomographic observations			
			
99.996 % Al polycryst. thick wetting layers grain displacement Tracking: some GB's are not wetted	A50831 (extruded) thick wetting layers grain displacement EBSP: some GB's are not wetted	Al5083 recrystallized only thin wetting layers similar results in small grained Al 1050 alloy	Al5083 recrystallized and deformed thick wetting layers

Figure 4.21: Summary of relevant experimental results.

4.7.3 A possible mechanism

Our experiments confirm the relevance of the spreading coefficient $S = \gamma_{gb} - 2\gamma_{sl}$ for the observed wetting phenomenon: no rapid penetration was observed in the case of low angle grain boundaries and the 113 twin boundary of the bicrystal. It is highly probable that the low energy of these boundaries yields a negative spreading coefficient and prevents the wetting transition in this case. Instead of rapid penetration a typical 'Mullins' groove is formed at the surface.

It turns out, that most of the grain boundaries in polycrystalline Al fulfill the wetting condition $S > 0$. In this case the local equilibrium at the groove root can no longer be maintained and the grain boundary will be replaced by the two solid-liquid interfaces of an intruding liquid film.

We found experimental evidence that the propagation of liquid Ga films is not controlled by diffusion but rather by a mechanism which involves the formation and propagation of intergranular cracks.

The formation and propagation of cracks requires a stress normal to the grain boundary. Under the assumption of a 'dynamic', non-zero dihedral angle [GN99], the non-equilibrated capillary forces do not only promote the diffusion of the liquid phase ahead of the groove tip (component F_{yy})[GN99] but create also a stress component σ_t perpendicular to the boundary plane.

We now have the necessary components to invoke the following intergranular brittle fracture mechanism (see also Fig. 4.22):

1. Atoms of the liquid phase diffuse along the grain boundary *ahead* of the groove tip. The adsorption of the diffusing atoms leads to progressive weakening of the grain boundaries resistance against brittle fracture.
2. The 'dynamic' dihedral angle leads to imbalanced capillary forces at the groove tip. The component F_{yy} accelerates the diffusion of Ga *ahead* of the groove tip. The perpendicular components σ_t of this imbalanced force are responsible for a tensile stress σ_t normal to the GB.
3. As soon as the extent of the weakened zone has reached a critical length l_{crit} , a crack opens over a distance L larger than the zone affected by Ga diffusion.

This mechanism allows to rationalize a number of experimental observations:

1. Abnormal high penetration rates of $>10\mu\text{m/s}$.

The kinetic mechanism of the advancing liquid film would be controlled by (i) the time necessary to weaken the grain boundary over a length l_{crit} (step 1) and (ii) the length L of the brittle crack extending along the grain boundary.

2. Displacement of grains during wetting and quasi-instantaneous thickening of the Ga layer all along the wetted part of the grain boundary.

The propagation of a crack over a distance L is connected with a displacement δ of the crack walls. Viscous liquid flow assures the quasi instantaneous filling of the enlarged groove [Gor78]. The liquid is drawn up into the groove and follows the advancing crack tip.

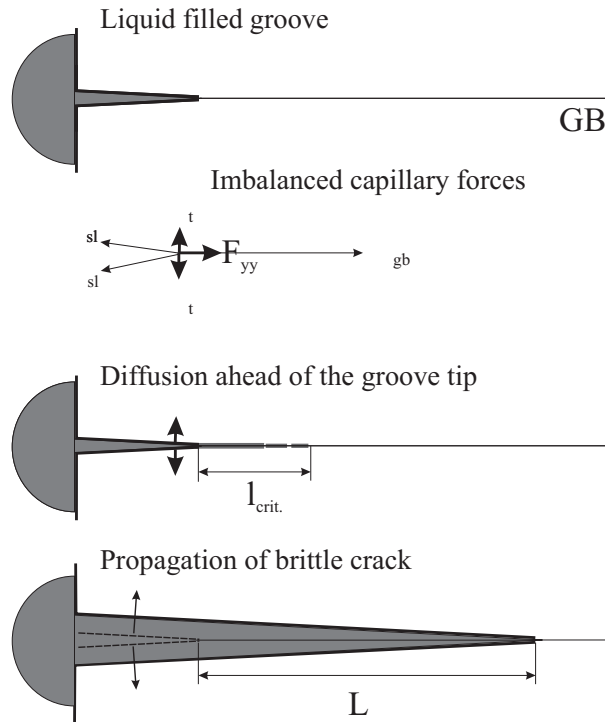


Figure 4.22: Proposed mechanism of rapid penetration of liquid films. Ga diffusion along the GB leads to progressive weakening of the GB. As soon as the diffusion zone has reached a critical value l_c a brittle crack propagates over a distance L , longer than l_{crit} .

3. Abrupt changes in the slope of the thickening curves. Such variations can be readily explained by the discontinuous propagation of cracks.
4. Acoustic emission (AE) during the penetration process. Again, the propagation of cracks can explain the origin of the AE signals.

Consequences

The observation, that penetration is accompanied by a grain displacement and the interpretation in terms of a crack propagation mechanism implies an important consequence:

The formation of macroscopic wetting layers is expected to depend strongly on external and internal mechanical constraints. If the lateral movement of the grains is restricted (like, e.g. in the center of a large sample) an intruding liquid film will cause an elastic stress. This stress tends to prevent the opening and propagation of cracks and consequently also the formation of macroscopic wetting layers.

Indeed, there is experimental evidence, that geometrical parameters like the grain size and the sample geometry play an important role. If we introduce the aspect ratio

$$\alpha = \frac{\text{grain diameter (d)}}{\text{sample diameter (L)}}$$

we can distinguish two limiting cases (Fig. 4.23)

$\alpha \ll 1$ The movement of small grains in the center of a large specimen is highly constrained. We observe no or only very thin wetting layers in this case (see Fig. 4.20).

$\alpha \cong 1$ In the case of bicrystals or large grained polycrystals the individual grains experience no or little constraints. Relative grain movements of up to several micrometers can be observed.

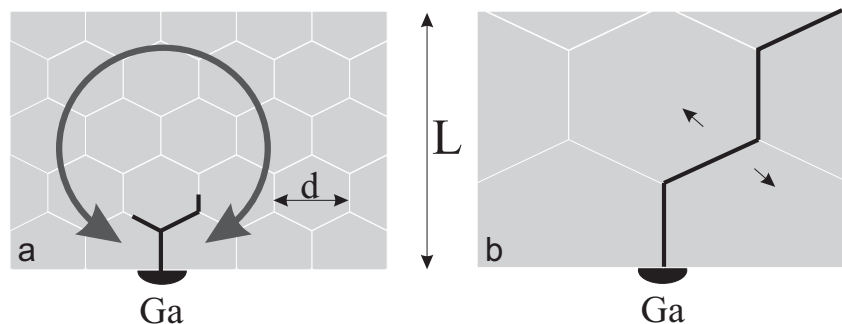


Figure 4.23: Influence of mechanical constraints on the macroscopic wetting behaviour. (a) in the case of small grained material, the movement of grains is highly confined and an intruding liquid film will cause a compressive stress which will prevent further crack dilation and opening. (b) In the case of large grained material the intruding liquid film can cause a grain displacement δ .

4.8 Conclusions

We applied and optimized X-ray micro-imaging techniques for the study of rapid penetration of liquid Ga into the grain boundaries of Al. For the first time it was possible to study the penetration process in-situ and in the bulk of millimeter sized Al specimens.

Measurements on Al polycrystals and bicrystals revealed that Ga spreads in form of a liquid film along the grain boundaries. Quantitative measurement of the penetration kinetics are restricted to bicrystals of perfect boundary geometry. In-situ observations on two identical bicrystal specimens revealed propagation rates of $10 \mu\text{m/s}$ and $30 \mu\text{m/s}$. The propagation along the boundary seems to obey linear kinetics.

The penetration is accompanied by a linear thickening of the liquid film which has an initial width below the resolution limit ($\cong 10 \text{ nm}$) of our technique. The thickening occurs along the whole length of the liquid film and has a typical rate of 10 \AA/s . A displacement of the grains in the direction normal to the grain boundary plane was observed *during* the wetting process. The absolute value of the displacement corresponds well to the thickness of the intruding liquid film.

This displacement suggests that the thickening of the liquid film does not occur via dissolution and removal of Al from the groove root. A plausible interpretation of our observations can be given in terms of intergranular fracture mechanism. There is experimental evidence, that the rapid penetration of macroscopic wetting layers is connected to the formation and propagation of intergranular cracks. Extension of the crack along the grain boundary leads to opening of the crack surfaces behind the advancing tip and accounts for the thickening of the wetting layers with time.

The absence of macroscopic wetting layers in the case of small grained material and discontinuities (quasi instantaneous changes of the layer thickness at points separated by several hundreds of micrometers) in the thickening rate which have been observed in the case of polycrystalline material can be understood in this framework. In the case of small grained polycrystalline material, mechanical constraints, imposed by the presence of neighbouring grains, seem to prevent the formation of macroscopic wetting layers.

We conclude this chapter by a list of worthwhile, future experiments which should help to elucidate further details of this intriguing phenomenon, which continues to withstand proper explanation for now more than 50 years.

Perspectives

Our observation technique did not provide the sensitivity required to reveal the existence of a (nanometric) precursor film ahead of the liquid filled groove. This precursor film is thought to promote the brittleness of the GB and deserves further experimental efforts in order to determine the extent and the kinetics of this part of the wetting film.

It should be possible to detect such a precursor film by using X-ray micro-fluorescence. The minimum detection limit of this technique depends on the atomic number, the footprint of the X-ray micro-spot and the escape depth of the characteristic radiation. Due to the fact, that the wetting layers extend in two dimensions, extremely low limits (sub-monolayer) are expected. The simultaneous detection of the fluorescence and absorption signal should allow to elucidate the relation between the nanometric and micrometric parts of the wetting film.

Still concerning the nanometric part of the wetting films, it would be interesting to verify, if these precursor films are still present in cases, where the formation of macroscopic wetting layers is suppressed by mechanical constraints. Micro-fluorescence tomography should allow to decide, if the grain boundaries in the bulk of small grained material are penetrated or not.

Further support for the hypothesis of the propagation of the macroscopic wetting layer by means of a crack propagation mechanism could be obtained from experiments combining direct radiographic observation of the wetting layers and the simultaneous detection of strain fields, i.e in-situ X-ray diffraction imaging (topography) during the penetration process. The formation and relaxation of long range strain fields near the groove tip should give rise to changes in the diffracted intensity. Moreover, the assumed propagation of an intergranular crack should lead to acoustic emission with distinct signal characteristics. First test experiments, performed at INSA Lyon were promising and a combination of in-situ radiographic imaging and AE measurements seems feasible. The coincidence of sudden changes in the layer thickness with strong AE signal would give strong support for the proposed mechanism.

Chapter 5

Grain boundary imaging

Our experiments with a polycrystalline aluminium alloy showed that the majority of the grain boundaries are wetted by liquid Gallium. This gives rise to the idea to use Ga as a selective contrast agent which allows to visualize the three-dimensional grain boundary structure in aluminium alloys. We demonstrate the potential of this technique for the study of the interaction of fatigue cracks with grain boundaries in cast aluminium alloys.

5.1 Motivation

The prediction of the fatigue life of engineering structures is an important issue in fracture mechanics. The usual approach to evaluate the fatigue life of cyclically loaded components and structures is based on the concepts of Linear Elastic Fracture Mechanics (LEFM) [BB97]. Within the framework of this theory it is possible to rationalize the fatigue behaviour of structures with different sizes. The key parameter governing the crack tip stress field and hence the propagation rate of fatigue cracks is called the elastic stress intensity factor range ΔK .

$$\Delta K = Y \Delta \sigma \sqrt{\pi a} \quad (5.1)$$

ΔK is a function of the applied stress range $\Delta \sigma$ (i.e. the difference between the maximum and minimum stress during a fatigue cycle) and increases as the square root of the crack length a . The proportionality factor Y depends on the geometry of the crack.

Provided that the elastic stress intensity factor is maintained, it is possible, thanks to LEFM, to evaluate the fatigue life of large structures by measurement of the fatigue crack growth rate in small laboratory samples. Fracture occurs, as soon as the length of the fatigue crack has reached a critical length (governed by the toughness of the material) and starts to propagate catastrophically.

It is now recognized, however, that LEFM cannot describe properly the behaviour of short cracks emanating from a smooth sample (i.e. without any surface defects which might act as stress concentrators) or from the root of a notch [Sur94]. As a result, the fatigue life of components calculated by LEFM and taking into account small initial defects is overestimated. This problem is of great practical concern and therefore it has attracted much attention in recent years.

The main differences observed experimentally between short and long cracks can be summarized as follows [BB97]:

- For a given ΔK short cracks propagate faster than long ones.
- Short cracks propagate for ΔK values below the macroscopic propagation threshold ΔK_{th} .
- The initial growth of short cracks can decrease or even stop for low stress levels.

Several explanations have been proposed for the short cracks behaviour:

- crack closure problems: i.e. the fact that during a fatigue cycle, a crack can close before reaching the minimum stress [Sur94].
- three dimensional effects: Cracks tend to reach an arc-shaped equilibrium configuration and the growth rate on the surface may be higher than the one in the bulk, see also Fig. 5.1. Such cracks often stop to grow after having reached the stable configuration [CAP84].
- interaction of the cracks with the microstructure (precipitates, twins, inclusions, grain boundaries) [Lan85].

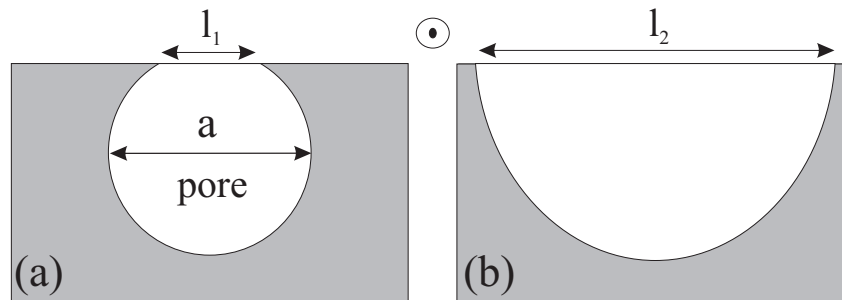


Figure 5.1: (a) Initial crack configuration. The rate of crack growth on the surface ($l_2 - l_1/\Delta t$) may be higher than the one in the bulk as the crack tends to reach an equilibrium shape (b). Short cracks often stop to propagate after having reached the stable arc-shaped configuration.

Experimentally, the mere observation of the material surface during cycling is a serious limitation for studying in detail the mechanisms of initiation and growth of short cracks. In fact, cracks may initiate from pores below the surface and it is impossible to monitor their growth by conventional observation methods. There have been some attempts to study the bulk behaviour of cracks by serial polishing [CAP84]. However this is a very tedious procedure not free from artifacts and hence of limited interest.

X-ray tomography turned out to be a valuable tool for studying short cracks in the bulk of a material. However visualizing fatigue cracks is not straightforward: the typical opening of cracks is in the order of $1 \mu\text{m}$ and smaller. Attempts to visualize these defects with laboratory X-ray scanners were not successful and revealed the need for a high-resolution tomographic set-up with $1 \mu\text{m}$ spatial resolution, currently only available at synchrotron sources.

In what follows we report on first experiments on a model cast aluminium alloy aimed at studying the interaction of short fatigue cracks with the microstructure using high-resolution X-ray tomography.

5.2 Fatigue properties of Al/Si cast alloy

The studied material is a model Al/Si cast alloy (AS7G0.3). This material can be easily processed for manufacturing objects with an intricate shape. However, because aluminium contracts when it solidifies, and also because hydrogen dissolves very easily in the molten metal, cast aluminium alloys always contain a certain amount of porosity when no special casting technique is used. This porosity is known to have a detrimental influence on the mechanical properties of the material, especially on its fatigue resistance. As a result, a lot of research has been carried out on the fatigue mechanisms in cast aluminium alloys in relation with porosity. A recent study has shown that the fatigue properties of such alloys at low stress levels are strongly correlated with the interactions of cracks with grain boundaries [Sav00].

The fatigue mechanisms of the studied alloy can be summarized as follows:

- The initiation of fatigue cracks always occur near a pore at the surface of the material or just below it. The number of cycles for the initiation is always negligible compared to the whole fatigue life.
- At high stress levels, once initiated, cracks propagate through the sample with no noticeable stop and the crack growth rate can be described through a Paris law [Sur94]

$$\frac{da}{dN} = C(\Delta K)^m \quad (5.2)$$

where da/dN denotes the crack propagation rate (a = crack length, N = number of cycles), ΔK the stress intensity factor and C and m are two material dependent constants.

- At low stress levels, short cracks are observed to stop at grain boundaries. This happens when the cracks are small (typically below 500 μm). For instance at 130 MPa the crack stopping at grain boundaries can account for nearly 90 % of the fatigue life.

The reason why cracks stop at grain boundaries is thought to be a reduction of the dislocation free zone at the tip of the crack induced by the presence of a neighbouring grain with a different crystallographic orientation [Cha97].

Thus, at low stress levels most of the fatigue life consists in the growth of short cracks which are often stopped at grain boundaries. At that stage the crack has a three dimensional configuration where it must increase its width and depth through several grains showing different crystallographic orientations. It is during this growing stage that the material exhibits its maximum resistance to fatigue. However, as already pointed out, several questions arise from the fact that such cracks are generally observed only at the sample surface:

- Is the crack blocked all along its length or is it stopped only at the surface while the rest of the crack continues to grow in the bulk ?
- Where does the process of overcoming the grain boundary start along the crack front ?
- Is there a relation between the grain crystallography and the crack path at the surface and in the bulk ?
- Is it possible to account for the crack stops observed in the middle of grains at the surface by some microstructural features below the surface ?

The answers to those questions are very important for the understanding of the alloy fatigue mechanisms and, from a more general point of view, of the behaviour of short cracks with respect to the microstructure. The ideal observation technique would be to characterize crack initiation and propagation in-situ and in three dimensions. Practically, this requires a fatigue machine which can be directly installed on the tomographic set-up (360 ° visibility) and which can be positioned in a reproducible way. Such a machine is currently under construction, but was not yet available for our experiments.

We followed an intermediate approach which consisted of the following procedure:

1. An interrupted dynamic fatigue test was performed at INSA, Lyon. The crack length was determined at the sample surface after a fixed number of cycles by optical microscopy. The fatigue experiment was stopped before final failure of the sample.
2. The grain structure in the region close to the surface intersection of the crack was determined by EBSP (INSA, Lyon).
3. The three-dimensional shape of the crack in the bulk of the sample was determined by micro-tomographic imaging (ESRF)
4. The sample was exposed to liquid Gallium and annealed for 1 h at 150°C. A second tomographic scan, revealing the grain boundary structure was recorded.

The experimental results presented in the following section are part of a collaboration with S. Savelli and J.Y. Buffière (INSA Lyon), who performed the fatigue test and surface characterizations. The three-dimensional visualization of the crack surface and the characterization of the grain structure in the bulk of the sample were performed by W. Ludwig, ESRF.

5.3 Experimental Results

5.3.1 Observations on the sample surface

Figure 5.2 summarizes the results of the crack propagation experiment. The optical micrograph on the left side shows the surface trace of a fatigue crack, which started at the porosity on the top of the scene. The dark points in this image are Si particles which are formed during solidification of the alloy. The second image is an EBSP mapping of the same zone and reveals the position of the grain boundaries. The crack, as well as the Silicon rich particles can not be indexed and appear as black points in the mapping. Note, that the Si particles are not only located at the grain boundaries, but also inside grains.¹ At point W, the crack changed from intergranular to transgranular propagation mode. For comparison we show also the tomographic reconstruction of the sample surface before and after application of Gallium (Fig. 5.2 c and d respectively).

The length of the crack was determined every 25000 cycles under a light microscope and is reported in Fig. 5.2 e. At points 'X' and 'Z' the crack was trapped for $\cong 50000$ and $\cong 25000$ cycles respectively at a grain boundary visible at the surface. The reason for the short arrest at point 'Y' remains unclear from surface observations.

¹more precisely, the Si particles inside the Al grains are located in the silicon rich eutectic Al phase between the dendrites of the primary Al

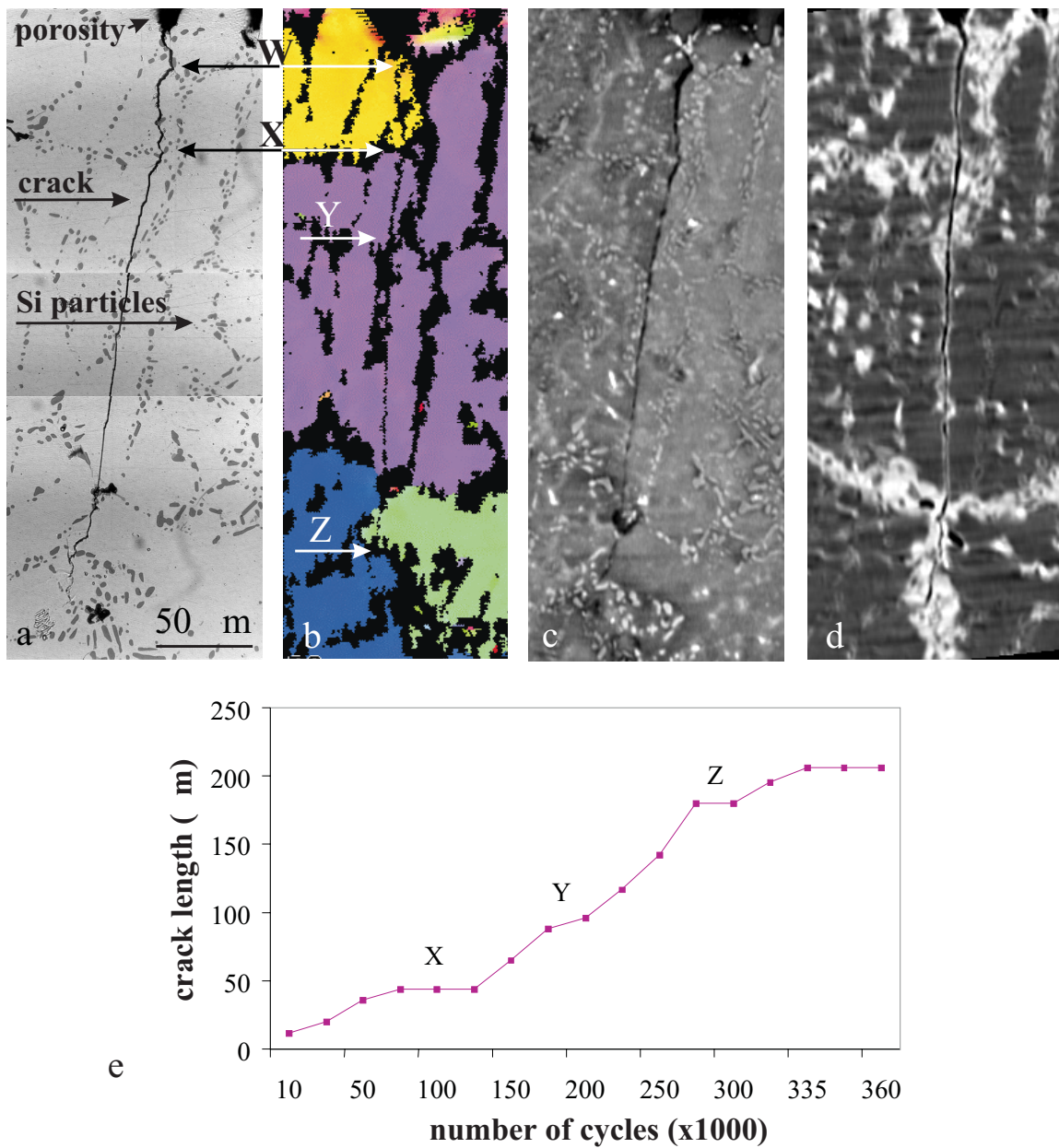


Figure 5.2: a) Optical micrograph of the fatigue crack at the sample surface b) EBSD mapping of the same zone c) tomographic reconstruction of the sample surface before application of Gallium d) tomographic reconstruction after application of Gallium e) plot of crack length versus number of cycles as observed by optical microscopy during the interrupted fatigue test.

5.3.2 3D analysis of the crack morphology

Figures 5.3 a and b show two tomographic slices perpendicular to the surface of crack observation (visible on the right border of image 5.3 a). These images suggest a complicated three-dimensional morphology of the crack surface. In addition to abrupt changes of the crack direction (Fig. 5.3 a) one observes branching and, apparently, unconnected crack segments (Fig. 5.3 b).

This complicated morphology requires a three-dimensional representation and analysis of the crack surface. The biphased structure of the material (aluminium matrix plus silicon rich parti-

cles) prevents the segmentation (i.e. the extraction of the voxels belonging to the crack surface) by means of simple threshold algorithms: both, the Si particles and the crack have lower gray values than the Al matrix² and would be extracted simultaneously. The selective extraction of the crack surface without the Si particles was performed by means of a morphological reconstruction (sequence of 3D morphological filter operations, [GM92]). The corresponding slices in the reconstructed, binary data set are shown in Fig. 5.3 c and d.

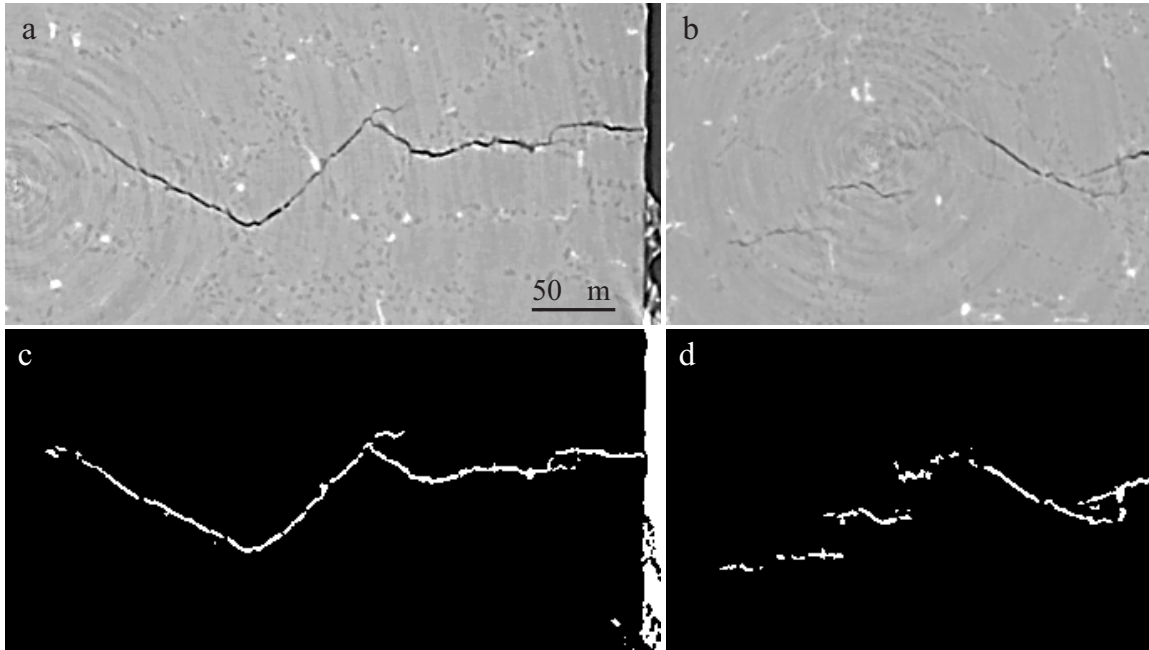


Figure 5.3: a,b): Tomographic slices perpendicular to the surface of observation (visible on the right border of the images on the left side) revealing the complicated topography of the crack in the bulk of the sample. c,d): corresponding slices after segmentation by morphologic reconstruction.

Figure 5.4 shows a volume rendering of the binary data set representing the crack. It turns out that the crack surface is connected and consists of three arc shaped segments (see also Fig. 5.6a). In the central segment the crack deviates abruptly by about 80 degrees from its mean direction (also seen in Fig. 5.3). The finger-like extensions in the right arc correspond to the crack fragments shown in Fig. 5.3 b.

5.3.3 Determination of the 3D grain structure

After the first tomographic scan the sample was exposed to liquid Gallium and annealed for one hour at 150 °C. After this treatment all grain boundaries are supposed to be wetted by liquid Gallium. The tomographic reconstruction in Figure 5.2 d validates our approach: the grain structure revealed by gallium is identical to the one determined by EBSP. Note however, that we are not restricted to the sample surface: the tomographic data contain the grain boundary structure of the whole sample. The inspection of tomographic slices in the bulk of the sample

²Si has a higher absorption coefficient than Al and one would expect the opposite contrast behaviour for Al and Si. The fact that we observe lower gray values for Si indicates that the sample to detector distance (8 mm) introduces already strong phase contrast. The apparent contrast inversion in Fig. 5.2c is an artifact due to the presence of the sample border (partial volume effect)

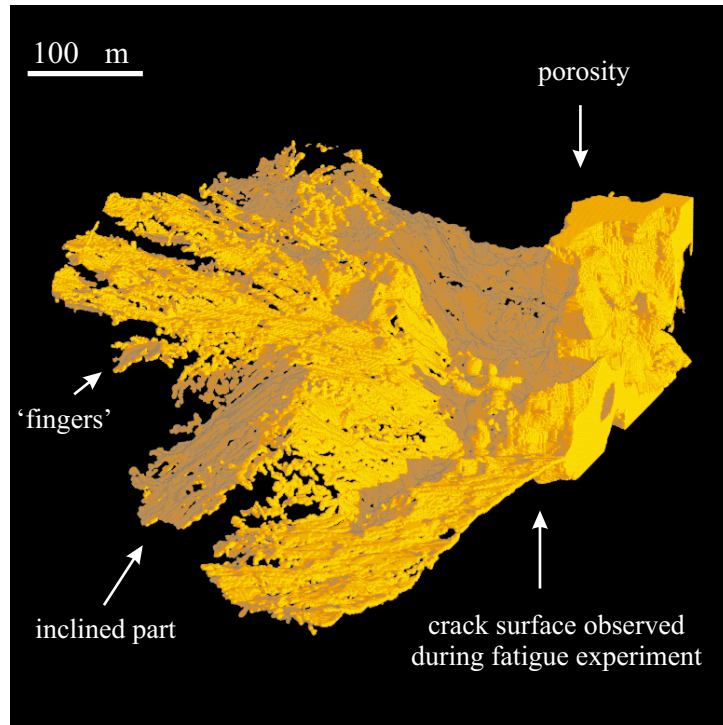


Figure 5.4: Three dimensional rendering of the crack surface. Note the abrupt change in inclination of the central arc-shaped crack segment. The finger-like crack extensions (see arrow) correspond to the crack fragments depicted in Fig. 5.3

(Fig. 5.5a) reveals an interesting finding: abrupt changes in the direction of the crack path like the ones observed in Fig. 5.4a are strongly correlated with the grain boundary structure.

In order to take full advantage of the three-dimensional information, we again have to perform a morphological segmentation of the data set. All voxels belonging to the same grain, i.e. to closed cells detected by the segmentation algorithm (3D watershed algorithm [GM92, Bou99]), were assigned identical labels (numbers). The result of this procedure is a new representation of the data set, well suited for three-dimensional visualization of the grain structure. Figure 5.5 illustrates the transition from the tomographic reconstruction to the segmented and labelled representation. The grain boundary structure in the segmented volume (Fig. 5.5b) is in good agreement with the tomographic raw data: all grains have been detected and only a few inaccuracies can be observed (e.g. the additional small grain in the lower part, arising from over-segmentation). Note, that the segmentation algorithm detects two distinct cells in cases where the crack has traversed a grain and divided it into two parts. Parts belonging to the same grain were attributed identical colours, but still exist as distinct cells (different numbers) in the numerical representation of the data set.

We finally merged both data sets: the one containing only the crack and the labelled one, containing the grains. We are now in the position to visualize the crack together with individual grains and to study the influence of the grain structure on the crack propagation in three dimensions. This turns out very useful, as demonstrated in Figure 5.6: the abrupt change of the crack inclination, already reported in Fig. 5.4 and 5.5 is clearly related to the transition into a new grain.

During the fatigue experiment a short crack arrest was observed at point 'Y' in Fig. 5.2 which seemed not to be related to the grain structure at the surface. The analysis of our data set

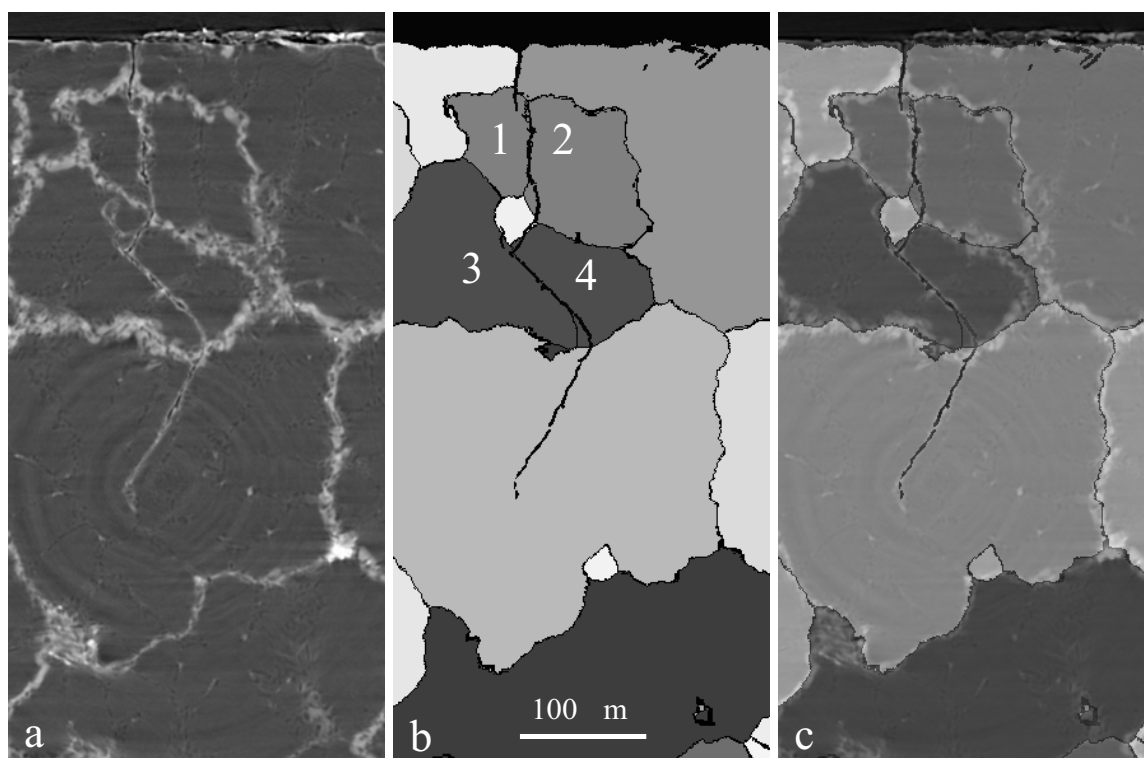


Figure 5.5: a) Tomographic reconstruction after application of Ga. The depicted slice corresponds to the same section shown in Fig. 5.4a. b) Result of 3D morphologic segmentation: each cell detected by the segmentation algorithm receives a distinct label, represented here by different colours. Cells belonging to the same grain (1&2 and 3&4) have been attributed identical colours. c) The superposition of the tomographic and the segmented data set shows a good agreement between both representations.

reveals another interesting finding: up to point 'Y', the purple grain (see Fig. 5.2 b extends only a few microns (10-20 μm) below the sample surface. The point 'Y' corresponds finally to the position, where the yellow grain disappears. This is illustrated in more detail in Fig. 5.7 a where the surface grain structure is visualized in three-dimensions. Only part of the purple grain is depicted in this figure: the right surface of the purple grain is actually one of the crack surfaces. The second part of this grain is set transparent in order to reveal the hidden structure of the yellow grain. The grains have been assigned the same colours like in the EBSP mapping (Fig. 5.7b).

5.4 Discussion

To the best of our knowledge, it is the first time that a simultaneous 3D image of a fatigue crack and of the surrounding crystal grains has been obtained. Although it is not possible to go back to the chronology of the crack growth in the bulk of the sample because of the procedure used, a number of important information can nevertheless be obtained from this kind of experiments.

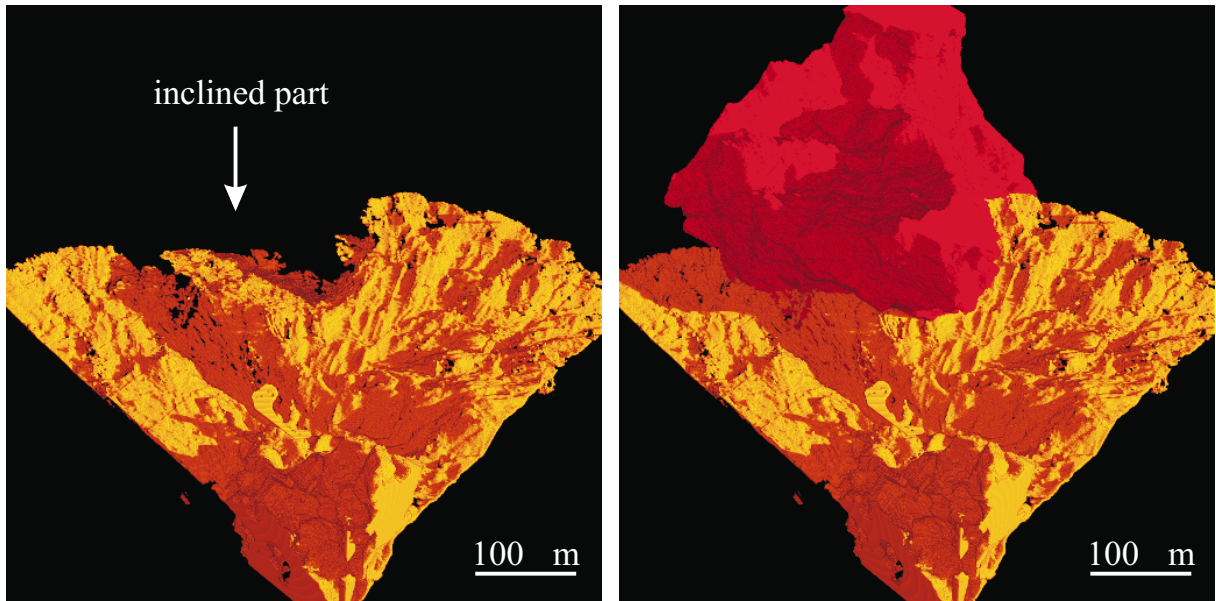


Figure 5.6: The abrupt deviation in the crack propagation direction coincides with the transition into a new grain. a) Volume rendering of the crack surface as in Fig. 5.3 but from a different viewpoint. b) Rendering of the crack surface and the grain that caused the sudden inclination.

Influence of grain orientation on crack propagation

It appears that the three-dimensional shape of the crack is strongly influenced by the different crystallographic orientations of the grains (see Fig. 5.6). In ductile solids, when the crack and the zone of plastic deformation surrounding the crack tip are confined to within a few grain diameters, crack growth occurs predominantly by single shear in the direction of the primary slip system ($\{111\}\langle 110\rangle$ for fcc metals). The effective shear stress τ acting on these systems can be calculated from the knowledge of the crystallographic orientation of the grain with respect to the axis of the applied tensile stress: $\tau = c\sigma$. The proportionality factor c is known as 'Schmidt factor' and results from the geometric projection of the applied stress on the active plane of dislocation glide [Sur94].

The assumption of a crack following crystallographic planes could be partly checked at the sample surface by extracting from the EBSD data the local Schmidt factors and the orientations of the most highly activated planes with respect to the crack path. This work is currently being carried out. A more complete approach would consist in a three-dimensional crystallographic characterization of the sample by means of the X-ray-tracking technique, presented in § 4.6.2. In the latter case it would be possible to determine the Schmidt factors also in the bulk of the sample.

The analysis of the strongly inclined part of the crack surface allows another interesting observation: the passage of the fatigue crack into the red grain shown on Fig. 5.6 occurs between points A and A' (Fig. 5.9), but not along the remaining part of the intersection between the crack and the grain boundary. A possible explanation of the preferential 'attack' along A-A' might be given in terms of a continuity condition for the crack surface, outlined below.

When the crack is small, its transition into a new grain of different orientation requires the adaptation to the new orientation of the most favourable crystallographic plane. This requires in general two types of rotations which we will call tilt and twist (see. Fig. 5.8). There is

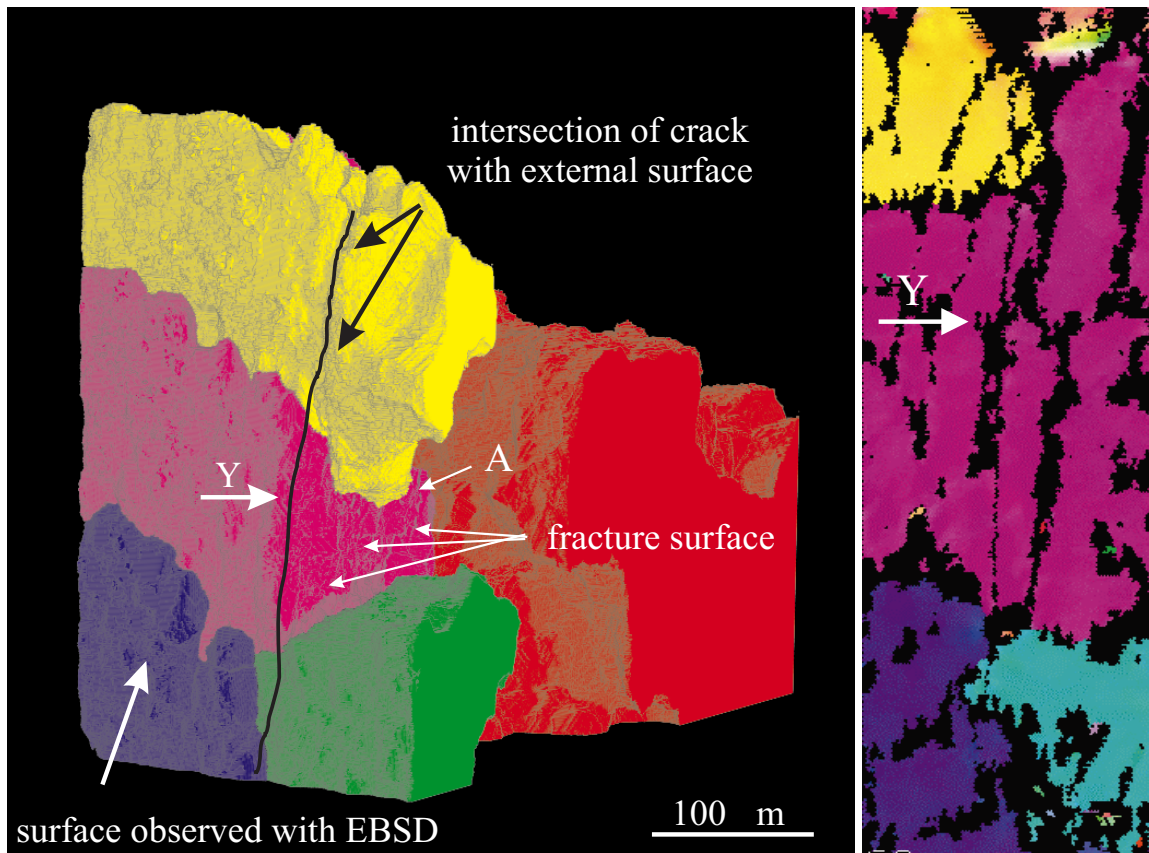


Figure 5.7: a) Volume rendering of the grain structure in the fractured region. The crack traversed the yellow and purple grain in transgranular mode. The second half of the purple grain is set transparent. b) EBSP mapping of the sample surface (cf. Fig. 5.2b).

experimental evidence, that the propagation by tilt is the preferred one in Al/Li alloy, [ZWM00b, ZWM00a]. This might be explained by the following 'hand-waving' argument: tilting allows for continuity of the crack surface, whereas twisting implies the creation of additional surfaces (the yellow ones in Fig. 5.8) and is consequently less favorable from an energetic point of view.

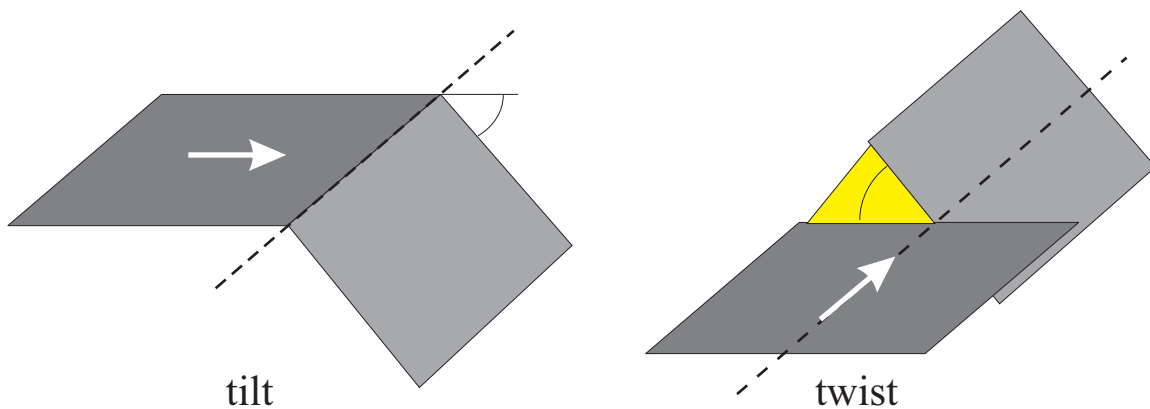


Figure 5.8: The adaptation of a crack to a new plane may involve tilting and twisting. Note that twisting requires the creation of additional surfaces (yellow) in order to preserve the connectivity of the crack surface.

Our observation seems to confirm this model: the crack enters the red grain between points A and A' because it can proceed by tilting, however it tends to follow the grain boundary and does not penetrate into the grain between points A' and A'' as this would require twisting of the crack plane (see Fig. 5.9). The analysis of a large number of fatigue cracks, including the crystallographic characterization of the adjacent grains will be necessary to corroborate the validity of the outlined mechanism. However, it seems likely that the twisting of the crack plane represents a serious limiting factor for the propagation of small cracks in the investigated material.

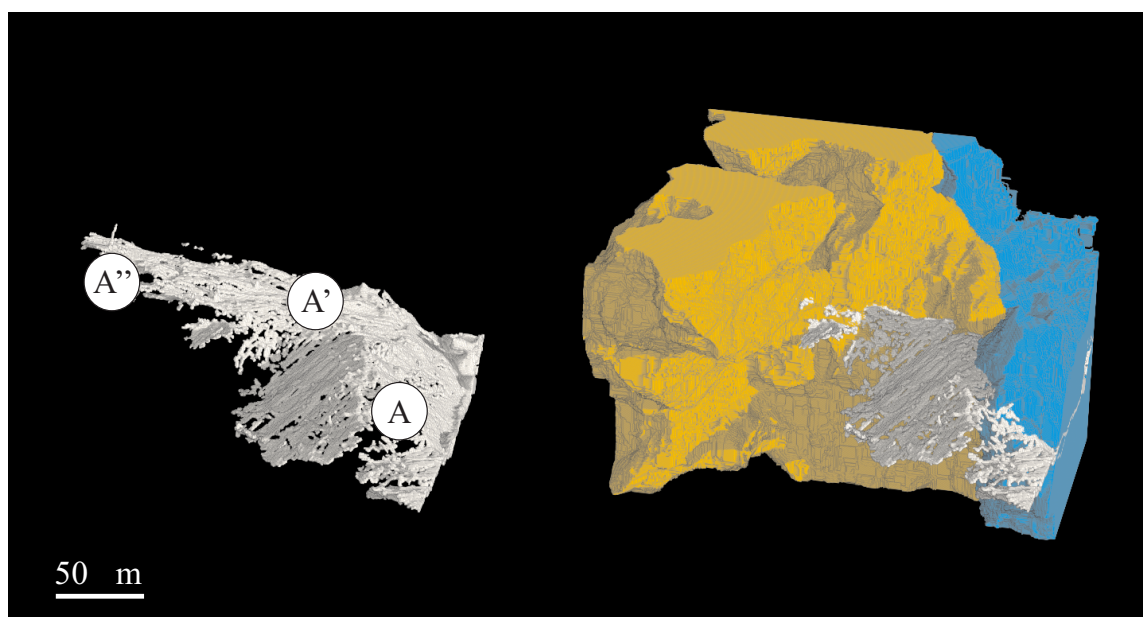


Figure 5.9: a) 3D rendering of the crack inside the 'red' grain (set to transparent). b) same scene with the surrounding grains. The crack entered the new grain between points A and A' by tilting. Between points A' and A'' the crack followed the contour of the grain. It is likely that the preferential attack along A-A' is governed by compatibility with favorable crystallographic orientations inside the grain.

Origin of crack stops

It was experimentally confirmed that the crack stops at points 'X' and 'Z' are related to the crossing of the surface grain boundaries. It might therefore be expected, that the passage of grain boundaries in the bulk of the sample will lead to comparable (local) crack stops.

Indeed, the 3D analysis of the grain structure below the surface (Fig. 5.10) allows to explain the crack stop observed in the middle of the purple grain at the sample surface (point Y, see also Fig. 5.2 and 5.7). We already concluded that it is likely that this stop corresponds to the crossing of the sub surface grain boundary between the yellow and the purple grains, i.e. the pinning of the crack front at point 'A' prevents the extension of the crack on the sample surface.

In spite of numerous studies published in the literature reporting evidences of crack stops (or decelerations) at grain boundaries, the mechanism(s) through which a crack can overcome such microstructural barriers remains unclear. Many authors agree however on the fact that it

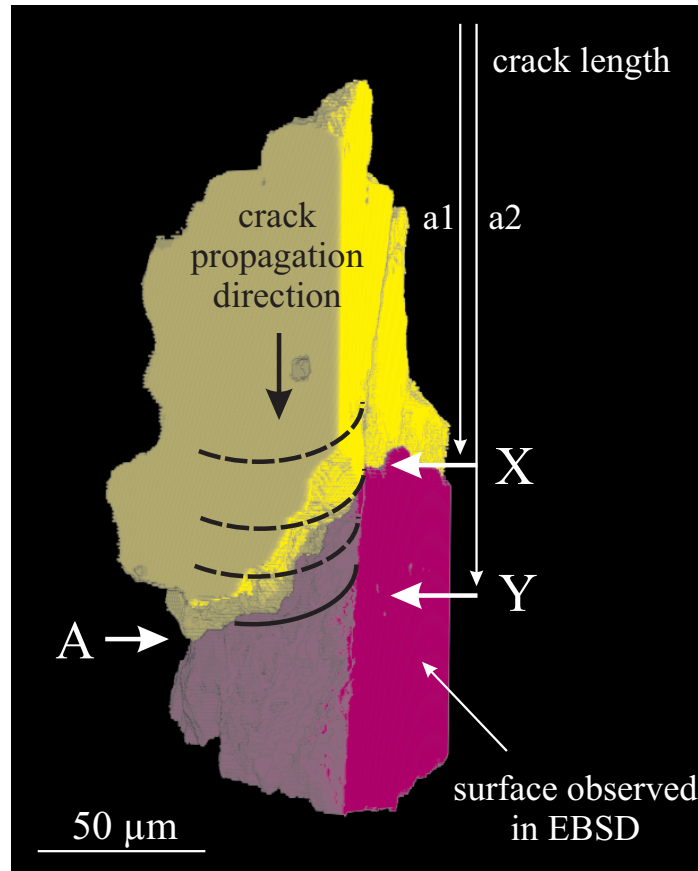


Figure 5.10: Crack stops were observed at points X and Y. Both stops can be attributed to the pinning of the crack front at the grain boundary between the yellow and purple grain.

is necessary that some plasticity should be initiated in the neighbouring grain for the crack to overcome the obstacle.

For the material studied here, a dislocation based mechanism has been proposed recently [Sav00] to evaluate the number of fatigue cycles necessary for a crack to overcome a grain boundary. This mechanism is schematically illustrated on Fig. 5.11. It can be summarized as follows: A crack is considered stopped at a grain boundary (a). The application of the cyclic fatigue stress leads to the activation of (at least) one dislocation source (S) in the neighbouring grain (b). For every fatigue cycle this source is thought to emit dislocations. Because of slip irreversibility, a fraction f^* of those dislocations will be stored in the material nearby the activated source (c). When the elastic energy W_{el} corresponding to those stored dislocations is high enough to compensate the formation of fresh crack surfaces ($W_{el} = 2\gamma_s$ where γ_s is the surface energy of the material), a new small crack can be created in the neighbouring grain (d). The blocked crack can join the new one and the propagation can go on until the next grain boundary (e). When the crack gets longer than 2 or 3 times the grain size its propagation is no more hindered by the presence of grain boundaries³ and its growth rate becomes comparable to that of long cracks.

With this mechanism it is possible to calculate the number of fatigue cycles N_B necessary to overcome the grain boundary between grains of known misorientation.

³This is due to the fact, that the stress intensity factor increases with the crack length, whereas the impeding action of microstructural features is constant

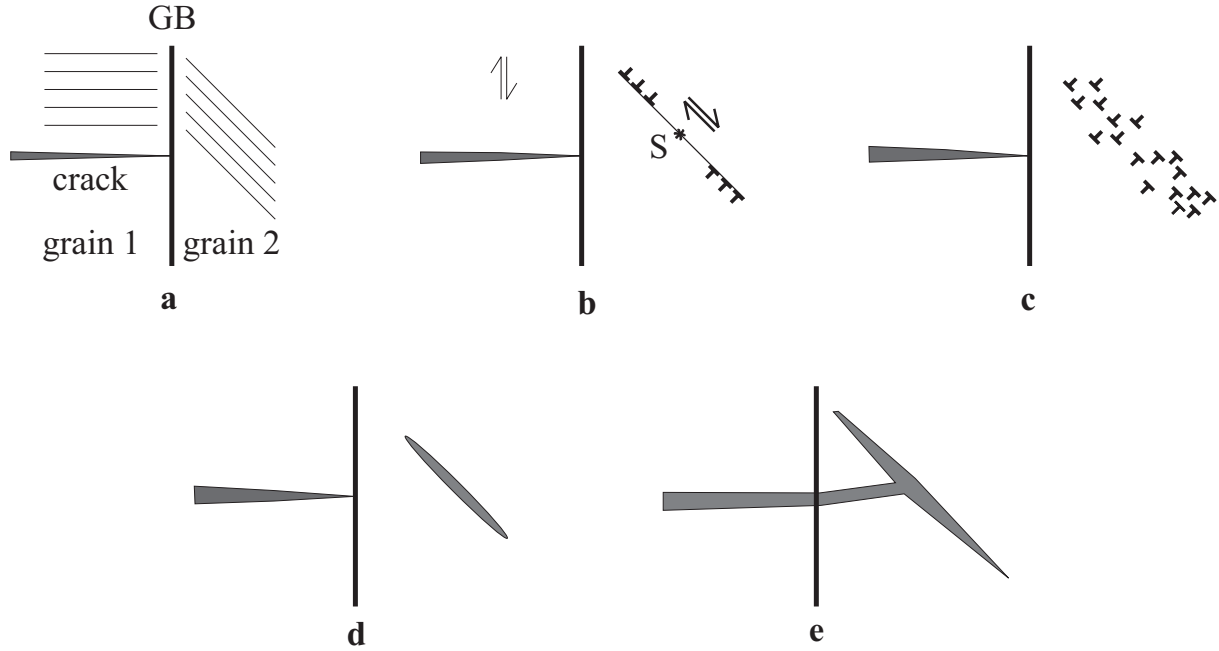


Figure 5.11: Schematic illustration of the dislocation based 'unlocking' mechanism of a crack which has been blocked at a grain boundary [Sav00].

As a matter of fact, the number of cycles N_B can be expressed as a function of the crack stress intensity factor K and of a crystallographic dimensionless factor ξ taking into account the crystallographic misorientation between the grains:

$$N_B = C\xi K^{-\beta} \quad (5.3)$$

where C and β are two empiric constants ($C=1.65 \cdot 10^7$ and $\beta \cong 7$ for the studied alloy [Sav00]).

Using this formula it is possible to calculate the number of cycles during which the crack is blocked at the yellow/purple grain boundary *at the surface* (point 'X', N_{Bs}) and *in the bulk* (point 'Y', N_{Bb}). Note that the crystallographic misorientation is the same in both cases. However, the stress intensity factor (equ. 5.1) is higher at point 'Y', due to the different length a_i of the crack (distance between the surface and the crack tip). Putting in real numbers, the model predicts crack arrests of $N_{Bs}= 50\,000$ and $N_{Bb}= 22\,000$ cycles. Those two values are in good agreement with the experimental numbers of cycles: $\cong 50\,000$ and $\cong 20\,000$ cycles respectively (see Fig. 5.2 e).

5.5 Conclusion

We demonstrated the possibility to visualize the three-dimensional grain structure of millimeter-sized aluminium polycrystals by means of the Gallium decoration technique. An adequate numeric representation of the grain structure was obtained by three-dimensional morphologic segmentation of the tomographic dataset.

This technique was applied to the study of the interaction of a fatigue crack with the grain structure in a cast aluminium alloy. The analysis of the three-dimensional crack shape with respect to the surrounding grain structure revealed clear evidence for the mutual interaction: the crack propagation direction is strongly influenced by the orientation of the most favourable planes

for dislocation glide. There is also evidence that transgranular propagation starts and proceeds from regions on the grain circumference where the crack surface can preserve its continuity. However, this point needs further investigation by in-situ observations during the fatigue test.

Future experiments should therefore include repeated tomographic characterization of the crack surface during interrupted fatigue tests, in order to monitor the crack extension in-situ and in the bulk of the sample. At the end of this test, the grain boundaries are wetted by Ga in order to obtain the precise spatial arrangement of the grains close to the crack. Combined with a determination of the grain *orientation* by the X-ray tracking technique, this type of experiments will allow to analyse the propagation of fatigue cracks as well as their interaction with microstructural features with unprecedented wealth of information.

Conclusion

The advent of modern third generation synchrotron sources has entailed considerable and on-going progress in the large spectrum of X-ray characterization techniques like X-ray crystallography, absorption spectrometry, diffractometry and X-ray imaging.

Concerning X-ray imaging, this progress may be roughly divided into two categories: (i) the enhancement of well established X-ray imaging techniques like diffraction imaging, absorption radiography and computed tomography in terms of sensitivity, spatial and temporal resolution and (ii) the development of an easily implementable form of X-ray phase contrast imaging, based on the propagation and interference of the partially coherent radiation delivered by modern synchrotron sources. Our contributions to these developments were presented in the first part of this work (*Methods and Instrumentation*).

The second part (*Applications*) was devoted to the application of X-ray micro-imaging to two particular problems in materials science: the wetting of aluminium grain boundaries by liquid gallium and the characterization of short fatigue cracks in cast aluminium alloy. X-ray micro-imaging allowed us in both cases to extract information which would otherwise have been inaccessible by conventional characterization techniques.

Methods and Instrumentation

In chapter 1 (Imaging) we presented a short introduction to the concepts of two-dimensional and three-dimensional X-ray imaging. Special emphasis was given to the description of the image formation process in the Fresnel approximation, taking into account the (partial) coherence of the incident radiation and the finite response of the two-dimensional detector system.

In chapter 2 (Instrumentation) we discussed the choice and the characteristics of the main components of the micro-imaging set-up, i.e. the monochromator, the high-resolution detector system and the mechanical set-up. The large bandwidth of synthetical metal-B₄C multilayer monochromators (compared to the conventional Si(111) double crystal arrangement) allowed us to reduce single exposure times in high-resolution imaging experiments ($\leq 1 \mu\text{m}$ pixelsize) from several tens of seconds to fractions of a second. This opened the way for the routine use of the high-resolution set-up in time-critical applications like tomography and in-situ radiography. The replacement of the YAG:Ce converter screens with optimized LAG:Eu screens lead to a significant improvement of the imaging performances of the high resolution detector system. Using the common technique to determine the different transfer functions (LSF, MTF) via measurements of edge (slit) profiles, we obtained a spatial resolution of $1 \mu\text{m}$ (fwhm of LSF) for the case of the optimized set-up with $0.4 \mu\text{m}$ pixelsize. In order to preserve this ultimate resolution, the mechanical set-up has to meet new, stringent requirements concerning precision and stability. These requirements were taken into account during the redesign of the tomographic instrument.

In chapter 3 (Methods) we compared and demonstrated different methods of qualitative and quantitative X-ray imaging. Image contrast under weak defocus conditions is connected to the (2D) Laplacian of the refractive index distribution and gives rise to a trivial form of phase contrast imaging ('edge enhancement') which is well suited to reveal the presence of inhomogeneities like internal interfaces, inclusions, cracks... in the bulk of the sample. By combining images recorded at different distances from the object, it is possible to retrieve the X-ray phase shift by a method similar to the focus variation technique in high-resolution transmission electron microscopy. The reconstructed phase maps can be interpreted as projections of the refractive index decrement and open the way for quantitative three-dimensional imaging (*holotomography*).

We further demonstrated the possibility to combine diffraction topography and tomographic imaging. This gives rise to a new imaging technique, (*topo-tomography*), which applies to perfect single crystals. We demonstrated the feasibility of this technique with the example of a synthetic diamond crystal where we were able to visualize the three-dimensional arrangement of individual dislocations in the bulk of the crystal.

Applications

The potential of X-ray micro-imaging for the direct observation of grain boundary wetting was demonstrated for the case of the metallic system Al/Ga (chapter 4). The wetting of Al grain boundaries occurs by a rapid (several tens of $\mu\text{m/s}$) process, involving initially only small quantities of liquid metal (nanometric liquid films). In-situ radiographic observations during the spreading process revealed that the thickness of the liquid films grows over the whole length of the wetted part and that the neighboring grains are pushed apart by distances corresponding to the film thickness. This grain movement was confirmed by comparison of tomographic reconstructions before and after the wetting process in polycrystalline material. The independent determination of the grain boundary structure by the X-ray tracking technique (3D) and electron diffraction (EBSP) revealed the existence of a small percentage of not-wetted grain boundaries. These boundaries could be identified as low-angle grain boundaries. The observation of discontinuous propagation and thickening rates in polycrystalline material suggests the existence of some kind of threshold mechanism, involving the nucleation and propagation of a brittle intergranular cracks. Such a mechanism implies a strong influence of geometrical sample parameters (grain size, confinement) in the case of polycrystalline material and might account for the peculiar behaviour of room temperature systems like Al/Ga and Zn/Ga.

In chapter 5 (Grain boundary imaging) we finally presented an application of the wetting phenomenon: the formation of microscopic Ga layers can be used to visualize the three-dimensional grain boundary structure in the bulk of polycrystalline Al alloys. This technique allowed us to perform a detailed (post-mortem) analysis of the interaction of a short fatigue crack with the grain structure in the *bulk* of a cast Al alloy. Our observations are in agreement with the results of previous work, rationalizing the propagation behaviour of such cracks.

Perspectives

In this work we tried to demonstrate the interest and the current possibilities of Synchrotron Radiation X-ray micro-imaging with the help of selected examples in the field of materials science. It is clear that we may apply these techniques also to other fields and in particular to life sciences. Hard X-ray phase contrast imaging (*holotomography*) is ideally suited for the study of weakly absorbing, biological samples. Unlike in electron or soft-X-ray microscopy, the

samples can be imaged in their natural, wet state and with considerably higher contrast and lower dose compared to conventional absorption imaging. The spatial resolution of $1\ \mu\text{m}$ seems well adapted for the analysis of the cellular structure of plants. Such work is currently in progress and showed encouraging perspectives.

Future experiments in materials science will strongly benefit from the development of additional sample environment (furnace, tension rig, cold cell,...). The *in-situ* observation of dynamic processes under the control of external parameters like temperature or tensile stress will considerably increase the spectrum of possible applications in this field.

With respect to the examples presented in this work, such additional equipment will for instance allow to extend the in-situ observation of wetting and embrittlement processes to systems like Ni-Bi and Fe-Pb which are currently intensively investigated due their relevance for applications in nuclear industry. Additional insight into the mechanisms of grain boundary wetting and in particular about the role of precursor films might further be expected from X-ray micro-fluorescence measurements.

A continuation of our work on fatigue crack propagation in Al alloys is planed for the near future: a dynamic fatigue module, compatible to the tomographic set-up is currently under construction and will open the way for *in-situ* observations of crack growth in the bulk of the sample. In combination with the X-ray tracking technique, these observations will allow to complete our analysis of fatigue cracks with the information about the crack propagation history and the Schmidt factors in the bulk of the material.

The 'topo-tomography' technique might find a practical application in the non-destructive characterization of natural diamond, prior to any cutting or polishing of the crystals. Moreover, the same principle (diffraction contrast) should allow to determine the shape of individual grains in a polycrystalline material and might e.g. be used for *in-situ* observations of grain growth in the *bulk* of metals. First attempts to perform time-resolved, *three-dimensional* imaging experiments revealed the possibility to reduce the overall acquisition time for a tomographic scan ($2\ \mu\text{m}$ pixelsize) to less than 2 minutes - a time scale which would also be sufficient to observe other dynamic processes and phase transformations in the bulk of opaque materials.

Bibliography

- [Ada97] B. L. Adams. Orientation imaging microscopy: Emerging and future applications. *Ultramicroscopy*, 67:11–17, 1997.
- [AJ86] M. F. Ashby and R. H. Jones. *Engineering materials 1. An introduction to their properties and applications*. Pergamon Press, 1986.
- [BB97] C. Bathias and J. P. Baille. *La fatigue des matériaux et des structures*. Hermes, Paris, 2nd edition, 1997.
- [BBBG97] F. Beckmann, U. Bonse, F. Busch, and O. Günnewig. X-ray microtomography (μ CT) using phase contrast for the investigation of organic matter. *J. Computer Assist. Tomography*, 21:539, 1997.
- [BDC96] M. Op de Beeck, D. Van Dyck, and W. Coene. Wave function reconstruction in HRTEM: the parabola method. *Ultramicroscopy*, 64:167–183, 1996.
- [BDZ93] J. Baruchel, A. Draperi, and F. Zontone. *J. Phys. D: Appl. Phys.*, 26:9, 1993.
- [Bec98] F. Beckmann. *Entwicklung, Aufbau und Anwendung eines Verfahrens der Phasenkontrast-Mikrotomographie mit Röntgen-Synchrotronstrahlung*. PhD thesis, University of Dortmund, Germany, 1998.
- [BH65] U. Bonse and M. Hart. An X-ray interferometer. *Appl. Phys. Lett.*, 6:155–156, 1965.
- [BIB96] V. A. Bushuev, V. N. Ingal, and E. A. Belyaevskaya. *Kristallografiya*, 41:808, 1996.
- [BKA95] B. S. Bokstein, L. M. Klinger, and I. V. Apikhtina. Liquid grooving at grain boundaries. *Mater. Sci. Eng. A*, 203:373–376, 1995.
- [Bou99] S. Bouchet. *Segmentation et quantification d'images tridimensionnelles*. Rapport de stage, ESRF, 1999.
- [BW99] M. Born and E. Wolf. *Principles of Optics, 7th ed.* Pergamon Press, Oxford, New York, 1999.
- [Cah77] J. W. Cahn. Critical point wetting. *J. Chem. Phys.*, 66:3667–3672, 1977.
- [CAP84] P. Clement, J. P. Angeli, and A. Pineau. Short crack behaviour in nodular cast iron. *Fatigue Engng. Mater. Struct.*, 7(4):251–265, 1984.
- [CBB⁺96] P. Cloetens, R. Barrett, J. Baruchel, J. P. Guigay, and M. Schlenker. Phase objects in synchrotron radiation hard X-ray imaging. *J. Phys. D: Appl. Phys.*, 29:133–146, 1996.

- [CG92] D. R. Clarke and M. L. Gee. *Materials Interfaces*, page 255. Chapman & Hall, London, 1992.
- [CGM⁺97] P. Cloetens, J. P. Guigay, C. de Martino, J. Baruchel, and M. Schlenker. Fractional Talbot imaging of phase gratings with hard X-rays. *Optics Letters*, 22:1059–1061, 1997.
- [Cha97] F. Champiot-Bayard. *Etude et modélisation de la propagation des fissures de fatigue de roulement amorcées en sous-couche dans l'acier M50 (80 Mo Cr V42)*. PhD thesis, INSA, Lyon, France, 1997.
- [CJBD92] W. Coene, G. Janssen, M. Op de Beeck, and D. Van Dyck. Phase retrieval through focus variation for ultra-resolution in field-emission transmission electron microscopy. *Phys. Rev. Lett.*, 69:3743–3746, 1992.
- [CLB⁺99] P. Cloetens, W. Ludwig, J. Baruchel, D. Van Dyck, J. Van Landuyt, J. P. Guigay, and M. Schlenker. Holotomography: Quantitative phase tomography with micrometer resolution using hard synchrotron radiation x rays. *Appl. Phys. Lett.*, 75:2912–2914, 1999.
- [CLD⁺99] P. Cloetens, W. Ludwig, D. Van Dyck, J. P. Guigay, M. Schlenker, and J. Baruchel. Quantitative phase tomography by holographic reconstruction. In U. Bonse, editor, *Developments in X-Ray Tomography II, SPIE Proc.*, volume 3772, pages 279–290, 1999.
- [Clo99] P. Cloetens. *Contribution to Phase Contrast Imaging, Reconstruction and Tomography with Hard Synchrotron Radiation: Principles, Implementation and Applications*. PhD thesis, Vrije Universiteit Brussel, Belgium, 1999.
- [Cor63] A. M. Cormack. Representation of a Function by its Line Integrals with Some Radiological Applications. *J. Appl. Phys.*, 34(9):2722–2727, 1963.
- [CPSB⁺97] P. Cloetens, M. Pateyron-Salomé, J. Y. Buffière, G. Peix, J. Baruchel, F. Peyrin, and M. Schlenker. Observation of microstructure and damage in materials by phase sensitive radiography and tomography. *J. Appl. Phys.*, 81:5878–5886, 1997.
- [CRS⁺99] L.S. Chang, E. Rabkin, B. Straumal, B. Baretzky, and W. Gust. Thermodynamic aspects of the grain boundary segregation in Cu(Bi) alloys. *Acta Mater.*, 47:4041–4046, 1999.
- [Des97] P. J. Desre. A mechanism for the stress independent grain boundary penetration of a metal by a liquid metal. Application to the metallic couple Al-Ga. *Scripta Mater.*, 37:875–881, 1997.
- [DiF99] High-efficiency multilevel zone plates for keV X-rays. *Nature*, 401:895–898, 1999.
- [ECB⁺98] J. Espeso, P. Cloetens, J. Baruchel, J. Härtwig, T. Mairs, J. C. Biasci, G. Marot, M. Salomé, and M. Schlenker. Conserving the coherence and uniformity of third-generation synchrotron radiation beams, the case of ID19, a ‘long’ beamline at the ESRF. *J. Synchrotron Rad.*, 5:1243–1249, 1998.

- [EMW00] W.J. Eaton, G.R. Morrison, and N.R. Waltham. Configured detector system for stxm imaging. In W. Meyer-Ilse, T. Warwick, and D. Attwood, editors, *AIP Conference Proceedings 507*, pages 452–456. Melville, New York, 2000.
- [FCJ94] M. G. Fernandes, R. E. Clegg, and D. R. H. Jones. Failure by liquid metal induced embrittlement. *Eng. Failure Analysis*, 1:51–63, 1994.
- [FDK84] L. A. Feldkamp, L. C. Davis, and J. W. Kress. Practical cone-beam algorithm. *J. Opt. Soc. Am.*, 1:612–619, 1984.
- [FGZ80] E. Förster, K. Goetz, and P. Zaumseil. Double crystal diffractometry for the characterization of targets for laser fusion experiments. *Kristall und Technik*, 1:937–945, 1980.
- [FJ97] M. G. Fernandes and D. R. H. Jones. Mechanisms of liquid metal induced embrittlement. *Int. Mat. Rev*, 5:251–261, 1997.
- [Fra94] V. E. Fradkov. Rapid liquid metal corrosion along grain boundaries. *Scripta Metall. Mater.*, 30:1599–1603, 1994.
- [GA82] P. Gordon and H. An. The mechanisms of crack initiation and crack propagation in metal-induced embrittlement of metals. *Metall. Trans. A*, 13A:457–472, 1982.
- [GE91] W. Graeff and K. Engelke. *Microradiography and Microtomography*, volume 4, pages 361–405. Elsevier Science, 1991.
- [Gli00] E. Glickman. Mechanisms of liquid metal embrittlement by simple experiments: from atomistics to life-time. In *Multiscale Phenomena in Plasticity*. Kluwer Academic Publishers, 2000.
- [GM92] C. Gratin and F. Meyer. Mathematical morphology in three dimensions. *Acta Stereologica*, 11 Suppl. I:551–558, 1992.
- [GN99] E. E. Glickman and M. Nathan. On the kinetic mechanism of grain boundary wetting in metals. *J. Appl. Phys.*, 85:3185–3191, 1999.
- [Gor78] P. Gordon. *Metall. Trans. A*, 9A:267, 1978.
- [GRS⁺99] T. E. Gureyev, C. Raven, A. Snigirev, I. Snigireva, and S. W. Wilkins. Hard X-ray quantitative non-interferometric phase-contrast microscopy. *J. Phys. D*, 32:563–567, 1999.
- [Gui71] J. P. Guigay. *Opt. Acta*, 18:677, 1971.
- [Gui77] J. P. Guigay. Fourier transform analysis of Fresnel diffraction patterns and in-line holograms. *Optik*, 49:121–125, 1977.
- [Hec98] E. Hecht. *Optics, 3rd ed.* Addison-Wesley, 1998.
- [Her80] G. T. Herman. *Image Reconstruction from Projections*. Academic Press, New York, 1980.
- [HH98] R. C. Hugo and R. G. Hoagland. In-situ observation of aluminium embrittlement by liquid gallium. *Scripta Materialia*, 38:523–529, 1998.

- [HH99] R. C. Hugo and R. G. Hoagland. Gallium penetration of aluminum: In-situ tem observations at the penetration front. *Scripta Mater.*, 41:1341–1346, 1999.
- [HH00] R. C. Hugo and R. G. Hoagland. The kinetics of gallium penetration into aluminum grain boundaries - in situ tem observations and atomistic models. *Acta Mater.*, 48:1949–1957, 2000.
- [Hig99] ESRF Highlights 1999. pages 112–113. ESRF Information office, 1999.
- [Hop55] H. H. Hopkins. *Proc. Roy. Soc. A*, 231:91, 1955.
- [Hou72] G. M. Hounsfield. *A method and apparatus for examination of a body by radiation such as X or Gamma*. Patent office, Pat.Spec. 1283915, London, 1972.
- [JBA99] B. Joseph, F. Barbier, and M. Aucouturier. Mechanism of liquid Bi penetration along Cu grain boundaries. *Scripta Mater.*, 42:1151–1158, 1999.
- [JPB99] B. Joseph, M. Picat, and F. Barbier. Liquid metal embrittlement: A state-of-the-art appraisal. *Eur. Phys. J. Appl. Phys.*, 5:19–31, 1999.
- [KCKH94] Y. Kodama, P. K. Choi, H. Koizumi, and S. Hyodo. Acoustic emission associated with the fracture of Al and Al alloy embrittled by liquid gallium. *Mat. Sci. Eng. A*, 176:231–235, 1994.
- [KG89] I. Kaur and W. Gust. *Handbook of grain and interphase boundary diffusion data*. Ziegler Press, Stuttgart, 1989.
- [Kir84] E. J. Kirkland. Improved high resolution image processing in bright field electron micrographs. *Ultramicroscopy*, 15:151–172, 1984.
- [KPH⁺99] A. Koch, F. Peyrin, P. Heurtier, B. Ferrand, B. Chambaz, W. Ludwig, and M. Couchaud. X-ray camera for computed microtomography of biological samples with micrometer resolution using $\text{Lu}_3\text{Al}_5\text{O}_{12}$ and $\text{Y}_3\text{Al}_5\text{O}_{12}$ scintillators. volume 3659, pages 170–178, 1999.
- [KRSS98] A. Koch, C. Raven, P. Spanne, and A. Snigirev. X-ray imaging with submicrometer resolution employing transparent luminescent screens. *J. Opt. Soc. Am. A*, 15:1940–1951, 1998.
- [KS88] A. C. Kak and M. Slaney. *Principles of Computerized Tomographic Imaging*. IEEE Press, New York, 1988.
- [Lan80] A. R. Lang. pages 170–185. Plenum Press, New York, 1980.
- [Lan85] J. Lankford. The influence of microstructure on the growth of small fatigue cracks. *Fatigue Engng. Mater. Struct.*, 8(2):161–175, 1985.
- [LB00] W. Ludwig and D. Bellet. Penetration of liquid gallium into the grain boundaries of aluminium: A synchrotron radiation microtomographic investigation. *Mater. Sci. Eng. A*, 281:198–203, 2000.
- [LSBM96] J. C. Labiche, J. Segura-Puchades, D. Van Brussel, and J. P. Moy. FRELON camera: Fast REadout LOw Noise. *ESRF Newsletter*, 25:41–43, 1996.

- [LSH⁺98] U. Lienert, C. Schulze, V. Honkimaki, T. Tschentscher, S. Garbe, O. Hignette, A. Horsewell, M. Lingham, H. F. Poulsen, N. B. Thomsen, and E. Ziegler. Focusing optics for high-energy X-ray diffraction. *J. Synch. Rad.*, 5:226–231, 1998.
- [LSR⁺99] B. Lengeler, C. Schroer, M. Richwin, J. Tuemmler, M. Drakopoulos, A. Snigirev, and I. Snigireva. A microscope for hard X-rays based on parabolic compound refractive lenses. *Appl. Phys. Lett.*, 74:3924–3926, 1999.
- [LST⁺99] B. Lengeler, C. Schroer, J. Tuemmler, B. Benner, M. Richwin, A. Snigirev, I. Snigireva, and M. Drakopoulos. Imaging by parabolic refractive lenses in the hard X-ray range. *J. Synch. Rad.*, 6:1153–1167, 1999.
- [Mar76] S. K. Marya. *Influence de la pénétration du Gallium sur les propriétés mécaniques de l'aluminium écroui. Etude de la structure et de la superplasticité à 50° C.* PhD thesis, Université de Paris-Sud, Centre d'Orsay, 1976.
- [MCG⁺95] D. A. Molodov, U. Czubyko, G. Gottstein, L. S. Shvindlerman, B. Straumal, and W. Gust. Acceleration of grain boundary motion in Al by small additions of Ga. *Phil. Mag. Lett.*, 72:361–368, 1995.
- [Mic86] A. G. Michette. *Optical systems for soft X-rays.* Plenum Press, 1986.
- [Mom95] A. Momose. Demonstration of phase-contrast X-ray computed tomography using an X-ray interferometer. *Nucl. Inst. Meth. A*, 352:622–628, 1995.
- [Mon76] L. F. Mondolfo. *Aluminium Alloys: Structure and Properties.* Butterworths, London, 1976.
- [MROM97] C. Medrano, P. Rejmánková, M. Ohler, and I. Matsouli. *Il Nouvo Cimento*, 19D:195–203, 1997.
- [Mul57] W. W. Mullins. Theory of thermal grooving. *J. Appl. Phys.*, 28:333–339, 1957.
- [Mul60] W. W. Mullins. *Trans. metall. Soc. A.I.M.E.*, 218:354, 1960.
- [Nat86] F. Natterer. *The mathematics of computerized tomography.* John Wiley sons, New York, 1986.
- [NO79] M. G. Nicholas and C. F. Old. Review liquid metal embrittlement. *J. Mater. Sci.*, 14:1–18, 1979.
- [NRS⁺91] O. I. Noskovich, E. Rabkin, V. Semenov, B. Straumal, and L. S. Shvindlerman. Wetting and premelting phase transitions in 38°[100] tilt grain boundary in (Fe-12at.%Si)-Zn alloy in the vicinity of the A₂-B₂ bulk ordering in Fe-12at.%Si alloy. *Acta Metall. Mater.*, 39:3091–3098, 1991.
- [OST⁺00] M. Ohler, M. Sanchez del Rio, A. Tuffanelli, M. Gambaccini, A. Taibi, A. Fantini, and G. Pareschi. X-ray topographic determination of the granular structure in a graphite mosaic crystal: a three-dimensional reconstruction. *J. Appl. Cryst.*, 33:1023–1030, 2000.
- [OT79] C. F. Old and P. Trevena. Liquid metal embrittlement of aluminum single crystals by gallium. *Met. Sci.*, 13:591–596, 1979.

- [PA91] S. D. Peteves and R. Abbaschian. Growth kinetics of solid-liquid Ga interfaces: Part i. experimental. *Metall. Trans. A*, 22A:1259–1286, 1991.
- [PNL⁺] H. F. Poulsen, S. F. Nielsen, E. M. Lauridsen, U. Lienert, R. M. Suter, and D. Juul Jensen. *Submitted*.
- [PRAW72] L. Peeters, C. Roques-Carmes, M. Aucouturier, and G. Wyon. Fragilisation intergranulaire de l'aluminium par le gallium liquide et application à l'examen microstructural de divers faciès intergranulaires de l'aluminium et de ses alliages. *Mém. Sci. Rev. Mét.*, 69:81–95, 1972.
- [Rab98] E. Rabkin. Coherency strain energy as a driving force for liquid grooving at grain boundaries. *Scripta Mater.*, 39:685–690, 1998.
- [Rad17] J. Radon. über die bestimmung von Funktionen durch ihre integralwerte längs gewisser Mannigfaltigkeiten. *Ber. Verh. Sächs. Akad. Wiss. Leipzig, Math-Nat.*, 69:262–277, 1917.
- [RAL70] C. Roques-Carmes, M. Aucouturier, and P. Lacombe. Mise en évidence par le gallium radioactif (⁷²Ga) des premiers stades de la pénétration intergranulaire de l'aluminium par le gallium. *Mém. Sci. Mét.*, 67:367–375, 1970.
- [RAL73] C. Roques-Carmes, M. Aucouturier, and P. Lacombe. The influence of testing temperature and thermal history on the intergranular embrittlement and penetration of Aluminum by liquid Gallium. *Met. Sci. J.*, 7:128–132, 1973.
- [Ran93] V. Randle. *The measurement of grain boundary geometry*. Institute of Physics Pub., 1993.
- [Rao93] D. Raoux. *Neutron and Synchrotron Radiation for condensed matter studies*, volume 1, pages 37–63. Springer, 1993.
- [RKS00] E. Rabkin, L. Klinger, and V. Semenov. Grain boundary grooving at the singular surfaces. *Acta. mater.*, 48:1533–1540, 2000.
- [Roq71] C. Roques-Carmes. *Mise en évidence du rôle de l'adsorption dans les mécanismes de pénétration intergranulaire des métaux par les métaux liquides - cas des systèmes Acier - Lithium et Aluminium - Gallium*. PhD thesis, Université de Paris-Sud, Orsay, 1971.
- [RSS91] E. Rabkin, L. S. Shvindlerman, and B. Straumal. Grain boundaries: Phase transitions and critical phenomena. *Int. J. Mod. Phys. B*, 5:2989–3028, 1991.
- [RSSS91] E. Rabkin, V. Semenov, L. S. Shvindlerman, and B. Straumal. Penetration of tin and zinc along tilt grain boundaries 43° [100] in Fe-5 at.% Si alloy: Premelting phase transition? *Acta Metall. Mater.*, 39:627–639, 1991.
- [Sav00] S. Savelli. *Identification des mécanismes et approche quantitative de la fatigue d'alliages modèles d'aluminium de moulage*. PhD thesis, INSA Lyon, France, 2000.
- [Sch97] R. Schwarzer. Advances in crystal orientation mapping with the SEM and TEM. *Ultramicroscopy*, 67:19–24, 1997.
- [SD98] A. Sasov and D. Van Dyck. *European Microscopy and Analysis*, 3:21–23, 1998.

- [SF96] R. Stumpf and P. J. Feibelman. Towards an understanding of liquid-metal embrittlement: Energetics of Ga on Al surfaces. *Phys. Rev. B*, 54:5145–5150, 1996.
- [SGM94] B. Straumal, W. Gust, and D. Molodov. Tie lines of the Grain Boundary Wetting Phase Transition in the Al-Sn System. *J. Phase Equil.*, 15:386–391, 1994.
- [SKSL96] A. Snigirev, V. Kohn, I. Snigireva, and B. Lengeler. A compound refractive lens for focusing high-energy x-rays. *Nature*, 384:49–51, 1996.
- [SMGP91] R. Schmelzle, T. Muschik, W. Gust, and B. Predel. The inclination dependence of the energy of Cu Σ 3 and Σ 19a grain boundaries. *Scripta Mater.*, 25:1981–1986, 1991.
- [SMGP92] B. Straumal, T. Muschik, W. Gust, and B. Predel. The wetting transition in high and low energy grain boundaries in the Cu(In) system. *Acta Metall. Mater.*, 40:939–945, 1992.
- [SNS⁺92] B. Straumal, O. I. Noskovich, V. N. Semenov, L. S. Shvindlerman, W. Gust, and B. Predel. Premelting transition on $38^\circ < 100 >$ tilt grain boundaries in (Fe-10at.%Si)-Zn alloys. *Acta Metall. Mater.*, 40:795–801, 1992.
- [SSK⁺95] A. Snigirev, I. Snigireva, V. Kohn, S. Kuznetsov, and I. Schelokov. On the possibilities of X-ray phase contrast microimaging by coherent high-energy synchrotron radiation. *Rev. Sci. Instrum.*, 66:5486–5492, 1995.
- [SSR⁺96] B. Straumal, V. Sursaeva, S. Risser, B. Chenal, and W. Gust. *Mater. Sci. Forum*, 207-209:557, 1996.
- [Sur94] S. Suresh. *Fatigue of materials*. Cambridge University Press, Cambridge, 1st edition, 1994.
- [Tal36] H. F. Talbot. *Phil. Mag.*, 3rd series 9:401, 1836.
- [Tan76] B. K. Tanner. *X-ray Diffraction Topography*. Pergamon Press, Oxford, 1976.
- [THP⁺00] D. I. Thomson, V. Heine, M. C. Payne, N. Marzari, and M. W. Finnis. Insight into gallium behavior in aluminum grain boundaries from calculations on $\Sigma=11$ (113) boundary. *Acta mater.*, 48:3623–3632, 2000.
- [ZMH⁺99] E. Ziegler, C. Morawe, O. Hignette, P. Cloetens, and R. Tucoulou. Multilayer X-ray optics for high energy third generation synchrotron sources: the state of the art. In Y. Furukawa, Y. Mori, and T. Kataoka, editors, *Precision Science and Technology for Perfect Surfaces, Proceedings of the 9th International Conference on Production Engineering, Osaka, Japan*, 3, pages 285–291, 1999.
- [ZWM00a] T. Zhai, A. J. Wilkinson, and J. W. Martin. A crystallographic mechanism for fatigue crack propagation through grain boundaries. *Acta Mat.*, 20:4917–4927, 2000.
- [ZWM00b] T. Zhai, A. J. Wilkinson, and J. W. Martin. The effect of micro texture and β' particle distribution on short fatigue crack growth in an Al-Li 8090 alloy. *Materials Science Forum*, 331:1549, 2000.
- [ZZ95] G. Zanella and R. Zannoni. The detective quantum efficiency of an imaging detector. *Nucl. Instr. Meth. A*, 359:474–477, 1995.

Appendix A

The new tomograph

The increasing demand for microtomographic characterization of materials in applied scientific and industrial research led to a major upgrade and extension of the ID19 multipurpose experimental station in spring/summer 2000. The new, enlarged experiments hutch can permanently accommodate the different experimental set-ups (microtomography, high-resolution diffraction & topography, curvable monochromator) and will help to avoid time consuming realignment procedures.

The working experience with the initial set-up and its encountered shortcomings gave rise to the design of an optimized instrument, dedicated for routine use in high-resolution tomography. The design goal was to ensure maximum flexibility and the preservation of the ultimate spatial resolution of 1 μm for tomographic imaging. For this, the mechanical design and the choice of components have to meet stringent requirements concerning stability and precision. Compared to the former set-up which consisted of two distinct blocs, the new instrument was designed as monobloc. This solution should eliminate instabilities arising from different thermal expansion and vibrations of the formerly separated instruments. Moreover, both functional units, the sample and the camera bloc were subject to modifications in order to yield maximum possible precision and versatility of the new instrument.

The foreseen instrument (currently under construction) is depicted in Figure A.1 and will be briefly described in the following paragraphs.

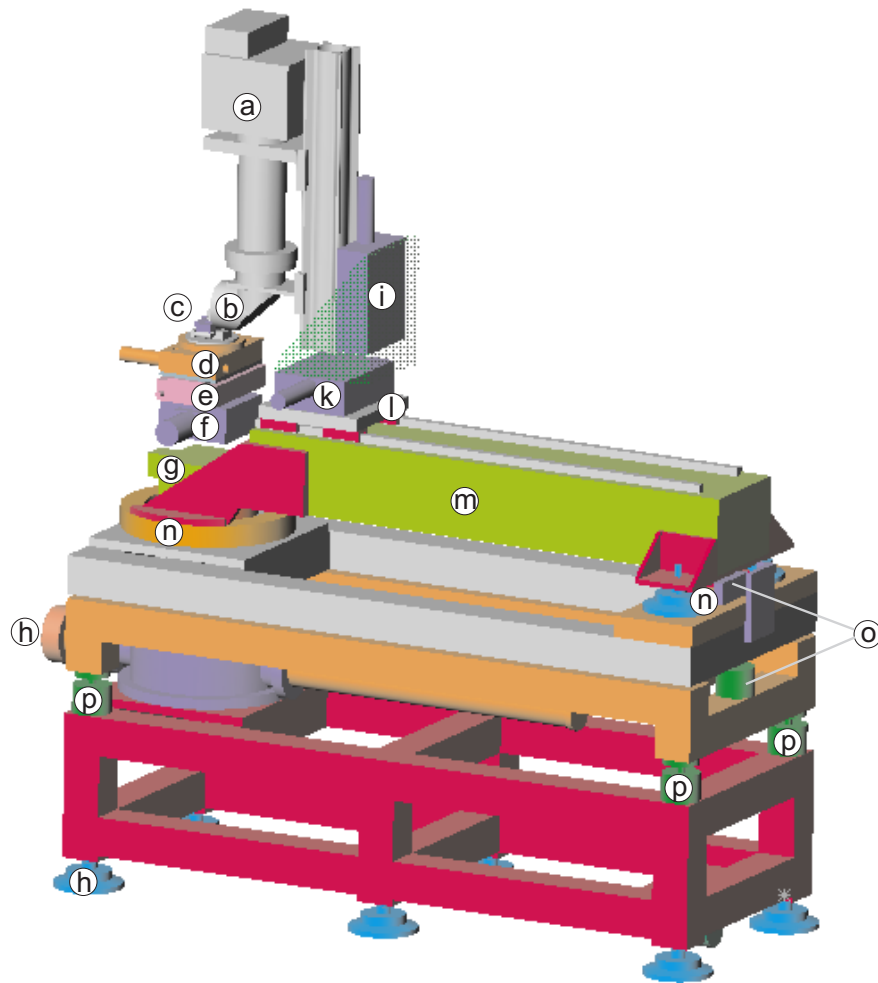
The base frame

The base frame hosts two functional modules enabling the movement and positioning of the instrument as a whole and a precise vertical movement for the upper frame. Although permanent installation of the instrument is foreseen in the future, a system of airpads and a rotation module allow to move and to perform a prealignment of the instrument on the polished marble floor.

The vertical translation (p) is required to follow the position of the beam which depends on the choice of monochromator and energy. The instrument can operate at up to 4 m distance with respect to the vertically diffracting multilayer. Special attention was given to the rigidity of the vertical movement: four guide tubes provide the necessary precision of this movement.

The sample stage

The sample stage consists of a series of precise movements used for alignment and for accurate positioning of the sample during the tomographic scan:



- a ESRF Frelon camera
- b camera objective (motorized focus)
- c X1,X2: sample micro-translations (Micos MP55)
- d PMO: sample rotation (Newport M-PM500 360)
- e PMY: sample translation y (Newport M-Pm500 6L)
- f Z2: sample z translation (Huber 5103.2)
- g sample tilt 1
- h mounting used for coarse alignment of the instrument (incl. airpads)
- i Zc: camera z translation
- k Yc: camera y translation
- l Xc: camera x translation (1m)
- m marble beam
- n rotation of marble (incl. airpads)
- o tilt 2 (sample and camera)
- p Z3: translation of upper frame

Figure A.1: Design of the new tomographic instrument (currently under construction). All movements are motorized and will allow for automatic alignment with the precision required for high-resolution tomographic imaging.

Sample tilt (g) is used for the alignment of the rotation axis with respect to the camera. An angular resolution of 10^{-4} rad is necessary to enable perfect alignment with respect to the columns of the CCD camera (1/10 of a pixel over the entire field of view, 1024 pixels). Misalignment of the axis will lead to unrecoverable degradation of the spatial resolution in the reconstructed images.

The vertical translation (f) is used for vertical positioning of the sample. Unwanted angular movements during translation must be smaller than 10^{-4} rad in order to preserve the alignment and the position of the rotation axis relative to the columns of the CCD. This limits the maximum stroke to 50 mm.

The ultra-precision translation and rotation unit(e,d) may be considered as the heart of the instrument. During a tomographic scan only these two movements are involved and they have direct influence on the ultimate resolution which can be achieved in the three-dimensional reconstruction. The translation is used to remove the sample during a scan in order to take regular updates of the background images. The sample has to be repositioned with an accuracy better than the resolution of the detector. The DC-motor driven translation stage PM500-LM (Newport) offers closed-loop positioning with an optical encoder and achieves a resolution and repeatability of $0.1 \mu\text{m}$.

The rotation stage PM500-360R (Newport) was chosen because of the small concentricity and wobble errors of the rotation axis. Characterization in the metrology laboratory gave a total wobble range of $9.1 \mu\text{rad}$ and a concentricity range of $1.6 \mu\text{m}$. The total (horizontal) translation error at the level of the sample ($\Delta z = 80 \text{ mm}$) over a half turn is in the order of $1 \mu\text{m}$ and is still acceptable for the current spatial resolution. Typical angular sampling rates required for tomographic imaging are in the order of $\pi/N_{\text{pix}} \approx 0.1$ degree and the nominal accuracy of $5 \cdot 10^{-3}$ degrees is therefore largely sufficient. Compared to conventional stepper-motor rotation stages, the PM500 series has the additional advantage to combine high precision with high velocities (up to $200^\circ/\text{s}$ for the rotation stage). This is very convenient during alignment when rotations over 180° have to be performed repeatedly.

Two crossed micro-translations(c) are mounted above the rotation stage and allow to center the sample with respect to the rotation axis. Precise centering of the sample allows to take advantage of the entire field of view during a tomographic scan.

A Goniometer head serves currently as sample holder. Two manual tilts allow to align the sample axis with respect to the rotation axis. A motorization of the tilts would be desirable but turns out problematic due to the limited available space.

The second tilt (o) is common to the sample and detector bloc and serves for alignment of the upper frame with respect to the direction of the beam. The rotation axis has to be aligned perpendicular to the beam direction (10^{-4} rad). This, together with the alignment by tilt (c) ensures that the tomographic slices (perpendicular to the rotation axis) are independent and enables us to use fast slice by slice reconstruction algorithms.

The inclination of the upper frame as a whole facilitates the use of the multilayer monochromator: sample and camera move as a rigid bloc and relative alignment between both is preserved. The acquisition of a defocus series (i.e. images in different distances from the sample) requires now only one single movement (i). Due to the large distance the required resolution of 10^{-4} rad is achieved via a linear movement of moderate accuracy ($100 \mu\text{m}$).

The translation unit consists of a polished marble beam (m) with a precision linear movement (l) of 1 m length mounted on it. Alignment of the translation unit parallel to the beam is accomplished by the previous tilt (o) and a system of airpads and a motorised translation (n). A precision of $1 \mu\text{m}$ is required for this movement in order to eliminate displacements of the image when the sample to detector distance is changed. Moreover, the wobble of the linear movement (l) must be smaller than 10^{-4}rad in order to preserve the alignment of the rotation axis during displacements of the camera.

The camera unit provides the missing vertical (i) and horizontal (k) movements required for precise positioning of the camera with respect to the center of the beam. The horizontal movement has enough stroke to remove the camera completely out of the beam path. It is therefore possible to use the beam in the back of the experimental hutch without removing the tomographic stage. The alignment of the set-up is preserved and deadtimes due to realignment procedures will be minimised in the future. The vertical movement provides additional stroke for the translation (f). This might be necessary for accommodation of sample environments like tension rigs, furnaces etc. of different size.

Appendix B

Approximation for an absorbing object

Our phase reconstruction in the case of an absorbing object was based on expression 3.1, derived for the case of a pure phase object. We used the same approach, replacing the intensity distribution I_D with the quotient I_D/I_0 :

$$\mathcal{F}\left\{\frac{I_D(\mathbf{x})}{I_0(\mathbf{x})}\right\} = \delta(\mathbf{f}) + 2 \sin(\pi \lambda D \mathbf{f}^2) \tilde{\varphi}(\mathbf{f}). \quad (\text{B.1})$$

It can be shown that this operation formally corresponds to the introduction of two additional approximations into the general expression (equ. 1.27) for the intensity spectrum of an absorbing object. Writing the object as $T = A(\mathbf{x}) \exp\{i\varphi(\mathbf{x})\}$ and developing the phase term we may express the intensity spectrum as

$$\begin{aligned} \tilde{I}_D(\mathbf{f}) &= \int e^{-i2\pi\mathbf{x}\mathbf{f}} \underbrace{A\left(\mathbf{x} + \frac{\lambda D \mathbf{f}}{2}\right) A\left(\mathbf{x} - \frac{\lambda D \mathbf{f}}{2}\right)}_{\cong A^2(\mathbf{x}) = I_0(\mathbf{x})} \left\{1 + i\varphi\left(\mathbf{x} + \frac{\lambda D \mathbf{f}}{2}\right) - i\varphi\left(\mathbf{x} - \frac{\lambda D \mathbf{f}}{2}\right)\right\} d\mathbf{x} \quad (\text{B.2}) \\ &\cong A^2(\mathbf{x}) = I_0(\mathbf{x}) \end{aligned}$$

It will be necessary to introduce the approximation $A\left(\mathbf{x} + \frac{\lambda D \mathbf{f}}{2}\right) A\left(\mathbf{x} - \frac{\lambda D \mathbf{f}}{2}\right) \approx A^2(\mathbf{x})$. Under the condition of a smoothly varying absorption profile and weak defocus distances, the introduction of this approximation seems justified. We may now write the integral in the form

$$\begin{aligned} \tilde{I}_D(\mathbf{f}) &\approx \tilde{I}_0(\mathbf{f}) + i \int I_0(\mathbf{x}) e^{-i2\pi\mathbf{x}\mathbf{f}} \left\{ \int e^{i2\pi\mathbf{h}\left(\mathbf{x} + \frac{\lambda D \mathbf{f}}{2}\right)} \tilde{\varphi}(\mathbf{h}) - e^{i2\pi\mathbf{h}\left(\mathbf{x} - \frac{\lambda D \mathbf{f}}{2}\right)} \tilde{\varphi}(\mathbf{h}) d\mathbf{h} \right\} d\mathbf{x} \\ &\approx \tilde{I}_0(\mathbf{f}) + 2 \int I_0(\mathbf{x}) \int e^{-i2\pi(\mathbf{f}-\mathbf{h})\mathbf{x}} \tilde{\varphi}(\mathbf{h}) \sin(\pi \lambda D \mathbf{h} \mathbf{f}) d\mathbf{h} d\mathbf{x} \quad (\text{B.3}) \end{aligned}$$

where we have expressed $\varphi(\mathbf{x})$ in terms of its Fourier transform. Changing the order of integration yields

$$\begin{aligned} \tilde{I}_D(\mathbf{f}) &\approx \tilde{I}_0(\mathbf{f}) + 2 \int \tilde{\varphi}(\mathbf{h}) \underbrace{\sin(\pi \lambda D \mathbf{h} \mathbf{f})}_{\approx \sin(\pi \lambda D \mathbf{h}^2)} \tilde{I}_0(\mathbf{f} - \mathbf{h}) d\mathbf{h} \quad (\text{B.4}) \\ &\approx \sin(\pi \lambda D \mathbf{h}^2) \end{aligned}$$

In order to reduce this expression to equation (B.1), we have to introduce a second approximation, consisting in the change of the argument of the sine function $\pi \lambda D \mathbf{h} \mathbf{f} \leftrightarrow \pi \lambda D \mathbf{h}^2$.

The justification of this second approximation is not obvious in the current formulation of the problem.

After this second modification, the integral reduces to the convolution

$$\tilde{I}_D(\mathbf{f}) \approx \tilde{I}_0(\mathbf{f}) + \tilde{I}_0(\mathbf{f}) \otimes \{\tilde{\varphi}(\mathbf{f}) 2 \sin(\pi\lambda D \mathbf{f}^2)\} \quad (\text{B.5})$$

or

$$\tilde{I}_D(\mathbf{f}) \approx \tilde{I}_0(\mathbf{f}) \otimes \{\delta(\mathbf{f}) + \tilde{\varphi}(\mathbf{f}) 2 \sin(\pi\lambda D \mathbf{f}^2)\}. \quad (\text{B.6})$$

The equivalence of (B.6) and (B.1) is obvious if we go back temporarily to real space:

$$I_D(\mathbf{x}) \approx I_0(\mathbf{x}) \cdot \left\{ 1 + \mathcal{F}^{-1} \{ \tilde{\varphi}(\mathbf{f}) 2 \sin(\pi\lambda D \mathbf{f}^2) \} \right\} \quad (\text{B.7})$$

hence

$$\frac{I_D(\mathbf{x})}{I_0(\mathbf{x})} \approx 1 + \mathcal{F}^{-1} \{ \tilde{\varphi}(\mathbf{f}) 2 \sin(\pi\lambda D \mathbf{f}^2) \} \quad (\text{B.8})$$

and finally

$$\mathcal{F} \left\{ \frac{I_D(\mathbf{x})}{I_0(\mathbf{x})} \right\} \approx \delta(\mathbf{f}) + \tilde{\varphi}(\mathbf{f}) 2 \sin(\pi\lambda D \mathbf{f}^2). \quad (\text{B.9})$$

Appendix C

Basic concepts of GBW models

C.1 The role of coherency strain

Rabkin has tried to explain the formation of relatively thick macroscopic liquid grooves in terms of a model which invokes diffusion of the liquid metal into the undersaturated solid ahead of the groove tip [Rab98]. Due to the dependence of the lattice parameter a on the concentration of solute, the diffusion zone is strained and has a higher chemical potential compared to the regions behind the groove tip, where the coherency is already lost due to emission of misfit dislocations. The coherently strained layer at the groove tip is in contact with a locally undersaturated liquid and dissolves into the liquid. As soon as the concentration of solute reaches some critical concentration, the elastic strain is released by nucleation of misfit dislocations and the preferential dissolution stops. Rabkin arrives at an expression which relates the thickness of the grooves to elastic properties and diffusion coefficients of the solid metal:

$$h = \frac{E\alpha^2 b V_m}{2(1+\nu)^2(1-\nu)RT} \left(\frac{D_{eff}}{D_v} \right) \quad (\text{C.1})$$

where E is Young's module, b the typical Burgers vector of the misfit dislocations, V_m the molar volume and ν the Poisson ratio of the solid metal. The parameter $\alpha \approx 2$ depends only very weakly (logarithmically) on the solute concentration c_0 and the misfit parameter η . D_{eff} describes the dissolution rate of the solid/liquid interface and D_v is the volume diffusion coefficient. RT has its usual meaning as the product of the universal gas constant and the absolute Temperature.

The model predicts very weak dependence of the groove width on the concentration of solute in the solid material. However, in the case of a completely saturated solid (i.e. of solidus composition according to the equilibrium phase diagram) no diffusion will occur and macroscopic grooving should be absent. Rabkin calculates a lower limit for the groove width by assuming that diffusion across the solid-liquid interface is comparable to bulk diffusion. He obtains a characteristic width in the order of $0.1 \mu\text{m}$ for common metal systems.

As stated by this author, his model is rather suitable for refractory metals and ceramics, which are intrinsically brittle. It seems not appropriate for ductile fcc metals and alloys, where the coherency in the bulk diffusion zone is probably lost in the early stages of the diffusion process, since many mobile dislocations are available to relax the strain.

C.2 The dissolution models

C.2.1 The model of Fradkov

The mathematical analysis carried out by Fradkov [Fra94] suggests the existence of two kinetic regimes for liquid grooving which depend on the state of saturation of the liquid phase. According to this author, the evolution of the groove shape can be described by an equation of the form:

$$V_n = \gamma\Omega\kappa K + V_0 \quad (\text{C.2})$$

V_n : dissolution rate normal to the surface

K : curvature of the interface

γ : solid liquid interface energy

Ω : atomic volume of the solid metal

κ : kinetic constant of dissolution

V_0 : dissolution rate of flat surface

Capillary mode ($V_0 = 0$). If the liquid is saturated by the solid, the V_0 term will vanish and the groove growth will be governed by capillary forces only. Fradkov has extended the classical analysis of Mullins to the case of small dihedral angles and deduces a groove profile which decreases exponentially with depth and grows slowly as the square root of time.

Etching mode ($V_0 > 0$). In the case of undersaturation the additional dissolution rate V_0 leads to linear grooving kinetics with (see Fig. C.1)

$$V = \frac{V_0}{\sin \varphi_0} \quad (\text{C.3})$$

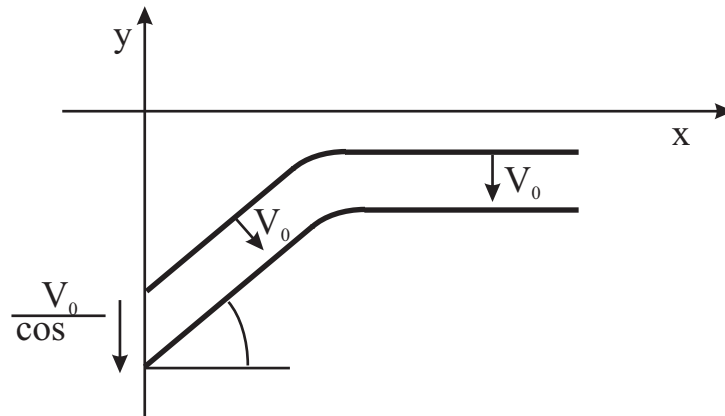


Figure C.1: Growth of a liquid metal etching groove by a dissolution mechanism ([Fra94])

According to this author, the singularity of the kinetics in the case of perfect wetting ($\varphi=90^\circ$) is avoided because other factors like the diffusional removal of solid material through the elongated channels will govern the grooving process in this situation.

The relevance of this model is unclear due to the fact, that rapid penetration has also been observed in the case of pre-saturated liquid phases, whereas the model predicts absence of rapid grooving in this case (capillary mode).

C.2.2 The model of Bokstein

Bokstein distinguishes a capillary mode for saturated liquid solutions and different etching modes in the case of undersaturated solutions. According to this author one has to distinguish three different kinetic regimes in the case of undersaturation.

Dissolution regime. In this case the grooving speed is controlled by the dissolution process across the interface only. Both, the diffusion of solute solid atoms in direction parallel and perpendicular to the groove (towards the reservoir of constant concentration outside the groove) are considered as very rapid compared to the dissolution process. In this case the width (w) and depth (h) of the groove vary linearly with time (cf. etching mode of Fradkov).

Diffusion regime. The grooving process is controlled by the slow diffusional migration of the solute in both directions, perpendicular and parallel to the groove walls. The groove profile varies in both directions with $t^{1/2}$.

Mixed regime. This case applies for long, narrow channels where the diffusion across the channel width is assumed sufficiently rapid to establish constant concentration, whereas the mass transport along the groove direction is controlled by the concentration gradient from the groove tip to the external reservoir. The width w of such grooves varies linearly with time, whereas the depth varies only with $t^{1/2}$. The shape depends further on the level of saturation of the liquid and tends towards narrower profiles for higher concentrations of the solid metal.

C.3 A thermodynamic approach

Desré proposed a mechanism for the penetration of a liquid metal along grain boundaries, which invokes the formation and thickening of a metastable "quasi-liquid" layer at the grain boundaries [Des97]. This metastable layer transforms into a liquid phase as soon as it reaches a critical thickness. Desré applied his model to the system Al/Ga and calculates a critical thickness of the layer smaller than a monolayer. He attributes this rather unrealistic result to the inaccuracy of the available thermodynamic data for the system Al/Ga.

Recently, Joseph and coworkers adopted this approach to the system Cu/Bi and interpret their experimental observations in the framework of this thermodynamic model [JBA99]. Whereas the model allows some insight into the thermodynamic stability of a thin amorphous phase at a grain boundary, it does not address the question of groove morphology and the analysis of the kinetic mechanism remains unclear. In fact the authors do not specify the transport mechanism with which the 'embrittler' atoms arrive at the groove tip.

C.4 The SIIS model

Glickman has recently proposed a model which allows to explain a large number of experimental observations in a consistent way [GN99]. This model applies to grooving by saturated liquids

and invokes a stress driven diffusion flux I_{gb} of the solid material along the grain boundary *ahead* of the moving groove tip. The stress results from an imbalance of surface tensions at the groove tip ("self-indentation") where a 'dynamic' angle θ_d is established (see Fig. C.2). There is experimental evidence, that the 'dynamic' angle is rather close to $\pi/2$ than to its theoretical value ($\theta_0 = 0$ for $S=0$). The grain boundary is assumed to act as perfect sink for the atoms removed from the groove cavity ("internal solution"). The stress driven flux of solid atoms ahead of the groove tip (I_{gb}) is coupled to the curvature driven diffusion flux I_K resulting from the convex-down shape of the groove profile and both together lead finally to the deepening of a groove with constant width h .

Glickman arrives at the following estimates for the grooving rate V and the width h of the grooves:

$$V \approx \frac{(D_{gb}\gamma_{gb}m)^2\Omega}{D_l\gamma_{sl}C_{l\infty}L^2kT}, \quad (C.4)$$

$$h \approx \frac{D_l\gamma_{sl}C_{l\infty}L}{D_{gb}\gamma_{gb}m}, \quad (C.5)$$

where

$$m = 1 - \frac{\cos \theta_d/2}{\cos \theta_0/2} \quad (C.6)$$

- D_l diffusion coefficient in liquid
- D_{gb} grain boundary diffusion coefficient
- Ω atomic volume of solid
- L characteristic distance between dislocation like defects
- $C_{L\infty}$ equilibrium solubility of SM in LM

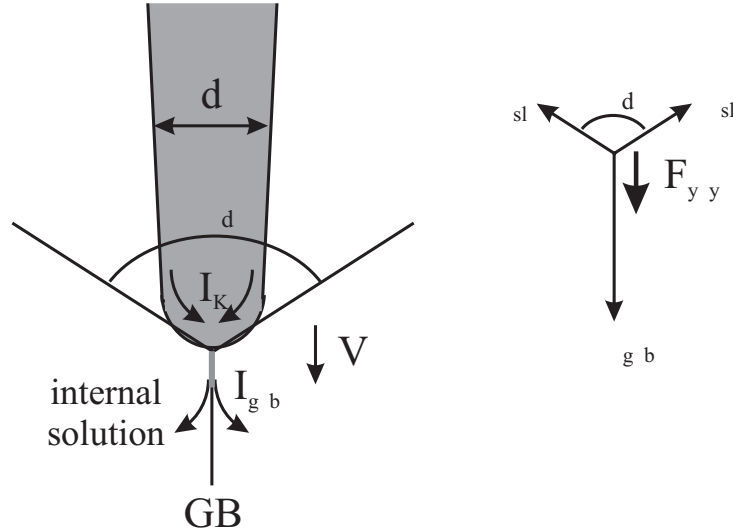


Figure C.2: Illustration of the 'self indentation internal solution' model of Glickman. The 'dynamic' angle θ_d creates an imbalanced capillary force F_{yy} and leads to internal solution of the solid material ahead of the groove tip

Whereas the calculated values correspond well to experimental results obtained at high temperatures ($T \geq 0.6T_m$), there is a big discrepancy concerning the results of liquid grooving

experiments at low temperatures ($T < 0.43 T_m$, e.g. Al-Ga, Zn-Ga), where grain boundary diffusion would be far too slow to accommodate the invoked material fluxes. Glickman attributes this to the fact that in the experimental studies he refers to, the liquid metal was not presaturated and that dissolution mechanisms (see the above models of Fradkov and Bokstein) are operational in these experiments.

Curriculum Vitae

Personal details

Surname Ludwig
Forename Wolfgang

Date of birth 23.08.1968
Place of birth Ingolstadt (Germany)
Marital status married, one child

Education

1988 Abitur (Apian Gymnasium Ingolstadt)

1989 Military Service (Sports company Sonthofen)

University

1989 Physics at the Technical University of Munich (TUM)
(Studienrichtung technische Physik)

1991 Vordiplom

1996 Diploma thesis at the Munich research reactor (FRM I):
*'Development of a position sensitive neutron detector and
application to neutron computer tomography'*

1996 Diploma in physics ('sehr gut bestanden')

PhD thesis

1997 Start of PhD thesis at the European Synchrotron Radiation Facility, France:
'Development and Applications of Synchrotron Radiation Microtomography'

2001 thesis submitted

Courses

1998 HERCULES *Higher European Research Course for Users
of Large Experimental Systems*, Grenoble, France, (6 weeks)

1997 Autumn school on X-ray diffraction, Smolenice (1 week)

1999 Electron microscopy, INPG, Grenoble, (1 week)

Teaching

1999 Courses in the computing language C at the ENSPG, INPG, Grenoble